AD-A183 882 INVESTIGATION OF RAPIDLY-SOLIDIFIED DISPERSION STRENGTHENED TITANIUM ALLOYS(U) UNITED TECHNOLOGIES RESEARCH CENTER EAST HARTFORD CT D B SNOW 01 JUL 87 UTRC/R87-917553-2 1/2

UNCLASSIFIED F/G 11/6.1 NL

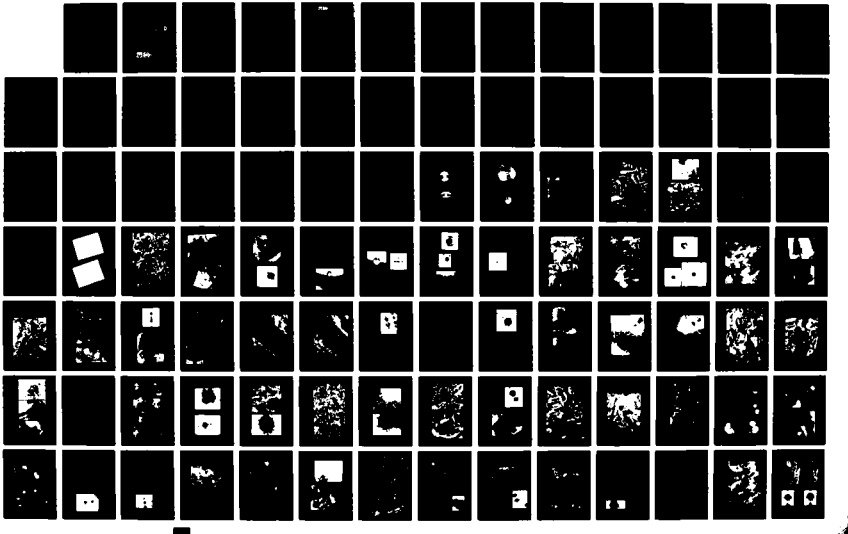

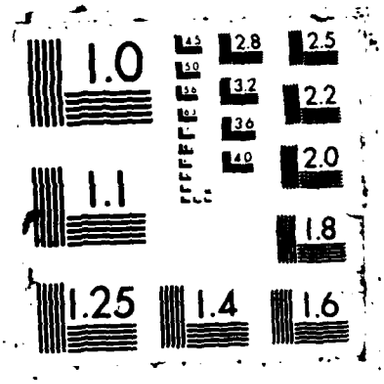
1.0
1.1
1.25
1.4
1.6
2.8
3.2
3.6
4.0
2.5
2.2
2.0
1.8

R87-917553-2

(12)

DTIC FILE COPY

AD-A183 882

Investigation of Rapidly-Solidified Dispersion Strengthened Titanium Alloys

Prepared by
D.B. Snow

Annual Report

Contract N00014-85-C-0426

for
Office of Naval Research
Department of the Navy
Arlington, VA 22217-5000

UNITED TECHNOLOGIES RESEARCH CENTER
East Hartford, Connecticut 06108

UNCLASSIFIED
SECURITY CLASSIFICATION OF THIS PAGE

AD-A183 012

REPORT DOCUMENTATION PAGE

1a. REPORT SECURITY CLASSIFICATION Unclassified	1b. RESTRICTIVE MARKINGS
2a. SECURITY CLASSIFICATION AUTHORITY	3. DISTRIBUTION / AVAILABILITY OF REPORT
2b. DECLASSIFICATION / DOWNGRADING SCHEDULE	
4. PERFORMING ORGANIZATION REPORT NUMBER(S) R87-917553-2	5. MONITORING ORGANIZATION REPORT NUMBER(S)
6a. NAME OF PERFORMING ORGANIZATION United Technologies Research Center 6b. OFFICE SYMBOL (If applicable)	7a. NAME OF MONITORING ORGANIZATION
6c. ADDRESS (City, State, and ZIP Code) East Hartford, CT 06108	7b. ADDRESS (City, State, and ZIP Code)
8a. NAME OF FUNDING / SPONSORING ORGANIZATION Office of Naval Research 8b. OFFICE SYMBOL (If applicable)	9. PROCUREMENT INSTRUMENT IDENTIFICATION NUMBER
8c. ADDRESS (City, State, and ZIP Code) Arlington, VA 22217-5000	10. SOURCE OF FUNDING NUMBERS PROGRAM ELEMENT NO / PROJECT NO. / TASK NO. / WORK UNIT ACCESSION NO.

11. TITLE (Include Security Classification)
INVESTIGATION OF RAPIDLY-SOLIDIFIED DISPERSION STRENGTHENED TITANIUM ALLOYS

12. PERSONAL AUTHOR(S)
D. B. Snow

13a. TYPE OF REPORT	13b. TIME COVERED	14. DATE OF REPORT (Year, Month, Day)	15. PAGE COUNT
Annual Report	FROM 9/85 TO 8/86	1987 July 1	97

16. SUPPLEMENTARY NOTATION

17. COSATI CODES		
FIELD	GROUP	SUB-GROUP

18. SUBJECT TERMS (Continue on reverse if necessary and identify by block number)
Splat quenching, Titanium Martensite, Titanium-aluminum alloys, Yttrium oxide, Neodymium oxide, Rapid solidification

19. ABSTRACT (Continue on reverse if necessary and identify by block number)

Significant potential exists for the improvement of high temperature strength in titanium base alloys by the addition of rare earth elements, followed by rapid solidification and aging. To investigate this potential, the relative effectiveness with which several different rare earth elements form oxide dispersions in splat-quenched Ti-Al solid solutions was examined, using Ti-Al-Er as a basis of comparison. The alloying elements of this type which were utilized included yttrium, lanthanum, neodymium, gadolinium, terbium, dysprosium, erbium and lutetium, added individually in amounts of ~0.5 at% each. Procedures were developed to prepare rapidly solidified laboratory quantities of these alloys by arc melting and splat quenching in the same apparatus, followed by aging in high purity argon. The dispersions formed in these alloys both before and after aging at 800°C were examined and compared by analytical transmission electron microscopy. While it was not generally possible to completely suppress the precipitation of intercellular oxides by splat quenching to thicknesses of ≥60 μm, in all cases most of the yttrium or the rare earth component of the alloy was retained in supersaturated solid solution. In alloys

20. DISTRIBUTION / AVAILABILITY OF ABSTRACT ☐ UNCLASSIFIED/UNLIMITED ☒ SAME AS RPT. ☐ DTIC USERS	21. ABSTRACT SECURITY CLASSIFICATION Unclassified
22a. NAME OF RESPONSIBLE INDIVIDUAL Dr. R. C. Pohanka	22b. TELEPHONE (Include Area Code) (202) 696-4401 22c. OFFICE SYMBOL

DD FORM 1473, 84 MAR 83 APR edition may be used until exhausted. All other editions are obsolete.

SECURITY CLASSIFICATION OF THIS PAGE
UNCLASSIFIED

Block #18 (Cont'd)

Rapid solidification technology
Oxide dispersion strengthening
Rare earth oxides
Lanthanum oxide
Gadolinium oxide
Dysprosium oxide
Terbium oxide
Rare earth element alloying
Erbium oxide
Lutetium oxide

Block #19 (Cont'd)

with Y, Gd, Dy, or Er additions, the structure of the $\geq$50 nm intercellular and intergranular precipitates which formed during rapid solidification and solid state cooling was that of the sesquioxide of each of these elements. Both cubic and monoclinic rare earth sesquioxides were observed at intercellular sites in as-splat-quenched Ti-Al-Gd and Ti-Er-Dy. Aging at 800°C produced a more homogeneous, intragranular dispersion of $<$50 nm precipitates in all eight alloys. The most common precipitate-matrix orientation relationship observed after aging was one in which {111} of the oxide was parallel to, and coherent with, (0001) of the HCP titanium-aluminum solid solution. This group of (Type I) precipitates were cubic, with a lattice parameter less than that of the corresponding equilibrium-structure sesquioxide, orientated with (111) of the precipitate parallel to (0001) of the matrix, and $[11\bar{2}]$ precipitate parallel to $[1\bar{1}00]$ of the matrix. They exhibited strong strain contrast when viewed with g = 0002. These Type I yttrium and rare earth oxides were faceted on (111), and were rectangular in profile when viewed in the $[11\bar{2}]$ direction, with a maximum dimension of ~35 nm after aging at 800°C for $\leq$4 hr. A much smaller quantity of cubic "Type II" precipitates were also detected in the same aged specimens. These had a lattice parameter equal to that of the equilibrium-structure cubic sesquioxide of the rare earth element in each alloy. They also induced strain contrast indicative of semi-coherency, but were distinct from the Type I precipitates in that the strain contrast was associated with g = 1120. The Type II oxides exhibited a crystallographic orientation of $(1\bar{1}0)$ precipitate || (0001) matrix and $[11\bar{2}]$ precipitate || $[1\bar{1}00]$ matrix. The largest quantities of finely-dispersed oxides which were precipitated by aging were observed in the alloys which contained yttrium, terbium, dysprosium or erbium.

UNITED
TECHNOLOGIES
RESEARCH
CENTER
East Hartford, Connecticut 06108

R87-917553-2

Investigation of Rapidly-Solidified Dispersion Strengthened Titanium Alloys

ANNUAL REPORT

Contract N00014-85-C-0426

REPORTED BY _____
D. B. Snow

APPROVED BY _____
A. V. Manzione

DATE July 1, 1987

TABLE OF CONTENTS

INTRODUCTION

The continuing effort to develop structural materials which have improved high temperature properties for aircraft gas turbine engine applications includes advanced alloys based on titanium. Currently, there is significant interest in the potential for increasing both the high temperature yield and creep strengths of titanium alloys by dispersion strengthening, achieved by rapid solidification processing and aging. Since the dispersed particles must precipitate readily and resist subsequent diffusional coarsening, they must also have a low solubility in the surrounding matrix. Oxides of the lanthanide group, and chemically similar metals, fit these criteria well, since they have large free energies of formation and are relatively insoluble in many alloys, including those of titanium. Such oxides have been successfully used for high temperature dispersion strengthening in alloys such as tungsten (1), nickel (2), and mechanically alloyed nickel base alloys (3,4). An important distinction in the case of titanium base alloys, however, is that the oxide dispersion is created by precipitation from supersaturated solid solution.

Early attempts to increase the high temperature strength of titanium and its alloys with oxide dispersions achieved limited success. One of the first of these, an internally oxidized titanium-cerium alloy, was reported to display an improvement in stress rupture life up to 650 °C (5). Another study reported that the addition of cerium zirconate and thoria to titanium, followed by arc melting, caused oxide particles to precipitate during solidification, which in turn increased the tensile strength at 538 °C (6). A subsequent investigation considered the potential of specific rare earth oxides for dispersion strengthening titanium, and concluded that Lu_2O_3, Nd_2O_3 and Dy_2O_3 should be particularly effective, since they did not appear to be reduced by titanium at 1066 °C (7).

Efficient utilization of rare earth oxides for strengthening titanium alloys at elevated temperatures requires the creation of fine, homogeneous dispersions (8). As mentioned above, mechanical alloying has been successfully used to produce oxide dispersion strengthened (ODS) nickel base superalloys (3,4). Similar attempts to create Y_2O_3 dispersions in titanium base alloys did not significantly improve their mechanical properties (9,10). This illustrates that, in the case of conventionally cast alloys, the beneficial effects which might be expected to derive from the relative insolubility of most rare earth elements in titanium (11), together with their strong affinity for oxygen (12) (Figure 1), have frequently been negated by inherently slow solidification rates. During relatively slow cooling at or below the solidus temperature, the rare earth oxides precipitate as embrittling interdendritic segregates (13) and/or relatively coarse (~260 nm) dispersions (6,12). It is noteworthy , however, that at low concentrations, their deoxidizing effect can result in ductility improvement (13,14). Even after mechanical processing, the presence of 20-70 nm yttrium- or erbium- containing particles in conventionally cast Ti-6Al-4V was less

effective than expected in increasing strength at temperatures above 330 °C (15). To avoid some of these difficulties, the consolidation of P/M alloys from blended rare earth oxide and titanium powders has been suggested (16,17), but it is not clear that a sufficiently refined or homogeneous dispersion of fine particles can be achieved by this procedure. It has, however, been recognized for some time that conventional solidification processing was not well suited to exploit the affinity of the rare earth elements for oxygen in titanium-oxygen solutions, or the stability of the rare earth oxides thus formed (18). During the past several years the results of numerous investigations (8,19-29) have suggested that technologically significant dispersion strengthening can best be achieved in these alloys by one of several rapid solidification techniques.

Although early observations of rapidly solidified titanium-rare earth alloys revealed dispersed particles which were shown to contain a rare earth element (19), the identity of these phases remained uncertain. The precipitate morphology also remained poorly defined. Subsequent research programs utilized analytical transmission electron microscopy to positively determine that the dispersed compounds in rapidly solidified Ti-Er and Ti-Al-Y alloys were equilibrium structure erbium or yttrium sesquioxides (8,20-22). Er_2O_3 was also identified as the dispersed second phase in rapidly solidified Ti-6242-Er and Ti_3Al-Er (25-27). In addition, the precipitates in laser-processed Ti-6Al-4V-1.5Y, -3Nd and -1.5Er (wt%) were shown to have the equilibrium lattice structure of the corresponding rare earth sesquioxide (26). Other recent investigations of rapidly solidified titanium base alloys have identified dispersions of lanthanum-tin intermetallics (28), and of cerium sulfides and oxysulfides (29). Dispersed precipitates of this type located within grain interiors have resisted coarsening sufficiently to remain < 50 nm in size when aged below the beta transus of titanium base alloys (22,25,30). In addition to their stability, it has recently been demonstrated that rare earth compound dispersions are effective in increasing the creep strength of alpha titanium alloy matrices (29-33).

Particle dispersions can be formed in rapidly solidified Ti-Al-rare earth alloys by the reaction of the rare earth components with elements, often regarded as impurities, which are interstitially dissolved in the titanium solid solution. The results of most of the investigations cited previously indicate that if tin, carbon, nitrogen or sulfur are not major alloy constituents, and the quantities of interstitial impurities nominal for commercially-pure titanium are present, the dispersed rare earth compounds which precipitate during or after rapid solidification will (structurally) be oxides. Consequently, knowledge and control of the interstitial (particularly oxygen) content of the alloy throughout processing is an important research objective. This has been exemplified by recent reports that the coarsening rate of erbia in an HCP titanium matrix is strongly influenced by whether the total oxygen content of the alloy is greater or less than the amount required to convert all of the erbium in the alloy to stoichiometric erbium oxide (22,25). In the present investigation, the measurement and control of the interstitial content of the alloy specimens was an important objective.

The results presented in this report were obtained during the first year of this research program, which concerns the characterization of rare earth oxide dispersions created by the rapid solidification and aging of titanium-aluminum base alloys. Eight different alloys were arc melted, hammer & anvil splat quenched, and aged at 800 °C. Each had a nominal composition of Ti-11at% Al, to which 0.5 at% of yttrium or a lanthanide element had been added (Figure 2). Both the as-splat-quenched and aged microstructures of these alloys were examined and compared with respect to the identity, distribution and crystallography of the second phases which they contained.

EXPERIMENTAL PROCEDURE

In order to achieve the full potential of refractory rare earth oxide dispersion strengthening, it was necessary to be able to melt titanium alloys without undesired additions of oxygen from indigenous impurities, crucibles or protective atmospheres. A precision arc melter/splat quencher was constructed by modifying and improving a previously published design (34). This apparatus (Figure 3) offered the advantages of melting without ceramic contact; preparation of small (5-30 g) master melts in the form of buttons; the use of a gettered argon atmosphere to minimize contamination; and the capability of splat quenching 0.2-0.3 gram specimens to achieve large diameter, thin splats. As an additional precaution, sacrificial Ti was melted to create an oxygen sink prior to melting each alloy specimen. A typical button master melt is shown in Figure 4. The arc was sustained by three sharpened tungsten electrodes, which slanted toward the water-cooled copper hearth from the sides. The arcs from these electrodes were sustained until the hammer motion was initiated. Splats were prepared with various thicknesses by variation of the amount of alloy melted, the hammer pressure or by the use of spacers. Based on the work of Jones (35), it is estimated that a 100 um thick splat should correlate to a cooling rate of 10^5 to 10^6 degrees °C/s. Alloy design and characterization which utilizes this range of rapid solidification is also applicable to the powdermaking thermal environment. However, the use of splat quenched specimens provides the significant advantages of reduced time between the conception of a new alloy chemistry and the fabrication of a rapidly-solidified alloy. The appearance of a typical splat is exemplified by the titanium-aluminum-yttrium alloy shown in Figure 5.

Eight different alloys were arc melted, hammer & anvil splat quenched, and aged at 800 °C for 0.25 or 4 hours. The elements used for alloy consolidation were commercially-pure Ti rod (Grade 2), 99.999% Al shot, and 99.99% (metallics) sublimed rare earth elements. The titanium contained sufficient oxygen so that, in combination with the expected 200-300 ppm increase during melting and heat treatment, full sesquioxide stoichiometry could be achieved. The splat quenched specimens were wrapped in and supported by tantalum foil during heat treatment in a metal tube furnace filled with continuously gettered argon. The integrity of the various joints in the gas delivery and furnace systems was verified by an oxygen analyzer located at the exit orifice of the furnace. The nominal composition of all alloys was 11 at% Al and 0.5 at% yttrium or a lanthanide element.

The splat quenched specimens contained areas with smooth opposing surfaces, 60-175 um in thickness, from which thin foils were prepared for examination by transmission electron microscopy. Thin foil specimens were prepared by double jet electropolishing at $\leq$ -25 °C at an applied potential of 20 VDC in an electrolyte of 5 % perchloric acid in methanol. Microstructural characterization was carried out with a Philips EM400T analytical transmission electron microscope operated at 120 kV.

RESULTS

Post-Processing Alloy Composition.

The degree to which interstitial impurities were dissolved in the titanium base alloys which were acquired from the gas environment during arc melting was determined by examining buttons made from titanium of three different purities by gas fusion or combustion analysis (Table I). The carbon content of all samples was reported in each case to be either 100 or 200 wt ppm. It is apparent that these data reflect the lower limit of detection for combustion analysis, rather than the true amount of carbon present. The nitrogen content of most specimens was determined to increase by <30 ppm. The average increase in oxygen for all arc melted buttons was 250 $\pm$ 50 wt ppm. Although these are rather small quantities, considering the high solubility of interstitially dissolved elements in titanium, an effort is being made to reduce them.

All of the rare earth elements used for the alloys described herein were stored in argon-filled sealed containers. As oxygen is usually the principal impurity in rare earth elements, the oxygen content of the Dy was analysed after several months of storage in argon. Five-gram samples cut from the Dy stock were determined by neutron activation analysis to contain 0.43 $\pm$ 0.02 wt% oxygen (4.2 $\pm$ 0.16 at% O). Thus, the addition of ~0.5 at% rare earth containing approximately this quantity of oxygen should not have significantly increased the total oxygen content of any of the alloys (~200 at ppm O).

Previous documentation of the selective loss of aluminum from titanium alloys during electron beam melting (36) indicated that arc melting might have a similar effect on the alloys used in this investigation. The composition of a thin foil, electropolished from an arc-melted, splat quenched and aged specimen of Ti-11Al-0.5Gd (nominal at%), was determined by wavelength dispersive X-ray spectroscopy (EDS) with an electron microprobe. Quantitative analyses of spectra obtained from three 12 x 12 um areas (Figure 6) yielded values of 10.2 $\pm$ 0.3 at% Al and 0.42 $\pm$ 0.06 at% Gd, using previously analysed Ti-6Al-4V (wt%) and Gd_2O_3 specimens as standards. Thus, in this instance, approximately 7 % of the aluminum and 16 % of the gadolinium was lost during arc melting.

As-Splat-Quenched Microstructures

The as-splat-quenched grain structure of all eight alloys (splat thickness range: 60-175 um) consisted predominately of acicular, alpha-prime HCP martensite (Figure 7); with some individual grains of relatively equiaxed alpha phase (Figure 8). It has been suggested that a similar observation of non-acicular alpha in as-splat-quenched Ti-6Al-4V (wt%) was indicative of cooling rates of $>10^5$ °C/s (37). However, the quantity of non-acicular alpha observed in any specimen was always small, and did not appear to be correlated with splat thickness (cooling rate). An estimation of the prior-beta grain size (e. g., 5-7 um in ~150 um thick splats) could often be made by observing groups of martensite plates which had similar contrast (Figure 9).

The eight alloys which were examined during this investigation could be categorized into two groups, based on the precipitate distribution observed in as-splat-quenched specimens. The first group was comprised of the alloys in which yttrium, terbium, dysprosium or erbium was the precipitate-forming component. In as-splat-quenched specimens of these alloys, all precipitates were larger than 50 nm, and formed predominately intercellular patterns (Fig. 10). Less frequently, both intercellular and intergranular networks were observed (Figure 11). Dark field images formed from spots from individual precipitates showed that they had no common crystallographic orientation over distances of >100 nm, neither with respect to each other, nor to the Ti-Al matrix. There was no evidence that any homogeneous solid-state precipitation had occurred below the solidus temperature as the specimen cooled during the quenching process, even in splats as thick as 175 um (Figure 12). On the other hand, some intercellular and/or intergranular precipitation was always observed in all eight alloys at splat thicknesses of >60 um; consequently, complete supersaturation was never achieved.

The second group of alloys, which contained lanthanum, neodymium, gadolinium or lutetium as the precipitate-forming component, displayed an as-splat-quenched grain structure (Figures 13,14), and an intercellular and intergranular distribution of >50 nm precipitates which was quite similar to that observed in the group of alloys described above. However, as-splat-quenched specimens of these alloys also contained a second population of very small ($\leq$ 20 nm), intracellular precipitates (Figures 15,16), which appeared throughout the microstructure in both martensitic and non-martensitic alpha areas. Most of these were cubic "Type I", the form of rare earth oxide which was observed to precipitate in all eight alloys after aging at 800 °C. The microstructural characteristics of Type I precipitates will be described subsequently in more detail. However, their presence in the as-splat-quenched specimens of these four alloys suggests that lanthanum, neodymium, gadolinium and lutetium do not form metastable solid solutions with Ti-11 at% Al as easily as do yttrium, terbium, dysprosium or erbium.

Several of the larger intercellular precipitates in some of the as-splat-quenched alloys were individually characterized by energy-dispersive X-ray (EDX) analysis. This data revealed that they were, as expected, rare earth compounds (Figure 16), in agreement with the results of several previous investigations (20-22,26). The presence of a titanium peak in these spectra suggests that titanium may be a minor component in such precipitates. However, secondary fluorescence and/or beam spreading effects might account for some or all of the titanium signal from precipitates in thin foils (26,38). In the case of extraction replicas (26), the possibility that some matrix may have been extracted along with the precipitate cannot be excluded. Selected area and convergent beam diffraction patterns from >50 nm intercellular and intergranular precipitates in as-splat-quenched specimens which contained Gd, Dy or Er revealed that many had the cubic equilibrium structure of rare-earth sesquioxides (Table II, Figure 17). However, non-cubic intercellular sesquioxides were also observed in the Ti-Al-Gd and Ti-Al-Dy alloys (Figures 18,19). Analyses of selected area diffraction patterns (Tables II & III), calibrated by the diffraction spots from the Ti-11 at% Al matrix, showed that the structure of these precipitates was the equilibrium, monoclinic (B-type) high-temperature polymorphs of Gd_2O_3 and

Dy_2O_3 (39,40). A similar observation of a retained metastable rare earth oxide crystal structure (hexagonal, A-type) was made in the case of interdendritic Nd_2O_3 in as-laser-processed Ti-6Al-4V-3Nd (wt%) (26).

Microstructures of specimens aged at 800 °C

The general characteristics of the microstructure of each alloy followed the pattern observed in the as-splat-quenched specimens. That is, the alloys containing terbium, dysprosium or erbium which were aged at 800 °C all exhibited a predominately unrecrystallized, martensitic microstructures (41), containing large amounts of < 35 nm precipitates. The microstructure of Ti-11Al-0.5Y (nominal at%) also exhibited a population of very refined precipitates, but some specimens a much greater population of non-martensitic alpha grains than others. In contrast, the alloys containing lanthanum, neodymium, gadolinium or lutetium had almost completely recrystallized, and exhibited larger quantities of > 50 nm intercellular and intergranular precipitates, and relatively smaller quantities of more homogeneously dispersed, < 35 nm precipitates. It appears that the alloys in this latter group retain relatively less rare earth in metastable solid solution when splat quenched to thicknesses of 80-125 um, and consequently form fewer refined precipitates upon aging.

Erbium. Specimens of Ti-11Al-0.5Er (nominal at%) were used as the basis of microstructural comparison for the other seven alloys, based on the well documented effectiveness of erbium in forming second phase dispersions in rapidly solidified and aged titanium base alloys (8,18,19,38,41,42). The grain structure of Ti-11Al-0.5Er, aged at 800 °C for 0.25 or 4 hr, was not markedly different from that of the as-splat-quenched specimens, in that it was almost completely martensitic with a few relatively equiaxed alpha grains (Figures 20,21). A few precipitate-free zones bordered by coarser precipitates could be observed. These appeared to have been formed by grain boundary migration, in a manner similar to that reported in rapidly-solidified and aged Ti_3Al + Er (42). Larger ($\geq$ 50 nm) precipitates were visible throughout the microstructure, with a size range and distribution which suggested that most of these were present prior to aging. Their dispersion was not as obviously intercellular in this 100 um-thick specimen as it was in the thicker as-splat-quenched specimen shown in Figures 7-10. However, it was difficult to tell to what extent this was an apparent effect, due to the greater depth of view in the latter case; or a real effect, due to the slower cooling rate experienced by the thicker (175 um) as-splat-quenched specimen. There were a few areas where the pattern of the dispersion suggested precipitation on prior-beta grain boundaries (left side, Figure 21B). Quantitative analysis of diffraction patterns obtained from several of the larger precipitates indicated that they were equilibrium-structure erbium sesquioxides (Figure 22), as found in the as-splat-quenched specimens, and in agreement with similar observations in laser-processed and aged Ti-0.7at%Er (38). However, none of the erbium carbides described in (38) were detected. Their absence is consistent with the intrinsically low carbon content maintained in these alloys.

An increase in aging time from 0.25 to 4 hours at 800 °C produced no distinguishable change in the microstructure of Ti-11Al-0.5Er. The primary effect of aging at 800 °C for 0.25 or 4 hours was the formation of a population of much smaller (<35 nm) and more homogeneously distributed precipitates. These formed a generally intracellular dispersion, and sometimes appeared to have precipitated at lower-energy sites such as martensite plate boundaries and dislocations (Figure 23-28). They were predominately platelike in morphology when viewed parallel to the $[1\bar{1}00]$ or $[11\bar{2}0]$ directions of the matrix, and exhibited strong adjacent matrix strain contrast under two-beam imaging conditions with g = 0002 (Figures 26,28,29). These data are consistent with observations of "Type I" erbia, precipitated in laser processed and aged Ti-0.7at%Ti (8,38,43); and with observations of < 30 nm yttria precipitates in HIP-consolidated Ti-1at%Y (44). A much smaller number of precipitates within the < 35 nm size population could be distinguished from this first group, in that they displayed strong matrix strain contrast when imaged under two-beam conditions with $g = 11\bar{2}0$, rather than g = 0002 (Figure 30). Following the convention used by previous investigators (8,38,43), precipitates which displayed this type of image contrast were designated "Type II". The matrix strain contrast associated with both Type I and Type II precipitates observed in this and in previous investigations (22,38,43,44) strongly suggests that they are semi-coherent. The coherency exists between {111} of either precipitate, and (0001) or $\{11\bar{2}0\}$ of the matrix, respectively. This contrast was not caused by elastic strains due to the mismatch in thermal expansion coefficients between the erbia and matrix, since it was entirely absent for Type II precipitates which were located near those of Type I orientation when both were imaged with two beam conditions, g = 0002; and vice versa when $g = 11\bar{2}0$.

The diffraction patterns formed by each of these two families of < 35 nm precipitates could be distinguished from one another most readily by observing one of the major zone axis patterns of the HCP matrix. As an example, Figure 31 shows a $[1\bar{1}00]$ matrix selected area diffraction pattern which contains Type I and Type II erbia precipitate spots. These can be indexed as shown in the superimposed schematic plots of Figure 32; which accurately shows the relative spot positions of the three phases present. However, it does not reflect the complexity of the experimental patterns caused by double diffraction; nor does it reflect the invisibility of many spots due to structure factor effects (21), or the low volume fraction of Type II precipitates, of which only one variant is in contrast.

Selected area diffraction patterns of the [0001], $[11\bar{2}0]$, $[1\bar{1}00]$ and $[1\bar{1}02]$ matrix zone axes which also contained precipitate spots (e.g., Figures 28,29) were quantitatively analyzed by assuming that the matrix lattice parameters were those reported for Ti-11at%Al: a = 0.2925 nm; c = 0.4675 nm (45). The results indicated that the Type I precipitates were cubic (Figures 25,26), with a lattice parameter of a = 1.012 $\pm$ 0.03 nm, in close agreement with the value of 1.015 nm previously reported (38). The crystallographic relationship of the Type I precipitates to the alpha (HCP) matrix also agreed with previous observations of erbia precipitates in Ti-0.7 at% Er (38,43): $[11\bar{2}]$ erbia || $[1\bar{1}00]$ matrix; and [111] erbia || [0001] matrix. The Type II precipitates were determined to be cubic, with a lattice parameter equal to that of equilibrium-structure erbium sesquioxide (1.055 nm). Their

crystallographic orientation with respect to the matrix was [11$\bar{2}$] erbia || [1$\bar{1}$00] matrix and (1$\bar{1}$0) erbia || (0001) matrix (Figure 30), again in agreement previous observations (38,43). Although Type I and Type II precipitates have different orientations, in both cases it is the {111} planes which appear to be coherent with the matrix, as described previously.

The presence of extra Type I spots due to double diffraction in major matrix zone axis patterns significantly increased their complexity. The strongest Type I diffraction spots observed in <1$\bar{1}$00> zone axis selected area diffraction patterns were usually $\bar{4}$40 or 222, while the strongest type II spot was usually 222. These observations are consistent with the strong fourth and second order intensities predicted by the structure factors of the M_2O_3 sesquioxides (21), which have space group $I(2_1/a)3$, (often shortened to Ia3). Consequently, it appears reasonable to assume that the Type I, as well as the Type II, precipitates are erbium sesquioxides (38,43). If both Type I and Type II precipitates were present in the same general region of the microstructure, {11$\bar{2}$0} matrix Kikuchi bands usually had strong $\bar{4}$40 Type I and observable 222 Type II spots associated with them, as suggested by the Type I erbia-matrix orientation relationship described previously. Thus {11$\bar{2}$0} matrix Kikuchi bands proved useful to orient particular areas of a specimen for precipitate zone axis patterns (Figure 33), and to obtain separate Type I and Type II erbia dark field images from the same area (Figures 34-36).

Terbium. Specimens of Ti-11Al-0.5Tb (at%), splat quenched to a thickness of 100 um thickness and aged at 800 °C, displayed a grain structure and precipitate distribution (Figure 37) similar to that of Ti-11Al-0.5Er. There were, however, many more precipitate free zones scattered throughout the microstructure, located both in areas where grain boundary migration had occurred during aging (Figure 38), and at prior beta grain boundary sites (Figures 39,40). As in the case of the erbium-containing alloy, aging at 800 °C produced large quantities of < 35 nm precipitates (Figures 40,41), most of which displayed the matrix strain contrast (Figure 40) and crystallographic orientation (Figures 42,43) characteristic of the Type I oxides described previously. This was somewhat surprising, in view of the multiplicity of equilibrium oxide stoichiometries known to occur in the terbium-oxygen system (46,47). Type II oxides of the same precipitate-matrix orientation observed in aged Ti-11Al-0.5Er were also observed, again in much smaller quantities than those with Type I orientation. The lattice spacings of the oxide precipitates were determined and cross-checked using selected area diffraction patterns from several major matrix zone axes. The Type I precipitates were cubic, a = 1.035 $\pm$ 0.003 nm; while those of Type II orientation were also cubic, with the lattice parameter of equilibrium-structure Tb_2O_3 (a = 1.07 nm). This diffraction data is exemplified by the precipitate diffraction patterns coincident with the [1$\bar{1}$00] and [0001] matrix zone axis patterns in Figures 42 and 43, which are similar those from rapidly solidified and aged Ti-0.7at%Er published previously (38,43). It should be noted that almost all of the precipitate spots in Figure 43 are from {440} of Type I terbia, extensively replicated by double diffraction.

Dysprosium. The microstructure of splat quenched Ti-11Al-0.5Dy after aging at 800 °C closely resembled that of aged Ti-11Al-0.5Er. However, the specimen shown in Figure 44 was splat quenched to a relatively smaller thickness (80 um), and thus experienced a more rapid cooling rate, than the erbium-containing specimens described earlier. The more rapid cooling is reflected by the finer scale of the martensitic structure. None of the non-martensitic alpha grains reported in rapidly solidified Ti-6Al-4V (wt%) (37), and observed in the aged Ti-11Al-0.5Er were present (Figure 44). Despite this relatively rapid cooling rate, presumably $\geq 10^6$ at the solidus temperature, it did not appear that all of the dysprosium had been retained in supersaturated solid solution. The size range, spatial distribution and random crystallographic orientation of the larger precipitates (Figure 45) suggested that they had been present in the as-splat-quenched specimen. In fact, the precipitates in the >50 nm size range were somewhat larger than those observed after the same heat treatment in Ti-11Al-0.5Er (Figures 20,24), which suggested that the relatively greater amount of grain boundary surface may have accelerated their coarsening. As in the erbium and terbium alloys, aging at 800 °C caused the widespread formation of <35 nm Type I precipitates, with the characteristic lattice strain contrast (Figure 46) and crystallographic orientation with respect to the matrix (Figure 47) described previously. The lattice parameter of the cubic Type I precipitates was determined to be 1.025 $\pm$ 0.003 nm, somewhat less than the lattice parameter of (cubic) equilibrium-structure Dy_2O_3 (a = 1.067 nm).

Yttrium. As mentioned earlier in this section, aging the Ti-11Al-0.5Y (at%) alloy at 800 °C consistently produced a large population of unusually small Type I precipitates in all specimens examined. However, there was a wide variation in the number of non-martensitic alpha grains present in the post-age grain structure in different specimens. In some instances, these grains were relatively large, yet did not appear to have formed by recrystallization, in that they contained a uniform, bimodal size distribution of precipitates with no evidence of precipitate-free zones formed by grain boundary migration (Figure 48). Other thin foils cut from the same splat-quenched and annealed specimen contained a larger volume fraction of martensite (Figure 49). In all cases, the precipitate distribution was largely independent of grain structure variations. Those in the larger size range were incoherent, equilibrium-structure yttrium sesquioxide, many of which were distributed in a pattern which suggested that they had precipitated at intercellular sites (Figure 50A). The other group consisted primarily of a more homogeneous distribution of unusually small (<20 nm) Type I precipitates which exhibited matrix strain contrast under two-beam conditions when g = 0002 (Figures 50B,51,52A), mixed with a lower quantity of Type II precipitates which exhibited matrix strain contrast when g = $11\bar{2}0$ (Figures 52B,53). The distinctive crystallography of these two forms of yttrium oxide was determined by analysis of [$1\bar{1}00$] (matrix) selected area diffraction patterns from areas which contained both types of semi-coherent yttria (Figures 54,55). These SADP's were qualitatively very similar to those obtained from the other aged alloys described previously.

Second Alloy Group.

The 800 °C aged microstructure of the alloys which contained La, Nd, Gd or Lu displayed generally characteristics of the four alloys just described, but the distribution of < 35 nm precipitates formed during aging was generally less homogeneous, and there was evidence for less supersaturation of the rare earth component prior to aging.

Gadolinium. The grain structure and precipitate distribution in a specimen of Ti-11Al-0.5Gd (nominal at%), splat quenched to 125 um thickness and aged at 800 °C for 0.25 hr, are shown in Figure 56. This microstructure illustrates the consistent observation that virtually no martensite was retained in any specimen aged at this temperature. The precipitate size distribution was bimodal, and most of the larger (>50 nm) precipitates had retained an intercellular pattern (Figure 57). Precipitates of somewhat smaller size were distributed in a pattern indicative of precipitation on prior beta grain boundaries (Figure 58). Some of the intercellular precipitates were determined by selected area diffraction to have the equilibrium low-temperature (cubic) structure of Gd_2O_3, a = 1.081 nm (39), while others retained the high-temperature (monoclinic) structure observed in as-splat-quenched specimens. Since the grain structure consisted of relatively equiaxed alpha, it is reasonable to assume that this was formed by recrystallization of the as-quenched martensite. However, although there was evidence for grain boundary migration over short distances (Figure 57), recrystallization would involve grain boundary migration over many micrometers, and the second phase particle distribution did not exhibit the large precipitate-free zones and coarsened gadolinia which would result (42). Consequently, if general recrystallization of the microstructure had occurred at 800 °C, it appears probable that the smaller (<35 nm) precipitates formed subsequently, after the moving grain boundaries had passed. Matrix strain contrast could be observed under many different imaging conditions in the immediate vicinity of many of the larger intercellular precipitates. In some cases dislocation loops had been generated at the particle-matrix interface (Figure 59). This evidence of high levels of stress at the particle-matrix interface appears to have been caused by the different thermal expansion coefficients of gadolinia (48) and alpha titanium.

A population of much smaller (<30 nm) and more homogeneously distributed precipitates had formed in intercellular locations after aging at 800 °C for 0.25 hr. They were, however, noticeably absent near grain boundaries, intercellular precipitates, and precipitates at prior-beta grain boundaries (Figures 59,60). They exhibited strong strain contrast under appropriate two-beam imaging conditions, indicative of semi-coherency (Figures 60-62). As with the previous alloys, selected area diffraction patterns calibrated from the matrix lattice parameters were used to determine that the majority of the small precipitates were cubic, with a lattice parameter of 1.045 $\pm$ 0.003 nm. Again, the crystallographic relationship of these precipitates to the HCP alpha matrix was the same as the "Type I" erbia precipitates observed in laser-processed and aged Ti-0.7at%Er (8,39): $[11\bar{2}]$ ppt || $[1\bar{1}00]$ matrix; $[\bar{1}10]$ ppt || $[11\bar{2}0]$ matrix; and [111] ppt || [0001] matrix (Figures 63,64).

Lutetium. Specimens of the Ti-11Al-0.5Lu (at%) alloy were aged for 4 hours at 800 °C in order to use the same sample to evaluate both the precipitate dispersion and its resistance to coarsening (Figure 65). The microstructure contrasted sharply to that of Ti-11Al-0.5Er (at%) after the same aging conditions, in that no martensitic grain structure was retained, and very few precipitates in the smaller size range (<35 nm) were present. The general characteristics of the precipitate in the largest size range (> 100 nm) were similar to those observed in the other aged specimens. In this alloy, some had begun to form facets after 4 hours of aging, but they did have any consistent orientation relationship with the matrix, nor did they display any evidence of coherency with the matrix. Although their distribution was not as obviously intercellular as that of similar particles in aged Ti-11Al-0.5Gd, these larger precipitates most probably formed during splat quenching rather than during aging. A third group of precipitates was apparent, which had not been observed in any of the other aged alloys. These had a size range of approximately 35-140 nm, and were noticeably faceted, with edges parallel to $\{1\bar{1}00\}$ of the matrix when viewed in the [0001] matrix direction (Figure 66). Analysis of selected area diffraction patterns combined with dark field images (Figures 67-69) showed that these precipitates were Type I, with $\{111\} \parallel (0001)$ and $\langle\bar{1}10\rangle \parallel \langle11\bar{2}0\rangle$. The coincident <111> ppt (Type I) - [0001] matrix zone axis patterns in Figure 67 are very similar to those observed in the other alloys (Figure 43), in that virtually all of the precipitate spots are from {440} Type I planes, parallel to $\{11\bar{2}0\}$ of the matrix, and replicated extensively by double diffraction from strong matrix spots. Dark field images of the area of Figure 66 were formed with $g = \bar{4}40$, Type I (Figure 68), for which both Type I variants should be in contrast; and with g = 222, Type II (Figure 69), which shows one of three Type II variants. The reason for the lack of contrast from the smallest (< 20 nm) precipitates in the upper left of Figure 54 in either dark field image is not immediately apparent, although they might be another variant of Type II. The lattice parameter of the cubic Type I precipitates was determined from these and other selected area diffraction patterns to be 1.00 ± 0.03 nm; while that for Type II matched that of equilibrium structure Lu_2O_3, a = 1.039 nm.

Lanthanum and Neodymium. Figures 70 and 71 show the grain structure and precipitate distribution in Ti-11Al-0.5La and Ti-11Al-0.5Nd (nominal at%), splat quenched to 94 um and 100 um thicknesses, respectively, and aged at 800 °C for 0.25 hr. The post-age microstructure of these alloys was similar to that of the Ti-11Al-0.5Gd alloy described earlier. No martensitic structure was retained, and the pattern formed by many of the larger particles suggested that they had precipitated at intercellular sites. Precipitate-free zones were much in evidence, and the population of <35 nm precipitates was noticeably low compared to the other alloys examined. Further characterization of these precipitates has not been attempted at this point in the research program. The low volume fraction and inhomogeneous distribution of the smaller precipitates suggests that their potential contribution to high temperature strength would not be of much technological interest. However, the second phases in rapidly-solidified and aged titanium base alloys containing lanthanum have been reported to display some unique characteristics, compared to the other rare earth elements (43). In as-solidified microstructures, discrete particles of pure lanthanum, rather than lanthanum oxide, have been observed. The precipitates which formed upon

aging were reported to be hexagonal lanthanum sesquioxides, with the same crystallographic orientation as the HCP matrix.

Orientation and Structure of Precipitates.

As described previously, the <35 nm precipitates which formed as a result of aging at 800 °C for 0.25 or 4 hours exhibited the same two types of orientation relationship with respect to the HCP matrix in each of the alloys which was characterized in detail (nominally 0.5 at% Y, Gd, Tb, Dy, Er and Lu, respectively). In each case, the majority of these precipitates were cubic, with a crystallographic orientation consistent with that described as Type I in rapidly solidified and aged Ti-Er alloys (20,38,43). In addition, each of these six aged alloys contained a small quantity of cubic precipitates with an orientation described by (20,38 and 43) as Type II. These two precipitate-matrix orientation relationships are depicted stereographically in Figure 72. The lattice parameters of both the cubic Type I and Type II precipitates in the alloys containing Gd, Tb, Dy, Er and Lu were experimentally determined from calibrated selected area diffraction patterns (usually the $\langle 1\bar{1}00\rangle$, $\langle 11\bar{2}0\rangle$ and [0001] zone axis patterns. In these five cases, the measured lattice parameter of the Type II precipitates matched that of the cubic sesquioxide of the rare earth element added to that alloy. The Type I lattice parameter was in each case consistently several percent less than this, as shown in Figure 73. The only previous determination of a Type I rare earth oxide lattice parameter was 1.015 nm for erbia (38), as described previously. It appears reasonable to assume that all of the Type I precipitates are oxides closely related to the Type II sesquioxides (38).

DISCUSSION

Specimen Cooling Rates

When rapid solidification is achieved by splat quenching, the rate of heat flow is controlled by the heat transfer coefficient between the alloy and the substrate (49). Based on the analyses made by Jones (35) and Ruhl (50),and the data reported by Broderick et al (37), it is estimated that a 100 um thick splat should have experienced an initial cooling rate of 10^5 to 10^6 °C/s at temperatures near the solidus. Within the range of splat-quenched specimen thicknesses investigated in here (65-175 um), the solidification rate had relatively little effect on the refinement of the oxide dispersions formed by aging, compared to the differences caused by changing the rare earth component of the various alloys.

Relative Effectiveness of the Rare Earth Elements in Forming Oxide Dispersions

Comparison of the microstructures of the splat quenched and aged alloys demonstrated that, despite their chemical similarity, yttrium and many of the lanthanide elements do not form equivalent oxide dispersions in Ti-11at%Al when processed similarly. Despite some variation in the solidification rate of the specimens, the microstructure of the various alloys investigated here consistently demonstrated that yttrium, terbium, dysprosium, and erbium could be supersaturated in Ti-Al by rapid solidification to a greater degree than the other four lanthanides, In fact, this was true even when the thickness of a particular specimen indicated that the alloy had solidified more rapidly (80 um, as-splat-quenched Ti-11Al-0.5Gd, Figure 14) than most of the others examined. The qualitative figure of merit for all alloys was the refinement of the oxide dispersion formed after aging at 800 °C for 0.25 h. However, many alloys which contained relatively few < 35 nm precipitates after aging also exhibited intragranular precipitation in the as-splat-quenched state, and thus less complete supersaturation.

Sastry et al (24) have described the structure and properties of a series of rapidly solidified and aged titanium-rare earth alloys, utilizing 0.34-1.0 at% yttrium, lanthanum, cerium, neodymium, gadolinium, dysprosium or erbium. Both the accuracy and the control of total interstitial content in these alloys is open to question, as is the identification of the second phases forming the dispersions. These issues have been discussed at some length by Konitzer et al (38). More detailed characterization of the particles in alloys of similar composition and processing, has been described in this report and in the recent literature (26,38,41). Based on these data, it is quite probable that the dispersions in all of these alloys were composed primarily of rare earth oxides (38). Thus, the mean particle diameters observed in Ti-Y, Ce, La, Nd, Gd, Dy or Er after aging at 800 °C for 1000 hours (Ref. 24, Table VI) provide a basis of comparison with the results of this investigation with respect to the relative refinement of the oxide dispersions formed by the rare earth elements. Ti-Y, Ti-Er, Ti-Dy, Ti-Nd and Ti-La were judged to form refined dispersions which were relatively resistant to coarsening. This agrees with the results of the present study in the first

three cases, but not in the latter two. There is some question as to how well the particle size dispersions were characterized in (24) since only a single mean particle diameter is reported, yet it is quite probable that the particle size distribution was at least bimodal. The quality and magnification of the transmission and scanning electron micrographs in (24) do not generally permit a direct comparison with those presented here, although there does appear to be larger population of <50 nm precipitates in Ti-0.7at%La. The conclusion by (24) that the refined (<50 nm) precipitates in alloys of titanium and any one of several rare earth elements have lattice parameters indicative of the presence of carbon was not supported by the results of this or other (38) investigations. Similarly, no evidence for the presence of aluminum-rare earth intermetallic precipitates, reported in melt-spun and HIPed Ti-Al-Er (28) was found.

Some additional, but very limited comparisons of the oxide dispersions formed by different rare earth elements in rapidly solidified titanium have appeared in recent publications. Gigliotti, et al (32) noted that the most stable rare earth oxides should be the most technologically suitable, with stability presumably based on the relative heat of formation. This same research group conducted an extensive evaluation of various particle dispersions for strengthening rapidly-solidified titanium alloys based on Ti-6242, and chose alloys in which yttria or erbia are formed upon aging for final evaluation of mechanical properties (51). In this and other reports, more emphasis has been placed (understandably) on the resistance of various dispersed compounds to coarsening than on comparisons of dispersion refinement. However, concern for the stability of a dispersion necessarily implies that its size and spatial dispersions were technologically attractive when first formed. Two recent reviews of rapidly-solidified titanium alloy development have reported that Y_2O_3, Er_2O_3 and cerium oxysulfides form particularly stable dispersions (52,53).

The results of the present investigation strongly indicate that none of the individual rare earth elements is superior to erbium in forming a refined and stable oxide dispersion in rapidly-solidified alpha titanium-aluminum alloys.

Rationale for the Existence of Type I vs. Type II Oxides

The occurrence of the Type I rare earth oxides as the most common <50 nm precipitate to form at 800 °C in each of the alloys investigated is the most surprising result of this investigation to date. For the alloys to which yttrium or any of several lanthanide elements have been added, the Type I precipitates were observed to have a consistently unique crystallographic orientation (Figure 72) and negative deviation from the lattice parameter of the corresponding equilibrium-structure cubic sesquioxide (Figure 73). A mechanism to explain this phenomenon in Ti-Er(-O) alloys has been proposed by Konitzer et al (38), by which the Type I particles initially precipitate during aging as HCP erbium with (0001) Er || (0001) Ti. These immediately oxidize to form a cubic structure, assumed to be a sub- stoichiometric form of cubic Er_2O_3, with {111} of the cubic erbia structure forming from and parallel to (0001) of the parent erbium. The <50 nm Type II particles, on the

other hand, were presumed to precipitate directly from the matrix as equilibrium-structure C-type sesquioxides, with their closest-packed plane, {110}, || (0001) titanium.

The results of the present investigation suggest that this model might also apply when either yttrium, gadolinium, terbium, dysprosium or lutetium is substituted for erbium. The C-type (cubic) rare earth sesquioxides have been reported to exist in a sub-stoichiometric form (54). Nevertheless, it is still surprising that suboxides should exhibit a constant, rather than gradually increasing, lattice parameter over a range of aging conditions. In Ti-Er, the quantity of Type II precipitates was observed to increase with increasing aging time and/or temperature (38), presumably favored at the expense of Type I by the ready availability of oxygen. An similar increase in the population of small Type II precipitates the alloys of the present program has thus far not been observed, but specimens aged for greater times and temperatures than 800 °C and 4 hours have not yet been fully evaluated. There has been no indication to date that aluminum plays a role in the formation of Type I oxides. It is anticipated that the coarser precipitates produced by more extensive aging will be somewhat easier to characterize, and thus provide additional information concerning these issues.

CONCLUSIONS

1. Refined rare earth oxide dispersions in alpha titanium-aluminum-rare earth alloys can be achieved by arc melting, splat quenching and aging under highly purified argon. Specimens of these alloys can be repeatedly produced with controlled rapid solidification rates and compositions.

2. Of the eight Ti-11Al-0.5 (at%) rare earth alloys that were investigated, the most refined dispersions of semi-coherent rare earth oxides were formed by aging at 800 °C in alloys containing yttrium, terbium, dysprosium or erbium. The terbium-containing alloy contained more precipitate-free zones at grain boundaries than the other three. Alloys which contained lanthanum, neodymium, gadolinium or lutetium retained relatively less of the rare earth element in supersaturated solid solution, and contained relatively lower volume fractions of refined precipitates after aging at 800 °C.

3. Intercellular precipitation of rare earth oxides was observed in all specimens of all alloys over an as-splat-quenched thickness range of 65-175 um. Precipitation on prior beta grain boundaries was frequently observed in these specimens.

4. Both the cubic and monoclinic equilibrium structures of Gd_2O_3 and Dy_2O_3 were observed in as-splat-quenched alloys which contained Gd or Dy.

5. Most of the precipitates formed in the eight alloys by aging at 800 °C were cubic rare earth oxides, < 35 nm in maximum dimension. These precipitates were designated Type I for consistency with the nomenclature of previous investigations. They were semi-coherent, and were determined to have the following crystallographic relationship with the HCP matrix: $\{11\bar{2}\}$ REO || $\{1\bar{1}00\}$ matrix, and <111> REO || [0001] matrix. In alloys containing nominally 0.5 at% Y, Er or Dy, a much smaller quantity of semi-coherent, equilibrium-structure sesquioxides were also observed to precipitate. These were designated Type II, and had the following crystallographic orientation: $\{11\bar{2}\}$ REO || $\{1\bar{1}00\}$ and $\langle 1\bar{1}0\rangle$ REO || [0001]. For both Type I and Type II, the rare earth oxide plane which was coherent with the HCP matrix was {111}.

6. The microstructure of Ti-11Al-0.5Y (at%), splat quenched to a thickness of 125 um and aged at 800 °C for 0.25 or 4 hr, was particularly noteworthy in that it displayed a very refined, bimodal oxide dispersion, yet all specimens were either partially or completely recrystallized.

7. In all alloys, those areas of the microstructure which did not recrystallize during aging exhibited accelerated oxide coarsening near grain boundaries. Similarly, grain boundary migration through areas in which < 35 nm precipitates had formed caused accelerated oxide coarsening and the formation of precipitate-free zones.

REFERENCES

1. G. W. King and H. G. Sell, "The Effect of Thoria on the Elevated-Temperature Properties of Recrystallized High-Purity Tungsten," Trans. TMS-AIME, 1965, vol. 233, pp. 1104-1113.

2. B. A. Wilcox and A. H. Clauer, "Creep of Thoriated Nickel above and below 0.5 T_m," Trans. TMS-AIME, 1966, vol. 236, pp. 570-580.

3. J. S. Benjamin, "Dispersion Strengthened Superalloys by Mechanical Alloying," Met. Trans., 1970, vol. 1 pp. 2943-2951.

4. J. S. Benjamin and M. J. Bomford, "Effect of Oxide Volume Fraction and Particle Size on Elevated Temperature Strength of a Dispersion Strengthened Alloy," Met. Trans., 1974, vol. 5 pp. 615-621.

5. R. H. Hiltz, Jr. and N. J. Grant, "The Elevated Temperature Characteristics of Internally Oxidized Titanium-Cerium Alloys," Trans. AIME, 1958, vol. 212, pp. 383-387.

6. C. F. Dixon and H. M. Skelly, "Dispersion Strengthening Titanium with Refractory Oxides," Canadian Metall. Quart., 1972, vol. 11, pp. 491-495.

7. R. C. Waugh, "Suitable Oxides for Dispersion Strengthening of Titanium Alloys," Int. J. Powder Met. & Powder Tech., 1976, vol. 12, pp. 85-89.

8. D. G. Konitzer et al., "The Production of Ultrafine Dispersions of Rare Earth Oxides in Ti Alloys Using Rapid Solidification," Rapidly Quenched Metals, Vol. I, S. Steeb and H. Warlimont, eds., Elsevier Science Publishers B.V., London, 1985, pp. 953-956.

9. M. J. Buczek, G. S. Hall, S. R. Seagle, and H. B. Bomberger, "Grain Refinement of Titanium Alloys," Final Technical Report AFML-TR-74-255, RMI Co., November, 1974.

10. I. G. Wright and A. H. Clauer, "Study of Intermetallic Compounds, Task A: Dispersion-Hardened TiAl," Report AFML-TR-76-107, Battelle Columbus Laboratories, July, 1976.

11. O. Kubaschewski-vonGoldbeck, "Part II: Phase Diagrams," Titanium: Physico-Chemical Properties of its Compounds and Alloys, K. L. Komarek, ed., International Atomic Energy Agency, Vienna, 1983, pp. 75-197.

12. K. A. Gschneidner, Jr., N. A. Kippenhan, and O. D. McMasters, "Thermochemistry of the Rare Earths," Rare Earth Information Center, Institute for Atomic Research, Iowa State University, 1973.

13. R. P. Simpson, "Controlled Weld-Pool Solidification Structure and Resultant Properties with Yttrium Inoculation of Ti-6Al-6V-2Sn Welds," Welding J. 1977, vol. 56, pp. 67s-77s.

14. R. E. Shalin, S. G. Glasunov, and A. I. Khorev, "Advanced Trends in Developing High-Strength Titanium Alloys," Titanium '80, Science and Technology, Vol. 2, H. Kimura and O. Izumi, eds., The Metallurgical Society of AIME, Warrendale, PA, 1980, pp. 1265-1275.

15. B. B. Rath et al., "The Influence of Erbium and Yttrium Additions on the Microstructure and Mechanical Properties of Titanium Alloys," pp. 1185-1196, ibid.

16. J. A. Miller and G. Brodi, "Consolidation of Blended Elemental Ti-6Al-4V Powder to Near Net Shapes," AFML-TR-4028, March, 1979.

17. C. A. Kelto et al., "Titanium Powder Metallurgy - A Perspective," Powder Metallurgy of Titanium Alloys, F. H. Froes and J. E. Smugeresky, eds., The Metallurgical Society of AIME, Warrendale, PA, 1980, pp. 1-19.

18. J. C. Williams, "Precipitation in Titanium-Base Alloys," Precipitation Processes in Solids, K. C. Russell and H. I. Aaronson, eds., The Metallurgical Society of AIME, Warrendale, PA, 1978, pp. 191-221.

19. B. B. Rath, R. J. Lederich, and J. E. O'Neal, "Effect of Rare Earth Additions on the Grain Refinement in Titanium," Grain Boundaries in Engineering Materials, J. L. Walter, J. H. Westbrook and D. A. Woodford, eds., Claitor's Publ. Div., Baton Rouge, LA, 1975, pp. 39-42.

20. D. G. Konitzer and H. L. Fraser, "An Example of the Use of Combined Techniques of Analytical Transmission Electron Microscopy for Phase Identification," Microbeam Analysis - 1984, K. F. J. Heinrich, ed., San Francisco Press, San Francisco, 1982, pp. 393-398.

21. D. G. Konitzer, B. C. Muddle and H. L. Fraser, "A Comparison of the Microstructures of As-Cast and Laser Surface Melted Ti-8Al-4Y," Met. Trans. A, 1983, vol. 14A, pp. 1979-1988.

22. D. G. Konitzer, B. C. Muddle, and H. L. Fraser, "Formation and Thermal Stability of an Oxide Dispersion in a Rapidly Solidified Ti-Er Alloy," Scripta Met., 1983, vol. 17, pp. 963-966.

23. S. H. Wang, "Rapidly Solidified Ti Alloys Containing Novel Additives," J. Metals, 1984, vol. 36, No. 4, pp. 34-40.

24. S. M. L. Sastry, P. J. Meschter, and J. E. O'Neal, "Structure and Properties of Rapidly Solidified Dispersion-Strengthened Titanium Alloys: Part I. Characterization of Dispersoid Distribution, Structure and Chemistry," Met. Trans. A, 1984 vol. 15A, pp. 1451-1463.

25. D. G. Konitzer and H. L. Fraser, "The Production and Thermal Stability of a Refined Dispersion of Er_2O_3 in Ti_3Al Using Rapid Solidification Processing," High-Temperature Ordered Intermetallic Alloys, C. C. Koch, C. T. Liu, and N. S. Stoloff, eds., Materials Research Society, Pittsburgh, PA, 1985, pp. 437-442.

26. D. B. Snow, "Structure and Mechanical Properties of Laser-Consolidated Ti-6Al-4V and Ti-6Al-2Sn-4Zr-6Mo with Rare Earth Element Additions," Laser Processing of Materials, K. Mukherjee and J. Mazumder, eds., The Metallurgical Society of AIME, Warrendale, PA, 1985, pp. 83-98.

27. R. G. Rowe et al., "Microstructural Study of Rapidly Solidified Titanium Containing Erbium and Boron," Rapidly Solidified Materials, P. W. Lee and R. S. Carbonara, eds., ASM International, Metals Park, OH, 1985, pp. 107-114.

28. C. S. Chi and S. H. Wang, "Microstructures and Mechanical Property of Rapidly-Solidified Ti-5Al-4.5La and Ti-5Al-5.4Er Alloys," Mechanical Behavior of Rapidly Solidified Materials, S. M. L. Sastry and B. A. MacDonald, eds., The Metallurgical Society of AIME, Warrendale, PA, 1986, pp. 231-245.

29. R. G. Rowe and E. F. Koch, "Rapidly Solidified Titanium Alloys Containing Cerium Sulfide and Oxysulfide Dispersions," Rapidly Solidified Materials, P. W. Lee and R. S. Carbonara, eds., ASM International, Metals Park, OH, 1985, pp. 115-127.

30. S. M. L. Sastry, T. C. Peng, and L. P. Beckerman, "Structure and Properties of Rapidly Solidified Dispersion Strengthened Titanium Alloys: Part II. Tensile and Creep Properties," Met. Trans. A, 1984, vol. 15A, pp. 1465-1474.

31. D. A. Koss, "Advanced Processing and Properties of High Performance Alloys", Technical Report No. 3, Contract No. N00014-85-K-0427, Michigan Technological Univ., Houghton, MI 49931, November 29, 1985.

32. M. F. X. Gigliotti et al., "Tensile and Creep Properties of Rapidly Solidified Titanium Alloys Containing Complex Matrices and Fine Dispersions," Rapidly Solidified Alloys and Their Mechanical and Magnetic Properties, B. C. Giessen, D. R. Polk and A. I. Taub, eds., Materials Research Society, Boston, MA, 1986, pp. 343-352.

33. M. F. X. Gigliotti, "Mechanical Evaluation of Rapidly Solidified Titanium Alloys Containing Fine Dispersiods," Titanium Rapid Solidification Technology, F. H. Froes and D. Eylon, eds., The Metallurgical Society of AIME, Warrendale, PA, 1986, pp. 141-151.

34. T. B. Reed and E. R. Pollard, "Tri-Arc Furnace for Czochralski Growth with a Cold Crucible," J. Crystal Growth, 1968, vol. 2, pp. 243-247.

35. Jones H., "Splat Cooling and Metastable Phases," Rep. Prog. Phys., 1973, vol. 36, pp. 1425-1497.

36. P. M. Strocchi and M. Socci, "Selective Evaporation of Some Titanium Alloy Components in the Electron Beam Furnace", Titanium and Titanium Alloys, Vol. I, J. C. Williams and A. F. Belov, eds., Plenum Press, New York, 1982, pp. 197-208.

37. T. F. Broderick et al., "The Effect of Cooling Conditions on the Microstructure of Rapidly Solidified Ti-6Al-4V," Met. Trans. A, 1985, vol. 16A, pp. 1951-1959.

38. D. G. Konitzer, J. T. Stanley, M. H. Loretto and H. L. Fraser, "The Nature of Dispersed Phases in Ti-0.7at%Er Prepared by Rapid Solidification Processing," Acta Met., 1986, vol. 34, pp. 1269-1277.

39. F. A. Shunk: Constitution of Binary Alloys, Second Supplement, MCGraw-Hill Book Co., New York, NY, 1969, pp. 305-306, 379.

40. K. A. Gscheidner, Jr.: Rare Earth Alloys, D. Van Nostrand Co., New York, NY, 1961, p. 243.

41. D. B. Snow and A. F. Giamei, "Rare Earth Oxide Dispersions in Rapidly Solidified Titanium-Aluminum Alloys," Rapid Solidification Titanium Technology," F. H. Froes and D. Eylon, eds., The Metallurgical Society of AIME, Warrendale, PA, 1986, pp. 153-164.

42. J. A. Sutliff and R. G. Rowe, "Rare Earth Oxide Dispersoid Stability and Microstructural Effects in Rapidly Solidified Ti_3Al and Ti_3Al-Nb," Rapidly Solidified Alloys and Their Mechanical and Magnetic Properties, B. C. Giessen, D. R. Polk and A. I. Taub, eds., Materials Research Society, Boston, MA, 1986, pp. 371-376.

43. S. A. Court, et al., "Laser Surface Melting of Ti Alloys Containing Er or La," Titanium Rapid Solidification Technology, F. H. Froes and D. Eylon, eds., The Metallurgical Society of AIME, Warrendale, PA, 1986, pp. 165-176.

44. S. Naka, M. Marty and H. Octor, "Oxide-dispersed titanium alloys Ti-Y prepared with the rotating electrode process," J. Matl. Sci., 1987, vol. 22, pp. 887-895.

45. P. Rogl, "Part III. Crystal Structure and Density Data," Titanium: Physico-Chemical Properties of its Compounds and Alloys, K. L. Komarek, ed., International Atomic Energy Agency, Vienna, 1983, p. 245.

46. R. P. Elliott: Constitution of Binary Alloys, First Supplement, MCGraw-Hill Book Co., New York, NY, 1965, p. 695.

47. F. A. Shunk: Constitution of Binary Alloys, Second Supplement, MCGraw-Hill Book Co., New York, NY, 1969, p. 575.

48. K. A. Gscheidner, Jr.: Rare Earth Alloys, D. Van Nostrand Co., New York, NY, 1961, p. 245.

49. M. C. Flemings, Solidification Processing, McGraw-Hill, New York, 1974, p. 16.

50. R. C. Ruhl, "Cooling Rates in Splat Cooling," Matl. Sci. Eng., 1967, vol. 1, pp. 313-320.

51. M. F. Gigliotti, G. K. Scarr and G. E. Wasielewski, "High Temperature RST Titanium Alloys, Quarterly Interim Technical Report No. 13," Air Force Contract F33615-83-C-5034, 1 September-30 November, 1986.

52. F. H. Froes and R. G. Rowe, "Rapidly Solidified Titanium," in Rapidly Solidified Alloys and Their Mechanical and Magnetic Properties, B. C. Giessen, D. R. Polk and A. I. Taub, eds., Materials Research Society, Boston, MA, 1986, pp. 309-334.

53. R. G. Rowe and F. H., Froes, "Titanium Rapid Solidification - Alloys and Processes," in Processing of Structural Metals by Rapid Solidification, F. H. Froes and S. J. Savage, eds., ASM International, Metals Park, OH, 1987, in press.

54. L. Eyring, "The Binary Rare Earth Oxides," in Handbook on the Physics and Chemistry of Rare Earths, Vol. III - Non-Metallic Compounds, K. A. Gschneidner, Jr., and L. Eyring, eds., North-Holland, New York, 1979, p. 349.

Table I

Mean Interstitial Content of Feedstock Titanium after Arc Melting

	Oxygen, as O wt ppm(at ppm)	Nitrogen, as N wt ppm(at ppm)	Carbon wt ppm(at ppm)
High-Purity Ti ALTA Corp., dendritic Initial total interstitials: 130 ppm	307 (918)	25 (85)	<133 (<530)
High-Purity Ti Johnson-Matthey, AESAR Group Initial oxygen: 450 ppm	665 (1987)	28 (96)	<167 (<665)
Commercial Purity Ti (Rod Stock, Grade 2)	2267 (6749)	190 (646)	<200 (<793)

Table II

Selected Area Diffraction Pattern Data;
Intercellular and Intergranular Dy_2O_3
in As-Splat-Quenched Ti-11Al-0.5Dy

HKL of plane	Calculated* CUBIC interplanar spacing (nm)	Observed CUBIC interplanar spacing (nm) for zone axis:		
		$[\bar{1}35]$	[100]	$[\bar{1}13]$
(110)	0.7541			0.752
(002)	0.5333		0.535	
$(\bar{2}1\bar{1})$, $(12\bar{1})$	0.4354	0.434		0.432
(022)	0.3771		0.375	
(310)	0.3373	0.338		
$(\bar{1}3\bar{2})$	0.2850	0.284		
(024)	0.2385		0.237	
$(3\bar{3}2)$	0.2274			0.227

HKL of plane	Calculated* MONOCLINIC interplanar spacing (nm)	Observed MONOCLINIC interplanar spacing (nm) for zone axis:
		$[\bar{1}3\bar{2}]$
$(20\bar{1})$	0.5840	0.587
(111)	0.3112	0.311
$(11\bar{2})$	0.2712	0.271
(310)	0.2783	0.279

* cubic lattice parameter: a = 1.0665 nm, Ref. 39
** monoclinic lattice parameters: a = 1.387 nm; b = 0.3518 nm;
c = 0.8589 nm; beta = 100.2 deg.; Ref. 39

Table III

Selected Area Diffraction Pattern Data;
Intercellular and Intergranular Gd_2O_3
in As-Splat-Quenched Ti-11Al-0.5Gd

HKL of plane	Calculated* CUBIC interplanar spacing (nm)	Observed CUBIC interplanar spacing (nm) for zone axis:
		[110]
$(1\bar{1}0)$	0.7646	0.767
(002)	0.5406	0.541
$(\bar{1}12)$	0.4414	0.442
$(\bar{2}22)$	0.3121	0.313
$(\bar{1}14)$	0.2549	0.256

HKL of plane	Calculated** MONOCLINIC interplanar spacing (nm)	Observed MONOCLINIC interplanar spacing (nm) for zone axis:
		$[\bar{1}3\bar{2}]$
$(20\bar{1})$	0.5980	0.601
(111)	0.3183	0.317
$(31\bar{0})$	0.2815	0.285
(112)	0.2805	0.278

* cubic lattice parameter: a = 1.0813 nm, Ref. 39

** monoclinic lattice parameters: a = 1.397 nm; b = 0.356 nm; c = 0.925 nm; beta = 99.1667 deg. Ref. 39

ΔG_f OF OXIDE AND O-Ti SOLUTIONS VS TEMPERATURE

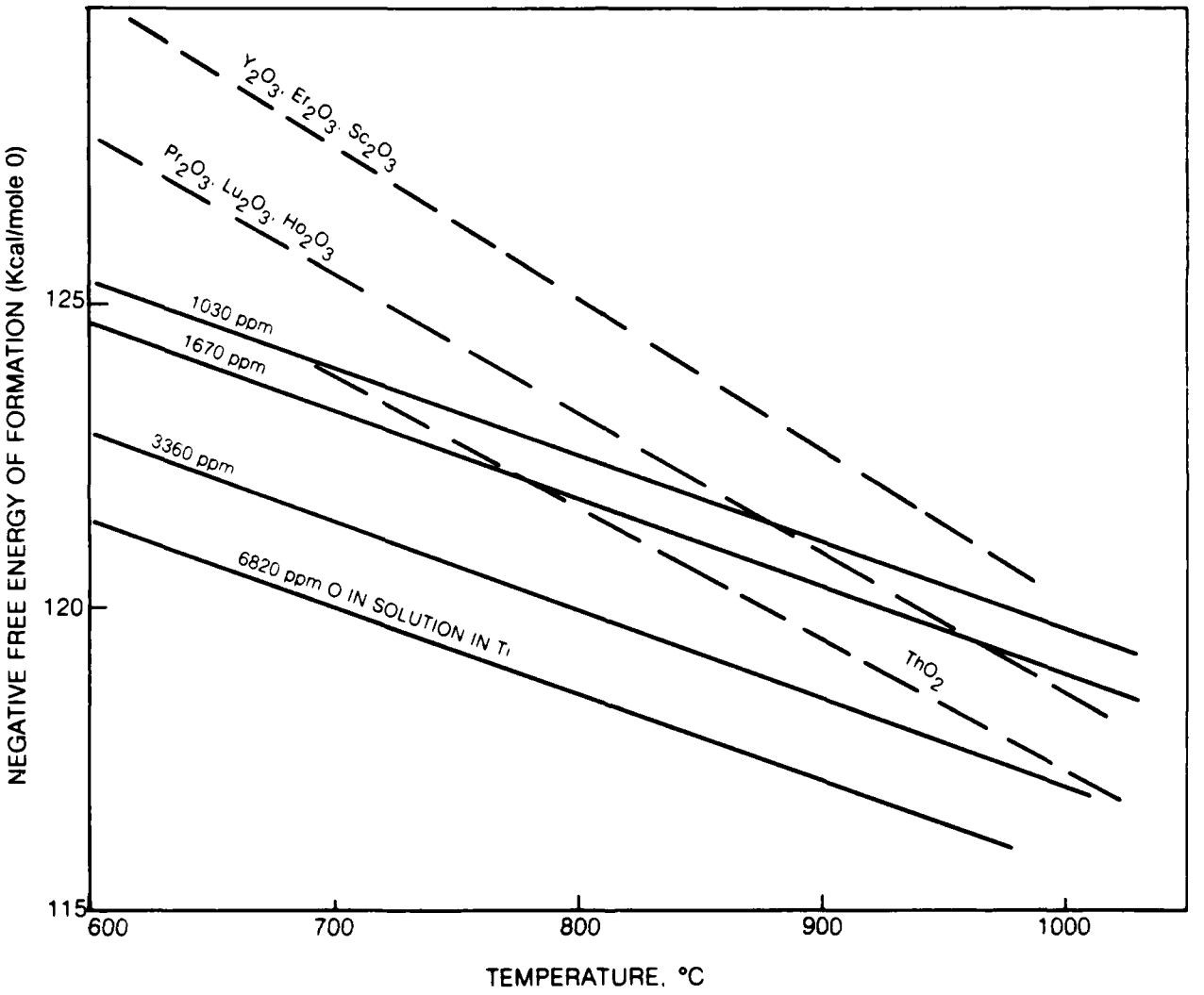

84-4-67-1

FIG. 2

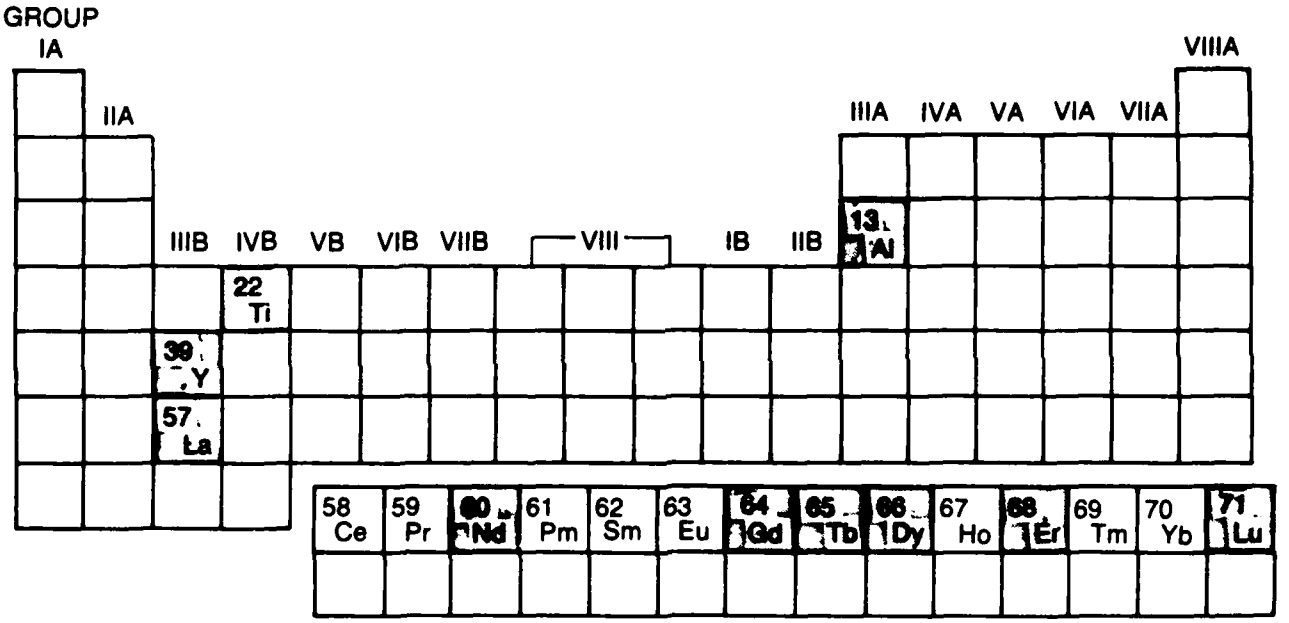
GROUP
IA
IIA
IIIB
IVB
VB
VIB
VIIB
VIII
IB
IIB
IIIA
IVA
VA
VIA
VIIA
VIIIA
13 Al
22 Ti
39 Y
57 La
58 Ce
59 Pr
60 Nd
61 Pm
62 Sm
63 Eu
64 Gd
65 Tb
66 Dy
67 Ho
68 Er
69 Tm
70 Yb
71 Lu

87—4—18—1

UTRC PRECISION HAMMER AND ANVIL SPLAT QUENCHER

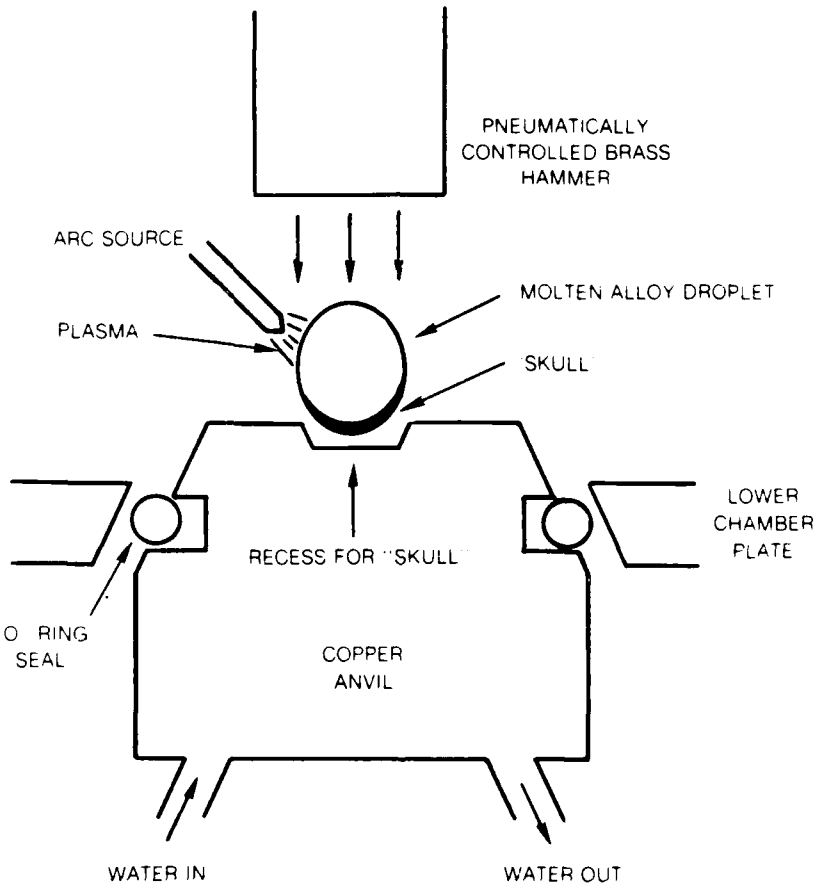

85-10-12-2

TYPICAL BUTTON FROM UTRC CLEAN ATMOSPHERE BUTTON MELTER

TOP VIEW

2 mm

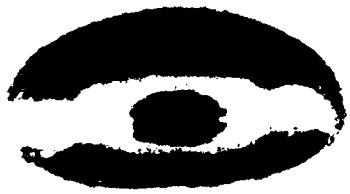

SIDE VIEW

2 mm

85-10-12-8

ARC MELTED & SPLAT QUENCHED SPECIMEN

(NOMINAL ALLOY COMPOSITION Ti-11Al-0.5Y, AT %)

TOP SURFACE

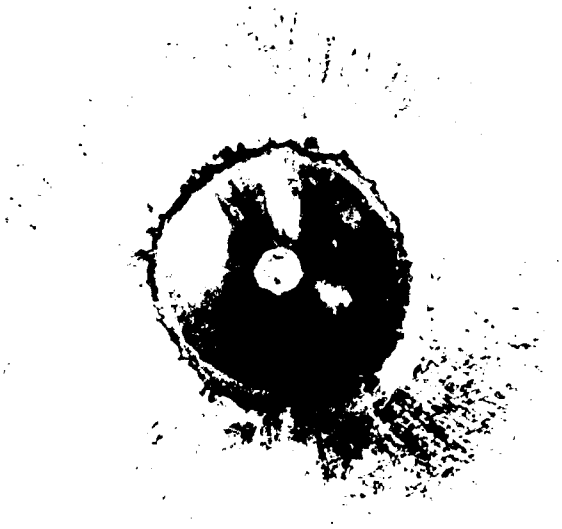

BOTTOM SURFACE

1 cm

87—4—18--2

MICROPROBE ANALYSIS, NOMINAL Ti-11Al-0.5 Gd (AT %)

SPLAT QUENCHED TO 125μm THICKNESS
AGED AT 800°C FOR 0.25 hr
ELECTROLYTICALLY THINNED FOR (S) TEM

BACKSCATTERED ELECTRON IMAGE

MICROPROBE ANALYSIS.
THREE 12 × 12μm AREAS.
(Gd_2O_3 STANDARD USED FOR Gd)

ALUMINUM: 10.2 ± 0.3 AT %
GADOLINIUM: 0.42 ± 0.06 AT %

FIG. 7

HCP MARTENSITE & INTERCELLULAR Er_2O_3 DISTRIBUTION IN AS-SPLAT-QUENCHED Ti-11Al-0.5Er (AT %)

BRIGHT FIELD CTEM, 165μm THICK SPLAT, AREA OF FIG. 10

87-4-18-4

NON-MARTENSITIC ALPHA (HCP) GRAIN IN AS-SPLAT-QUENCHED Ti-11Al-0.5Er (AT %)

165μm THICK SPLAT

BRIGHT FIELD CTEM

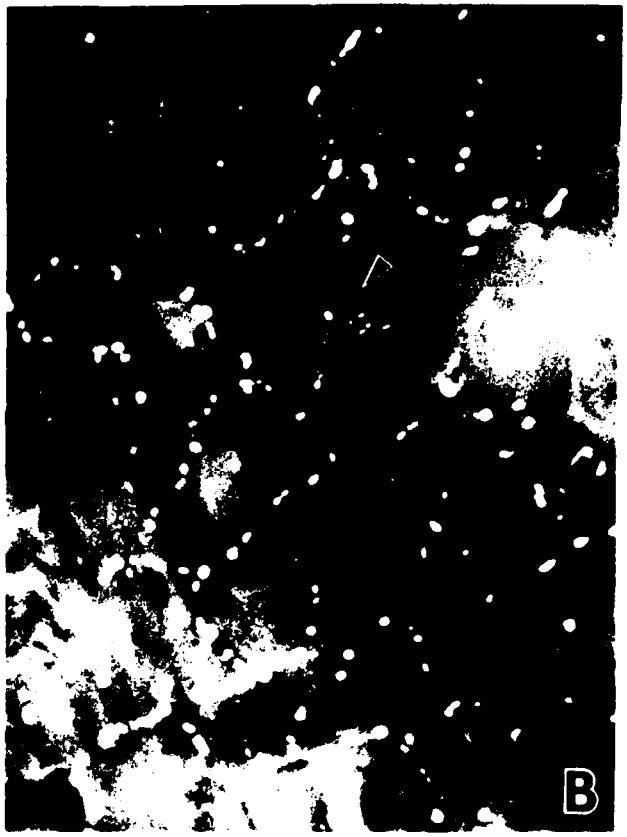

INTERCELLULAR ERBIA DISTRIBUTION IN UPPER AREA OF (A). ANNULAR DARK FIELD STEM; 120 kV, 2 nm SPOT SIZE. TILTED 30° WITH RESPECT TO (A).

FIG. 8

FIG. 9

DISTRIBUTION OF Dy_2O_3 IN AS-SPLAT-QUENCHED Ti-11Al-0.5Dy (AT%)

150μm SPLAT THICKNESS, ANNULAR DARK FIELD STEM IMAGE, 120 kV

85 12 44 2

Er_2O_3 DISTRIBUTION IN AS-SPLAT-QUENCHED Ti-11Al-0.5Er (AT %)

ANNULAR DARK FIELD STEM IMAGE, 165μm THICK SPLAT. (AREA OF FIG. 7)

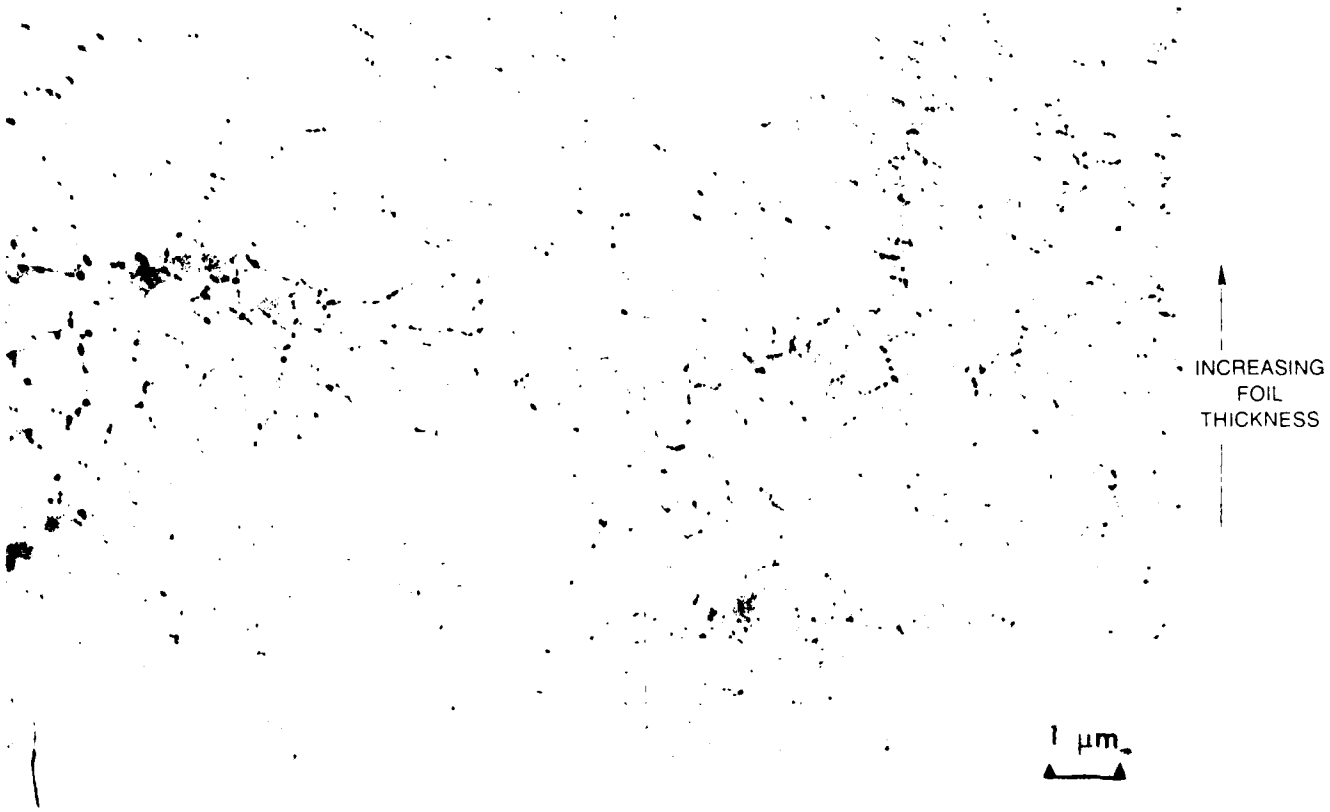

85-10-43-2

Dy_2O_3 DISTRIBUTION IN AS-SPLAT-QUENCHED Ti-11Al-0.5 Dy (AT %)

ANNULAR DARK FIELD STEREO IMAGE, 120 kV
AREA FROM CENTER OF FIG. 9

85 12-44-3

Dy_2O_3 DISTRIBUTION IN AS-SPLAT-QUENCHED Ti-11Al-0.6Dy (AT %)

AREA SHOWN IN FIG. II-11

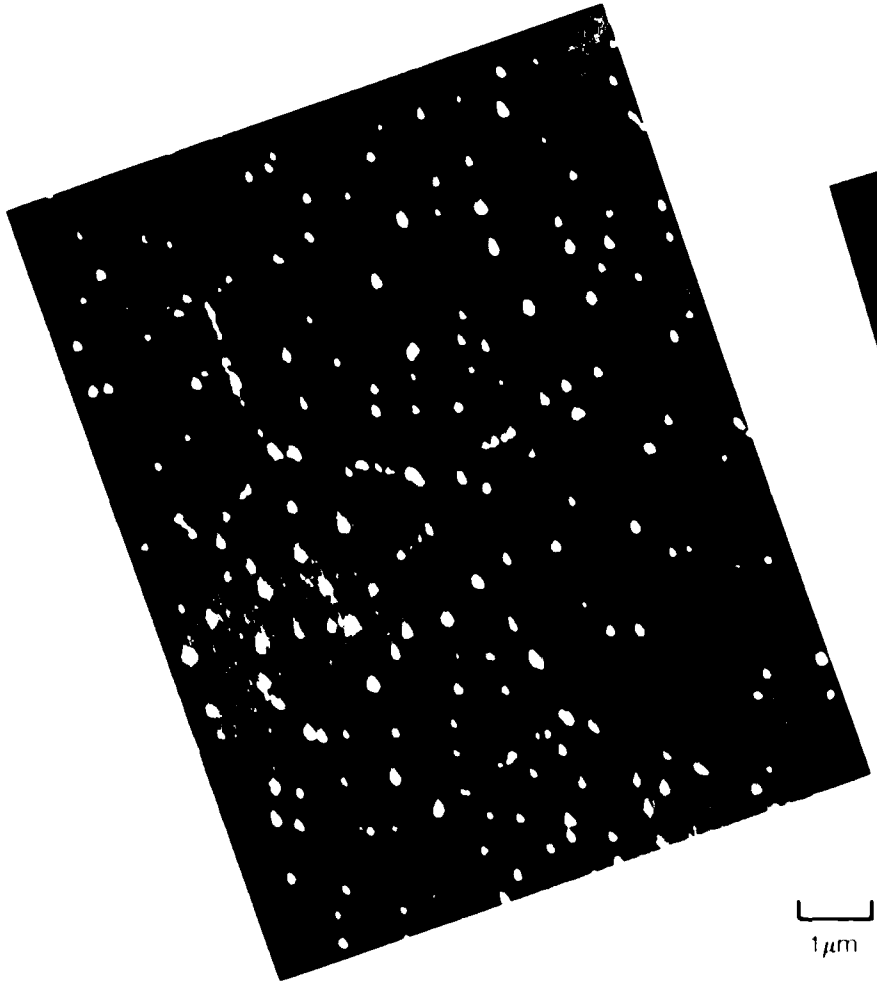

(A) BACKSCATTERED ELECTRON IMAGE, 120 kV
ALL Dy_2O_3 PRECIPITATES OF >50 nm
WITHIN THE THIN FOIL ARE IN CONTRAST

(B) SECONDARY ELECTRON IMAGE, 120 kV.
ONLY Dy_2O_3 AT OR NEAR THIN FOIL
SURFACE IN CONTRAST. AREA FRACTION
≅ VOLUME FRACTION

R87-917553-2

FIG. 12

85 12 44 4

FIG. 13

MICROSTRUCTURE OF AS-SPLAT-QUENCHED Ti-11Al-0.5 Gd (AT %)

64μm SPLAT THICKNESS. AREA "a" ALSO SHOWN IN FIGURE 14

FIG. 14

Gd_2O_3 DISTRIBUTION IN AS-SPLAT-QUENCHED Ti-11Al-0.5 Gd (AT %)

64μm SPLAT THICKNESS; AREA "a" ALSO MARKED IN FIGURE 13

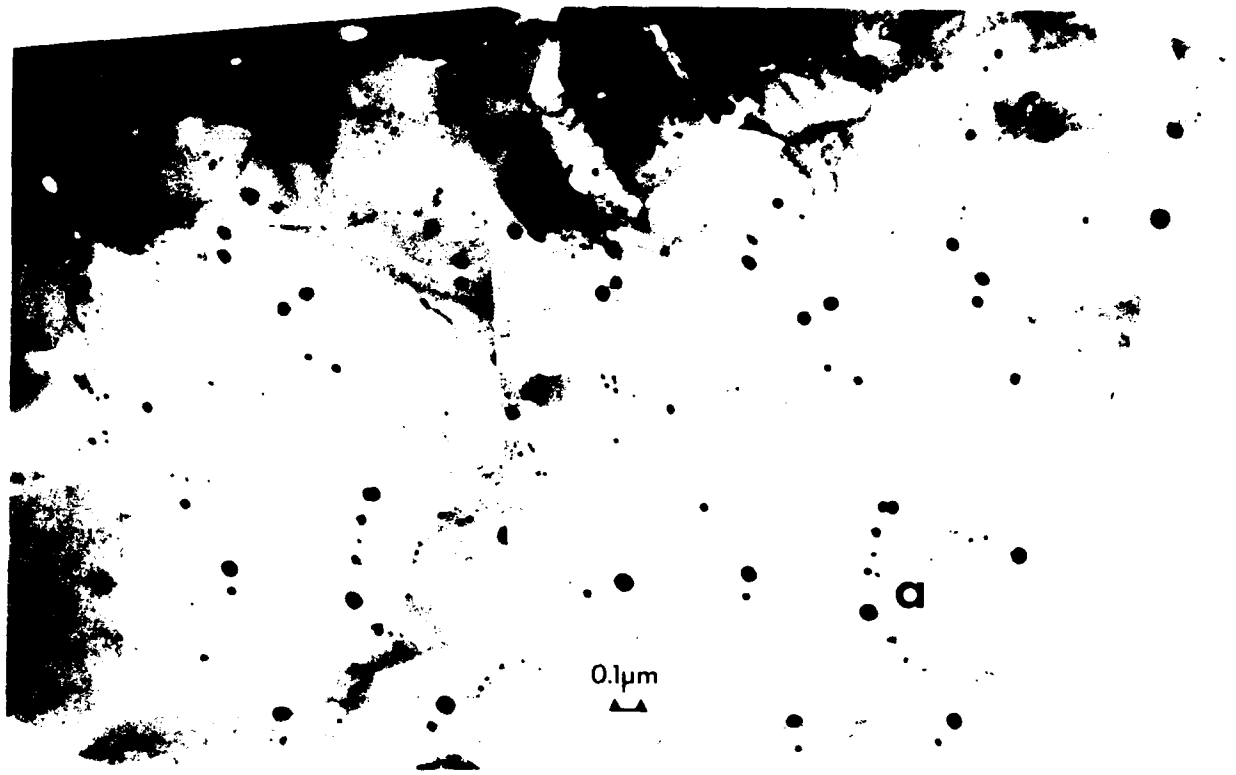

(A) BRIGHT FIELD STEM STEREO PAIR; 120 kV, 5 nm SPOT SIZE

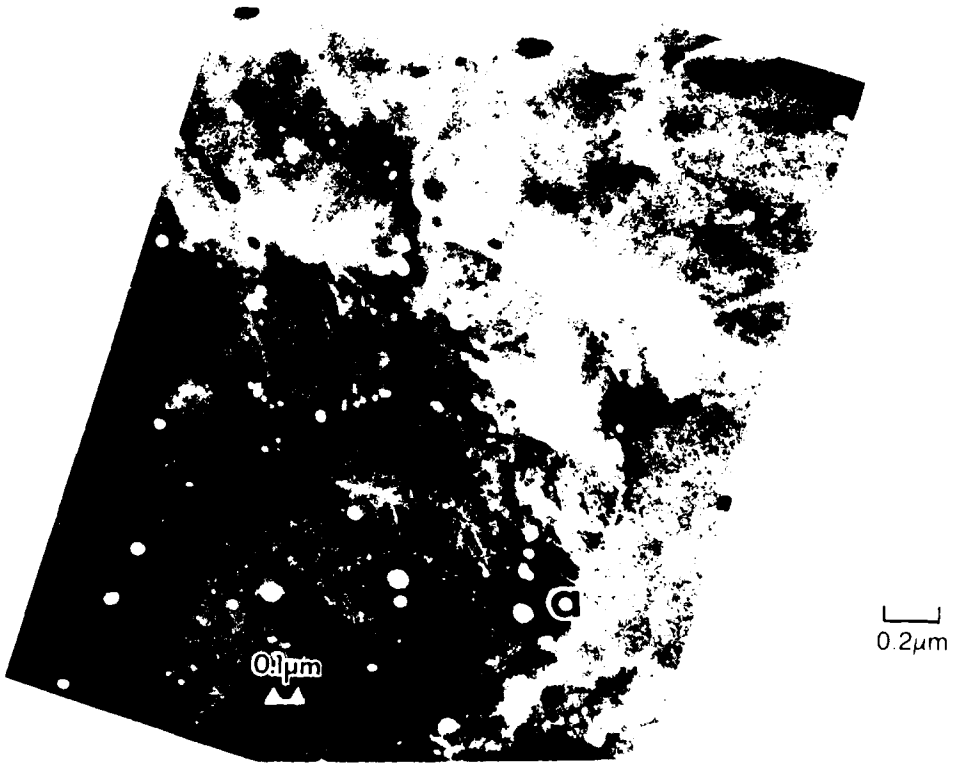

(B) ANNULAR DARK FIELD STEM, AREA OF (A)

FIG. 15

Gd_2O_3 DISTRIBUTION IN AS-SPLAT-QUENCHED Ti-11Al-0.5 Gd (AT %)

AREA "a" ALSO MARKED IN FIGURES 13 AND 14

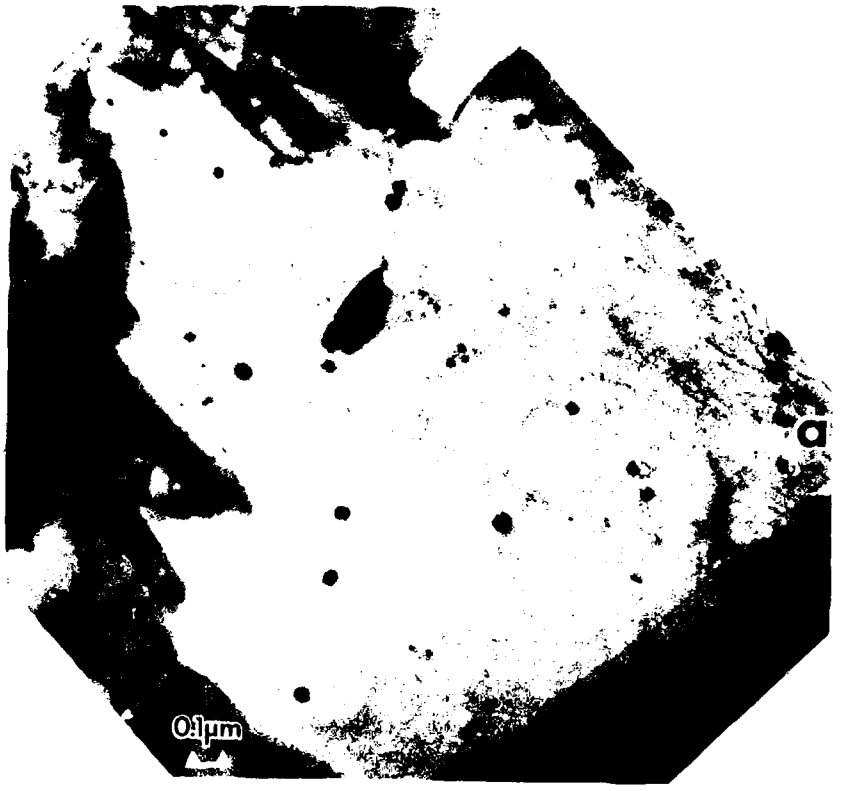

(A) DARK FIELD CTEM. AREA IN FIGURES 13 AND 14.
g = 222, Gd_2O_3, SHOWN BY POINTER IN (B)

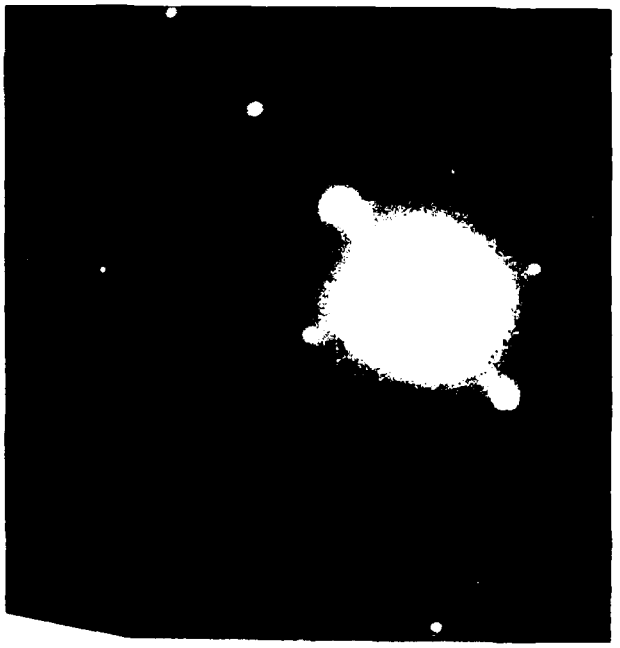

(B) SELECTED AREA DIFFRACTION PATTERN FROM CENTER OF (A).
BEAM DIRECTION APPROXIMATELY 5° FROM [1$\bar{1}$00] MATRIX.

87-4-18-8

R87-917553-2

ANNULAR D.F. STEM IMAGE AND ENERGY DISPERSIVE X-RAY SPECTRUM, Dy_2O_3 IN AS-SPLAT-QUENCHED Ti-11Al-0.5 Dy (AT %)

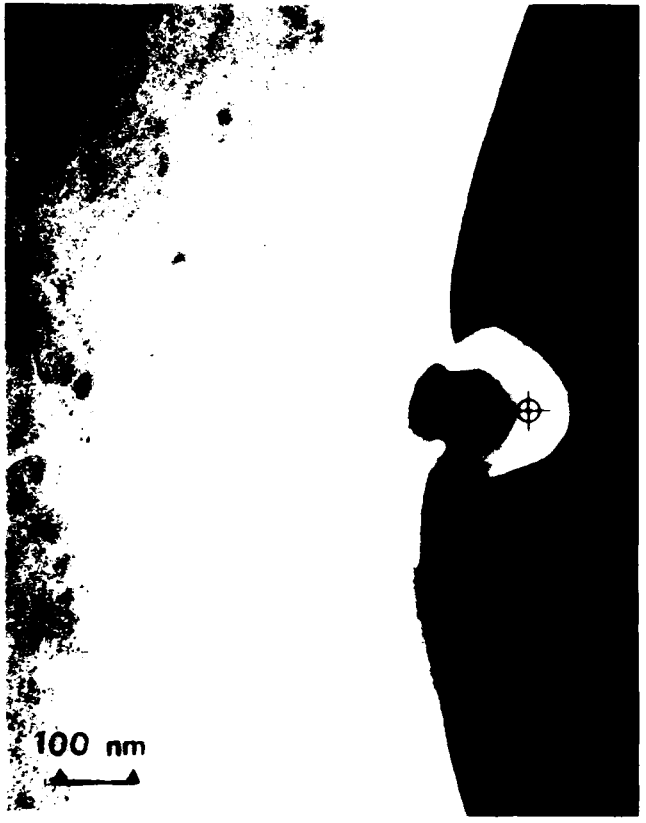

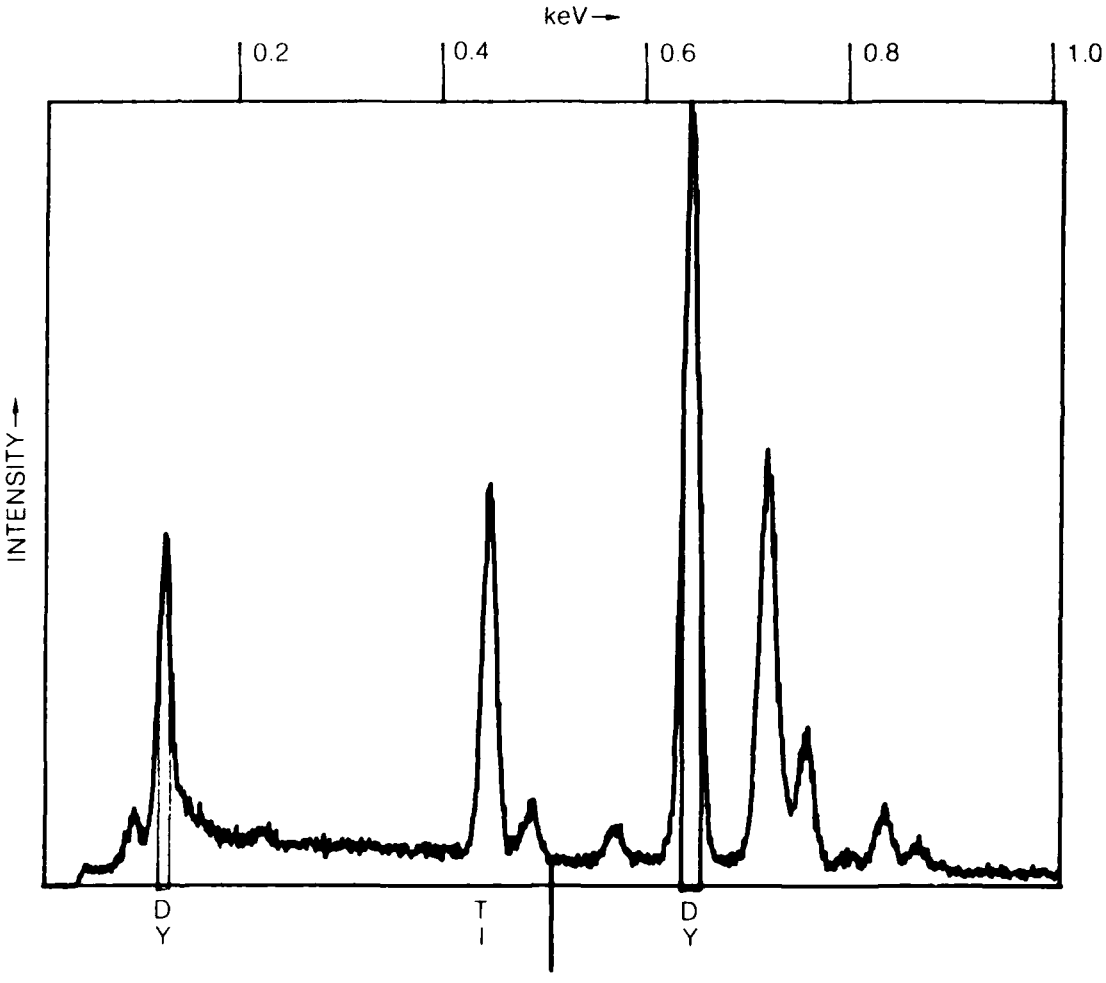

120 kV, 5 nm SPOT SIZE, 180 s LIVE COUNT TIME, BEAM POSITIONED AS SHOWN AT LEFT

85-12-44-5

FIG. 16

CUBIC INTERGRANULAR Dy_2O_3 IN AS-SPLAT-QUENCHED Ti-11 Al-0.5 Dy (at%)

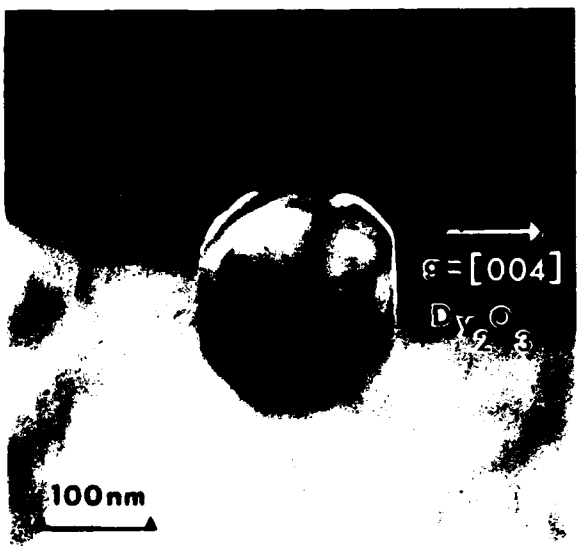

DARK FIELD CTEM IMAGE

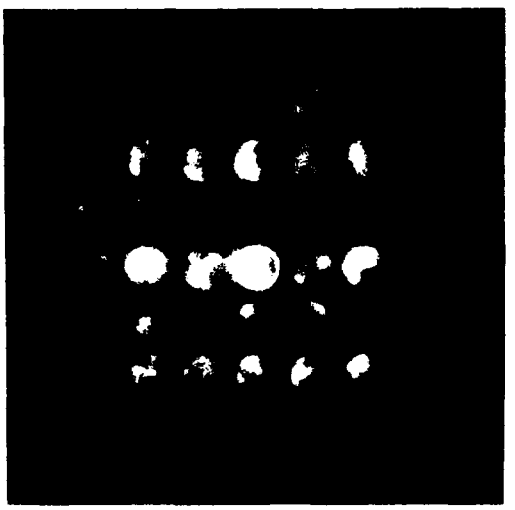

[100] CONVERGENT BEAM MICRODIFFRACTION PATTERN FROM DYSPROSIA PRECIPITATE, 40 nm SPOT SIZE

MONOCLINIC INTERCELLULAR Dy_2O_3 IN AS-SPLAT-QUENCHED Ti-11 Al-0.5 Dy (at%)

DARK FIELD CTEM IMAGE, g = 402

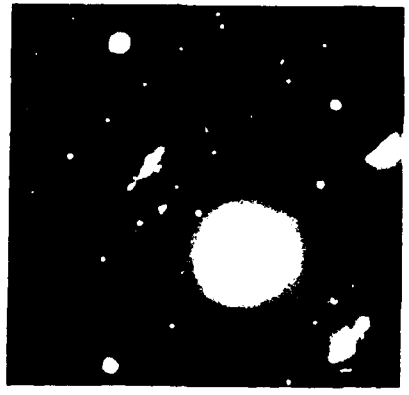

SADP; MONOCLINIC ZONE AXIS: $[\bar{1}3\bar{2}]$
POINTER MARKS g OF DARK FIELD IMAGE

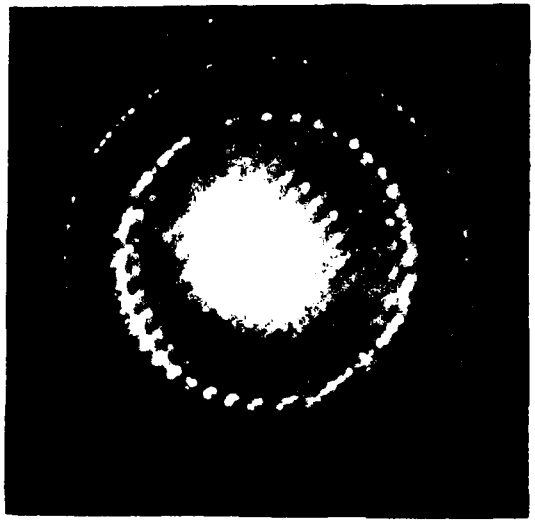

LOW CAMERA CONSTANT CBDP,
40 nm SPOT SIZE

CBDP; MONOCLINIC INTERCELLULAR Dy_2O_3 IN AS-SPLAT-QUENCHED Ti-11 Al-0.5 Dy (at%)

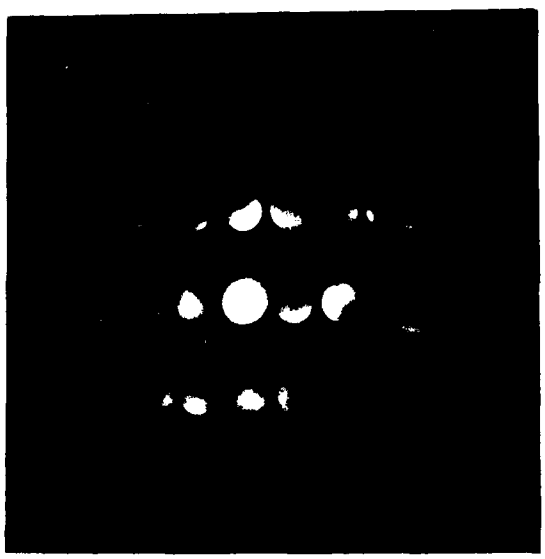

CBDP, 40 nm SPOT SIZE

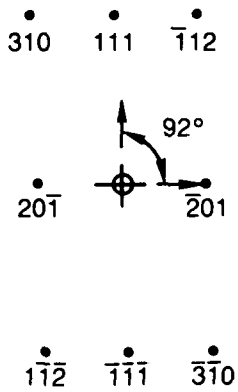

$[\bar{1}3\bar{2}]$ ZONE AXIS
MONOCLINIC STRUCTURE

FIG. 20

GRAIN STRUCTURE AND Er_2O_3 DISTRIBUTION IN Ti-11 Al-0.5 Er (at%)

100μm THICK SPLAT: AGED AT 800°C/0.25 hr

FIG. 21

GRAIN STRUCTURE AND Er_2O_3 DISTRIBUTION IN Ti-11 Al-0.5 Er (at%)

100μm THICK SPLAT; AGED AT 800°C/0.25 hr

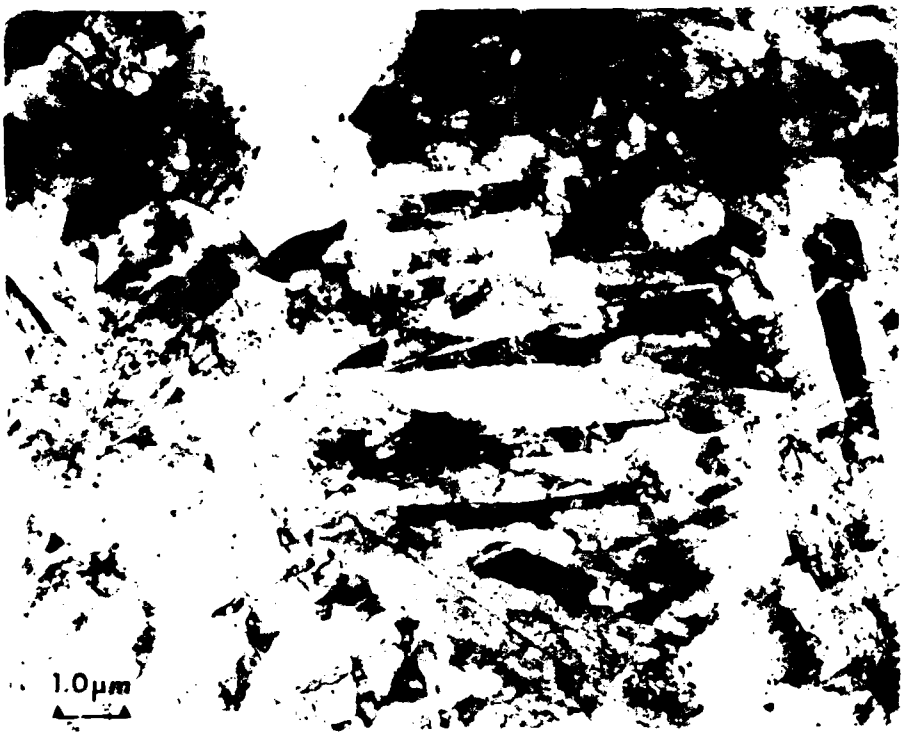

(a) BRIGHT FIELD CTEM

(b) ANNULAR DARK FIELD STEM

87 4 18 13

INTERCELLULAR Er_2O_3 PRECIPITATE IN Ti-11 Al-0.5 Er (at%)

100μm THICK SPLAT; AGED AT 800°C/0.25 hr

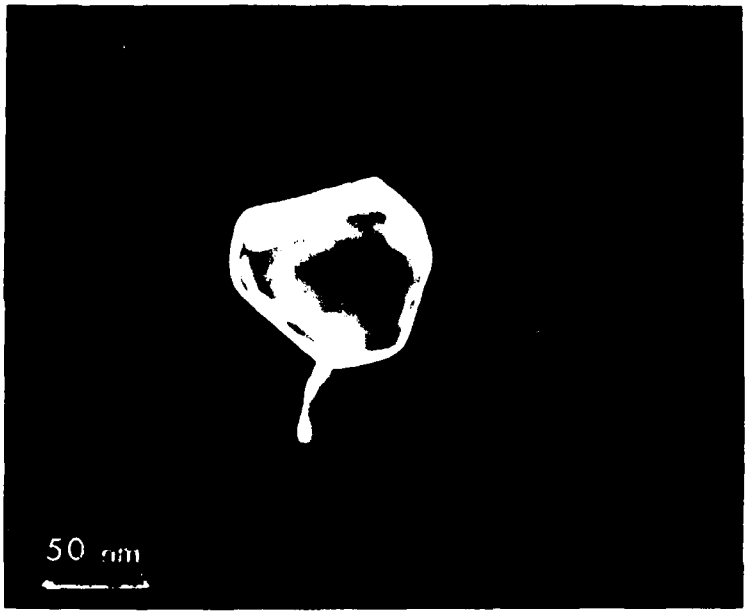

(a) INTERCELLULAR, EQUILIBRIUM-STRUCTURE Er_2O_3 PRECIPITATE DARK FIELD CTEM, $g = 4\bar{4}0$

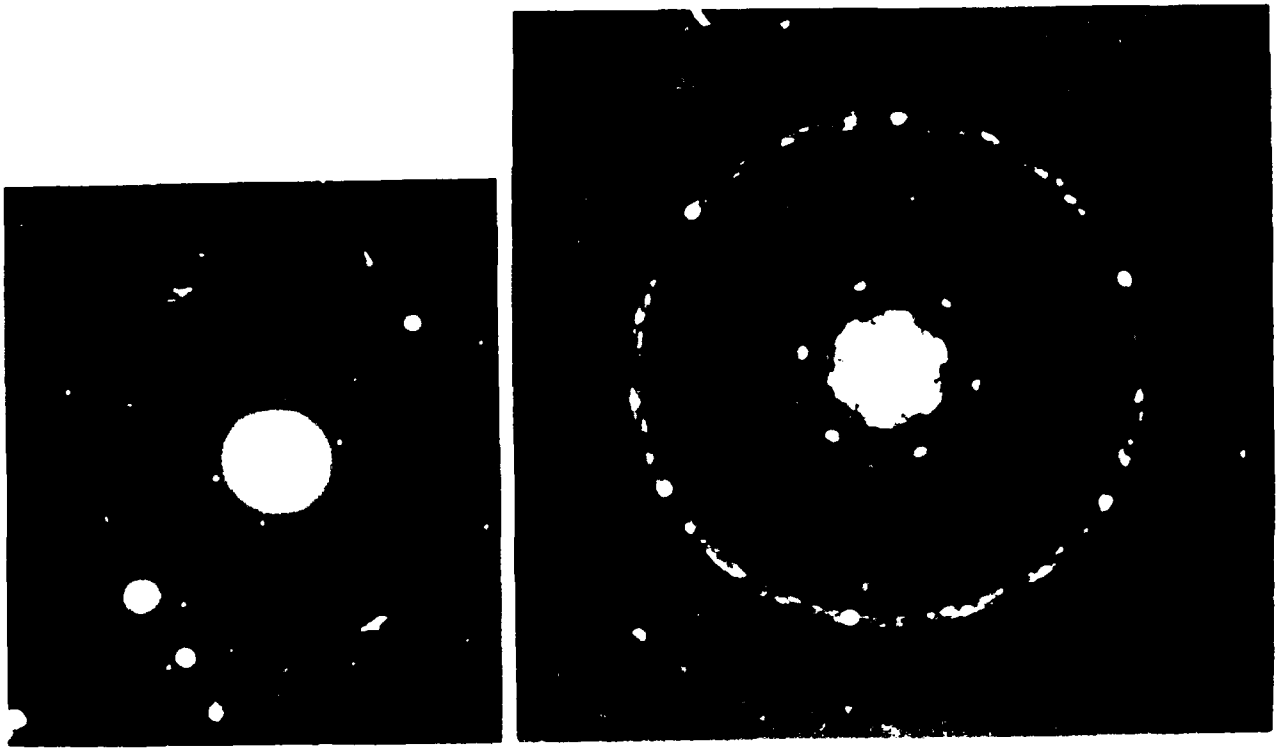

(b) [111] ZONE AXIS SELECTED AREA AND CONVERGENT BEAM DIFFRACTION PATTERNS FROM PRECIPITATE IN (a)

FIG. 23

ERBIA DISTRIBUTION IN Ti-11 Al-0.5 Er (at%)

100μm THICK SPLAT: AGED AT 800°C/0 25 hr

FIG. 24

ERBIA DISTRIBUTION IN Ti-11 Al-0.5 Er (at%)

100μm THICK SPLAT, AGED AT 200°C/0 25 hr
AREA SHOWN IN FIG. 23

1μm

(b) ANNULAR DARK FIELD STEM

(a) BRIGHT FIELD STEM

FIG. 25

ERBIA DISTRIBUTION IN Ti-11 Al-0.5 Er (at%)

175μm THICK SPLAT: AGED AT 800°C/4 hr

ERBIA DISTRIBUTION IN Ti-11 Al-0.5 Er (at%)

175μm THICK SPLAT, AGED AT 800°C/4 hr
BEAM DIRECTION NEAR [1$\bar{1}$00]; AREA IN LEFT ON FIG 25

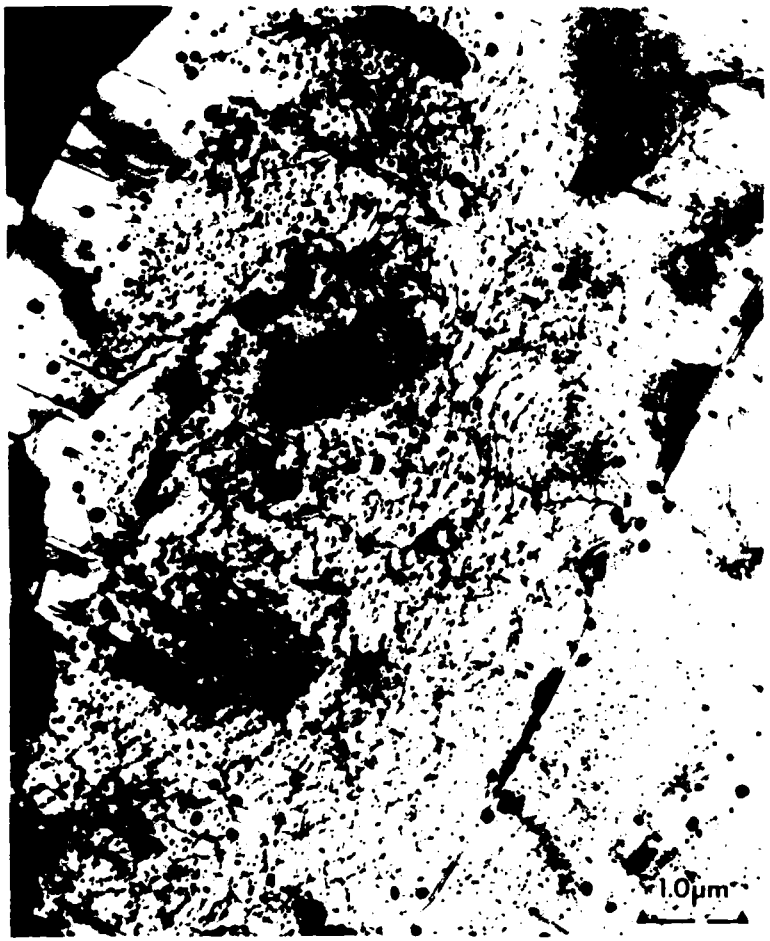

(a)

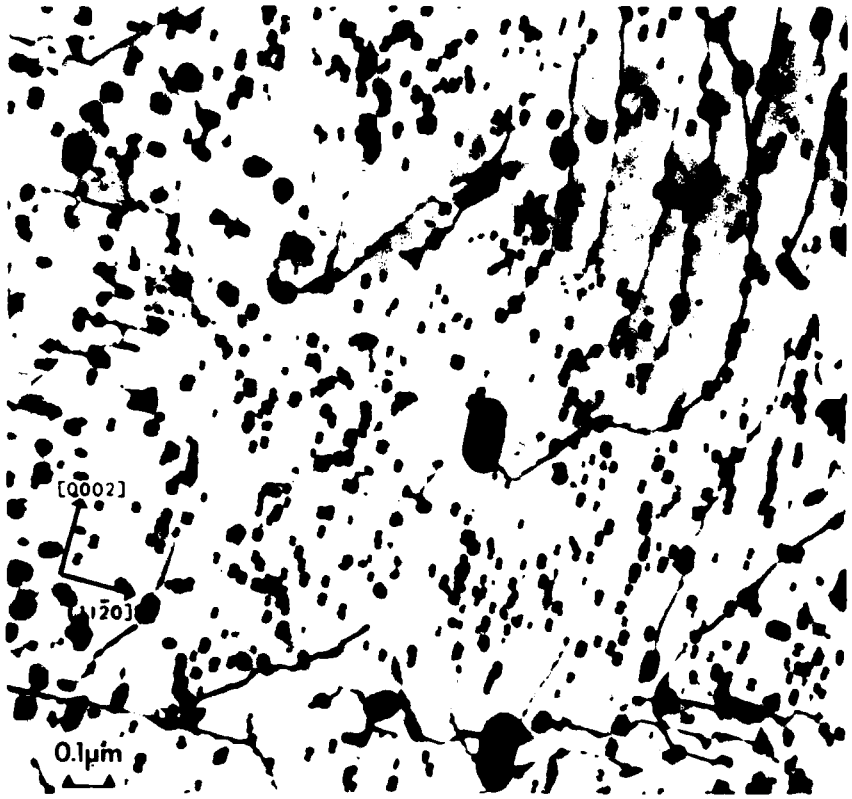

(b) AREA IN CENTER OF (a). MULTI-BEAM, BUT g = 0002 DOMINANT. MATRIX STRAIN CONTRAST IS EVIDENT AT SMALL TYPE I ERBIA PRECIPITATES.

ERBIA DISTRIBUTION IN Ti-11 Al-0.5 Er (at%)

175μm THICK SPLAT; AGED AT 800°C/4 hr

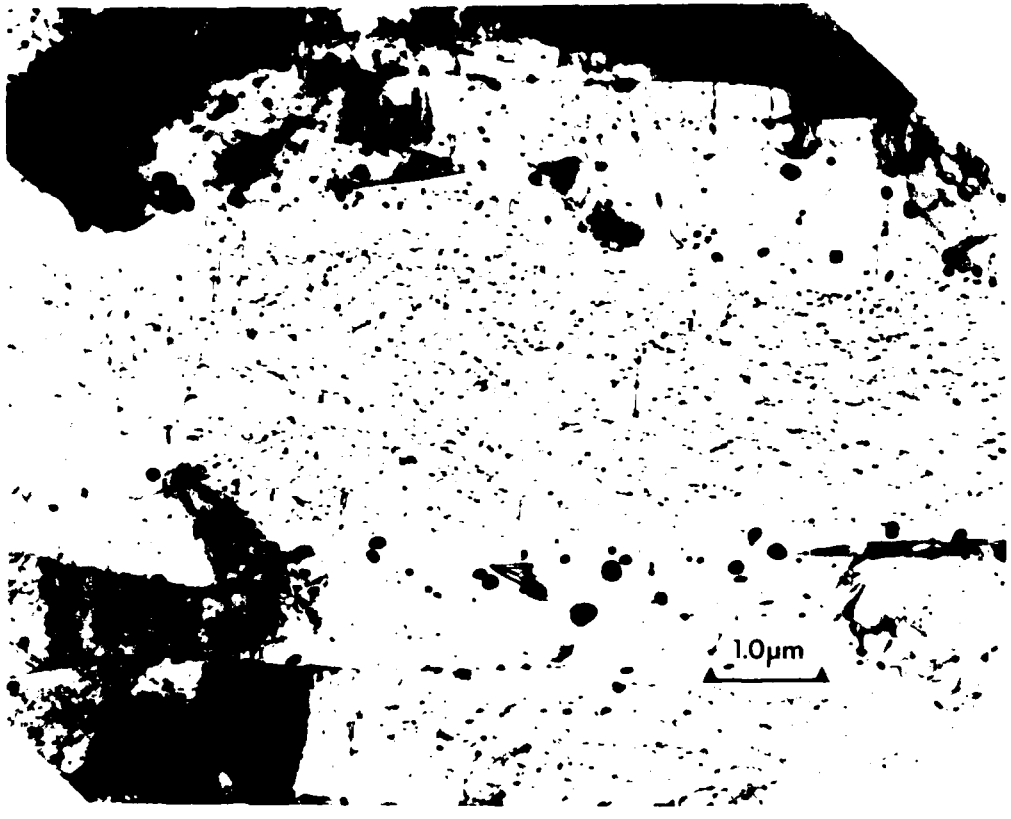

TWO BEAM BRIGHT FIELD TEM, g = 0002

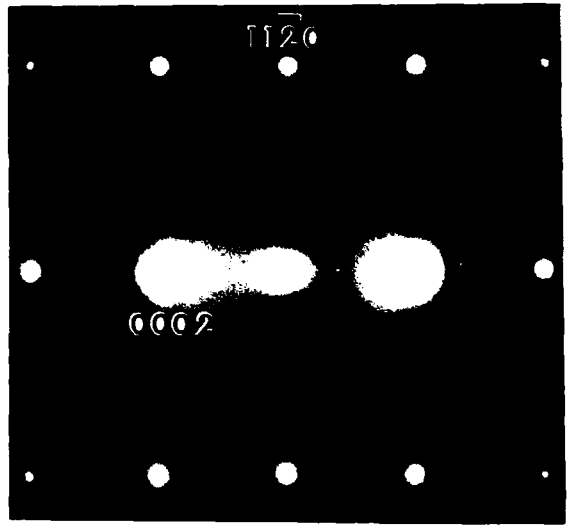

ASSOCIATED [1100] SADP
FROM CENTRAL GRAIN

ERBIA DISTRIBUTION IN Ti-11 Al-0.5 Er (at%)

175μm THICK SPLAT; AGED AT 800°C/4 hr

(a) BRIGHT FIELD STEREO PAIR, g = 0002

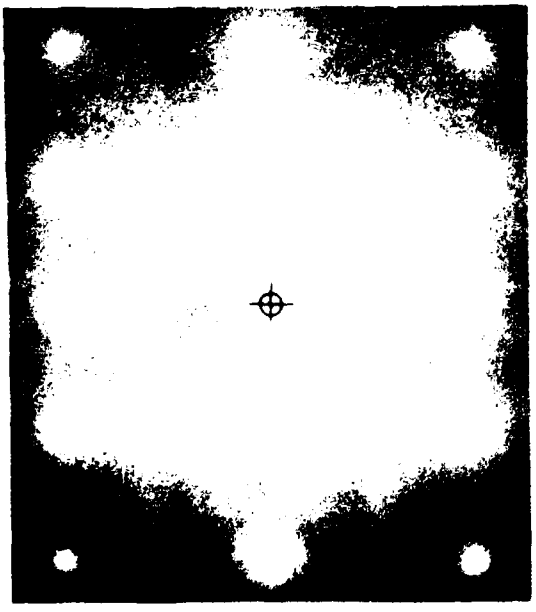

[1$\bar{1}$00] SADP FROM CENTER OF (a). FOIL TILTED TO MIDPOINT OF STEREO ROTATION

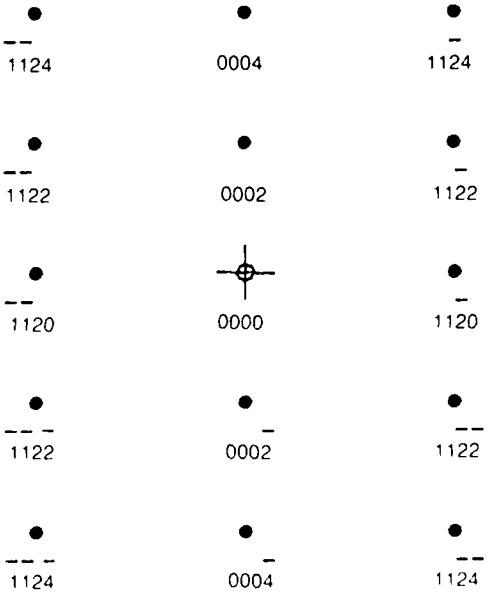

MATRIX SPOT INDICES

FIG. 29

ERBIA DISTRIBUTION IN Ti-11 Al-0.5 Er (at%)

175μm THICK SPLAT; AGED AT 800°C/4 hr; AREA IN FIGS. 27, 28
TWO BRIGHT BEAM FIELD, g = 0002 STRAIN CONTRAST FROM TYPE I ERBIA
(0001) MATRIX II (111) ERBIA

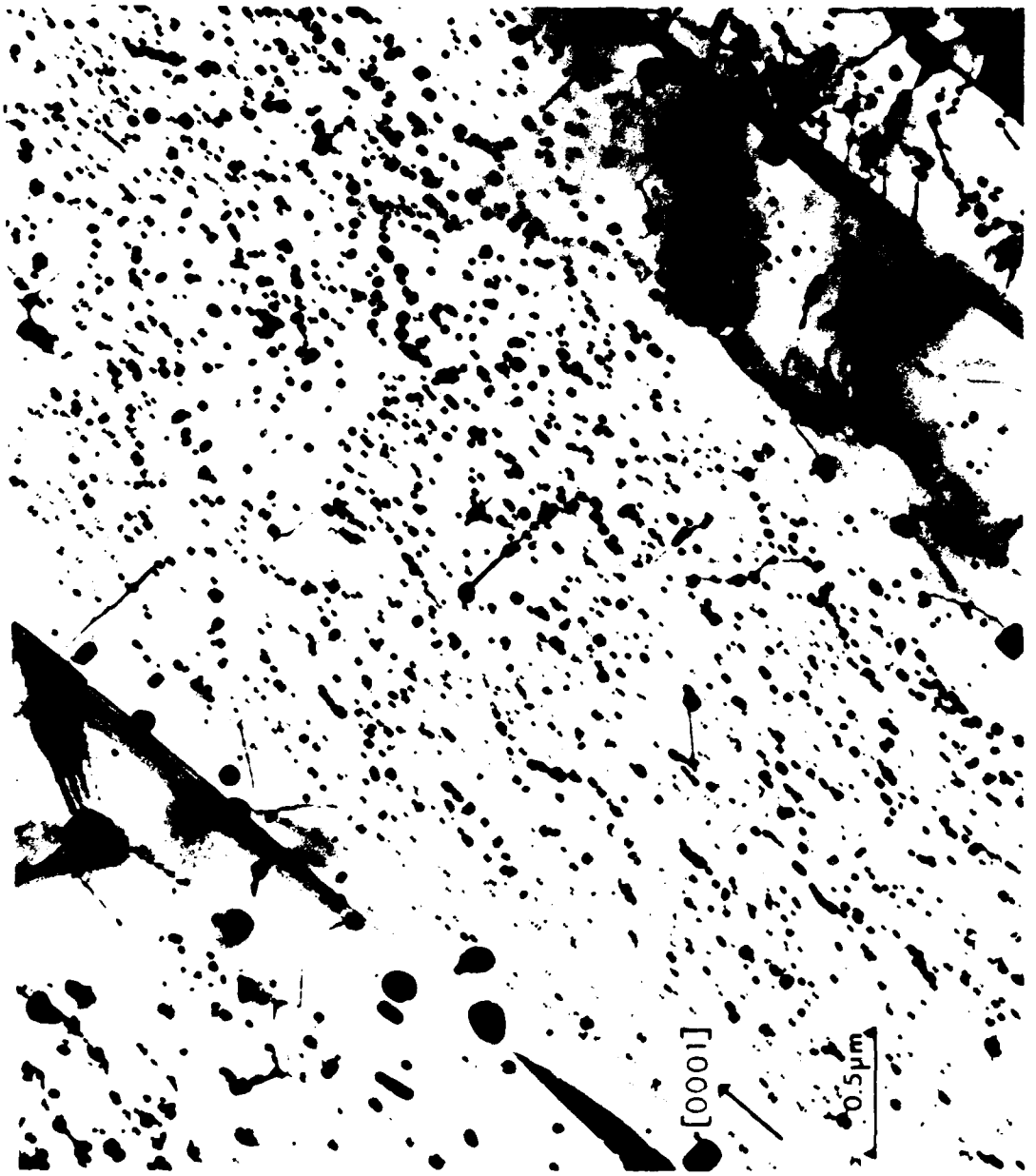

87 - 4 - 18 - 22

FIG. 30

ERBIA DISTRIBUTION IN Ti-11 Al-0.5 Er (at%)

175μm THICK SPLAT; AGED AT 800°C/4 hr; AREA OF FIG. 29
TWO BEAM BRIGHT FIELD, $g = 11\bar{2}0$ STRAIN CONTRAST FROM TYPE II ERBIA
$(11\bar{2}0)$ MATRIX (111) ERBIA

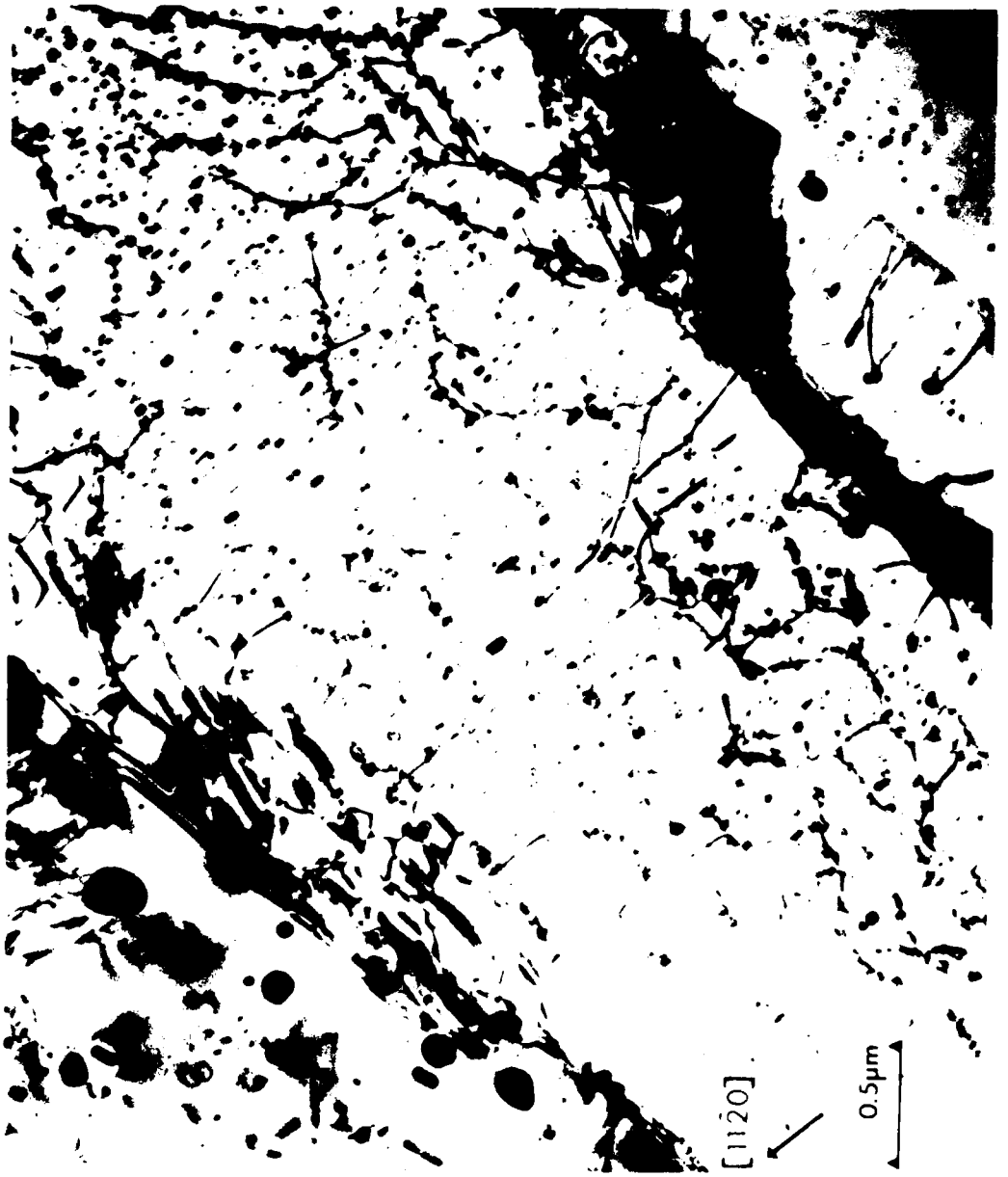

87 - 4 - 18 - 23

Er_2O_3 DISTRIBUTION IN Ti-11 Al-0.5 Er (at%)

125μm THICK SPLAT; AGED AT 800°C/0.25 hr

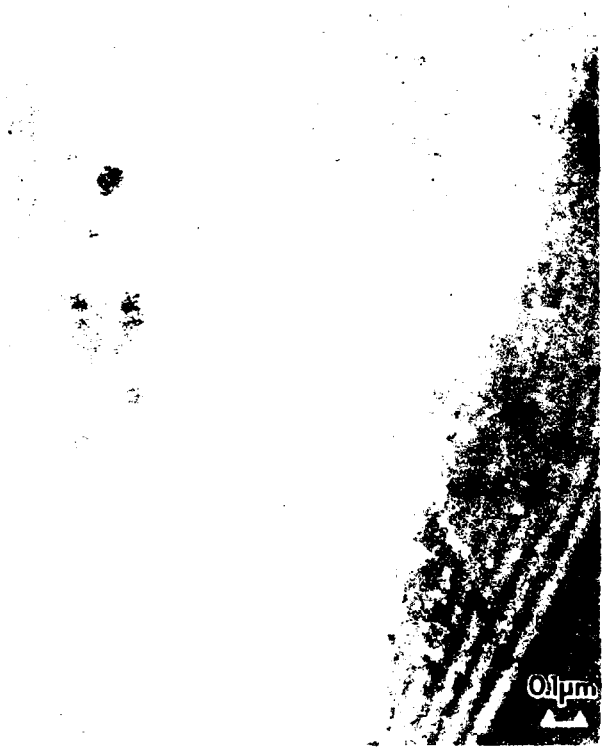

DARK FIELD, g = 222, Er_2O_3

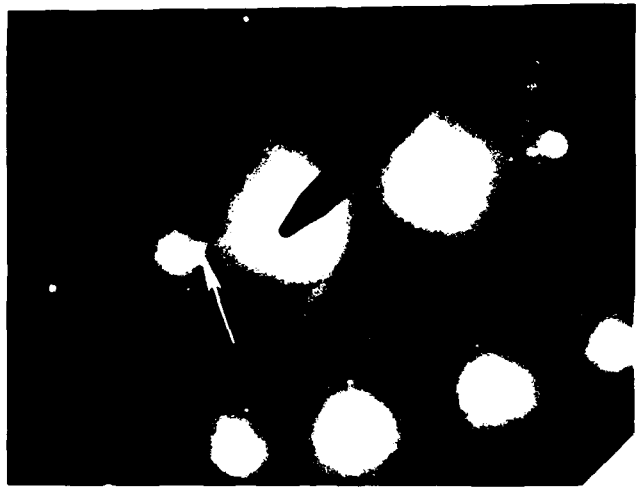

SADP FROM AREA ABOVE; [$1\bar{1}00$] ZONE AXIS
BEAM STOP OVER 0000; ARROW MARKS 222 Er_2O_3

HCP matrix, Ti-11at%Al

Type I Erbium Oxide

Type II Erbium Oxide, Er_2O_3

Lattice Parameter(s): a = 2.925 Å

a = 10.12 Å

a = 10.55 Å

HEXAGONAL Zone Axis = $1\bar{1}00$

CUBIC Zone Axis = $11\bar{2}$

CUBIC Zone Axis = $11\bar{2}$

c = 4.675 Å

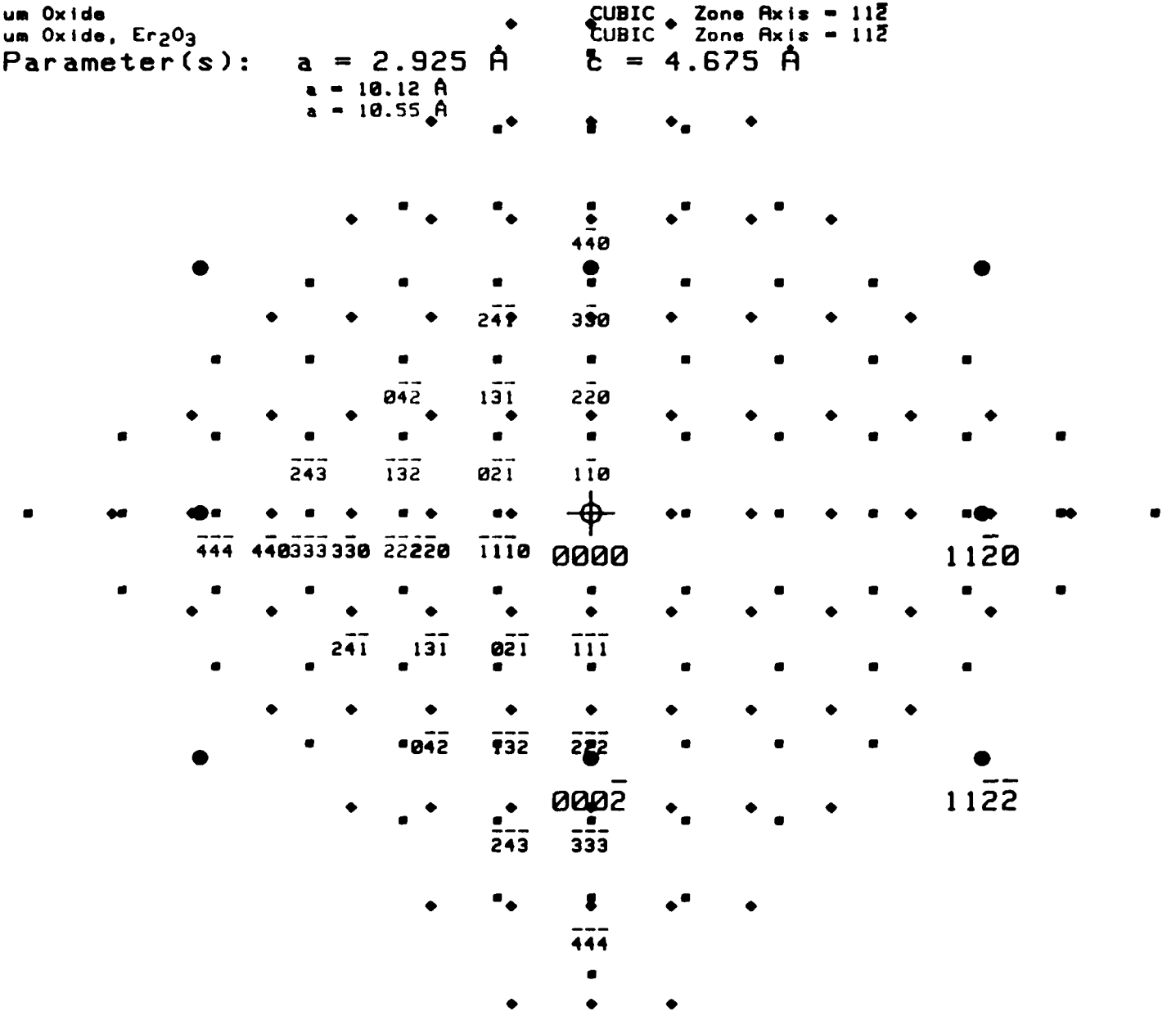

R87-917553-2

FIG. 32

87-4-18-39

FIG. 33

SADP, <110> ZONE AXIS, TYPE I ERBIA PRECIPITATES

CENTER OF AREA SHOWN IN FIG. 34

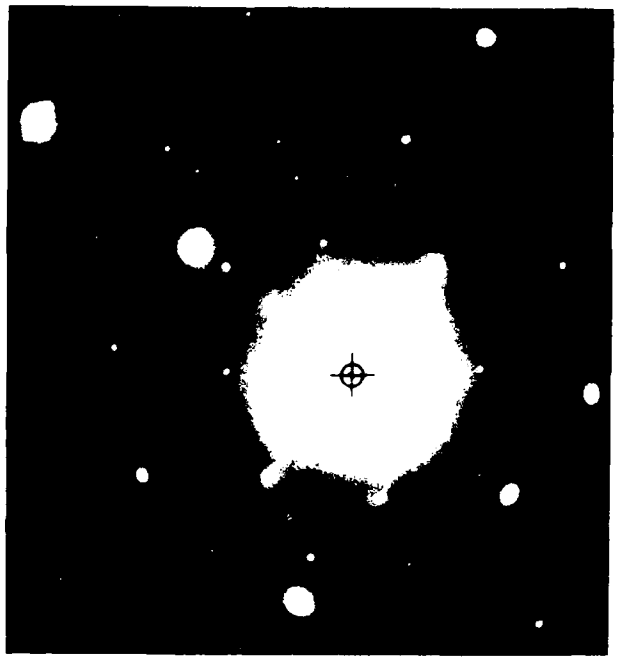

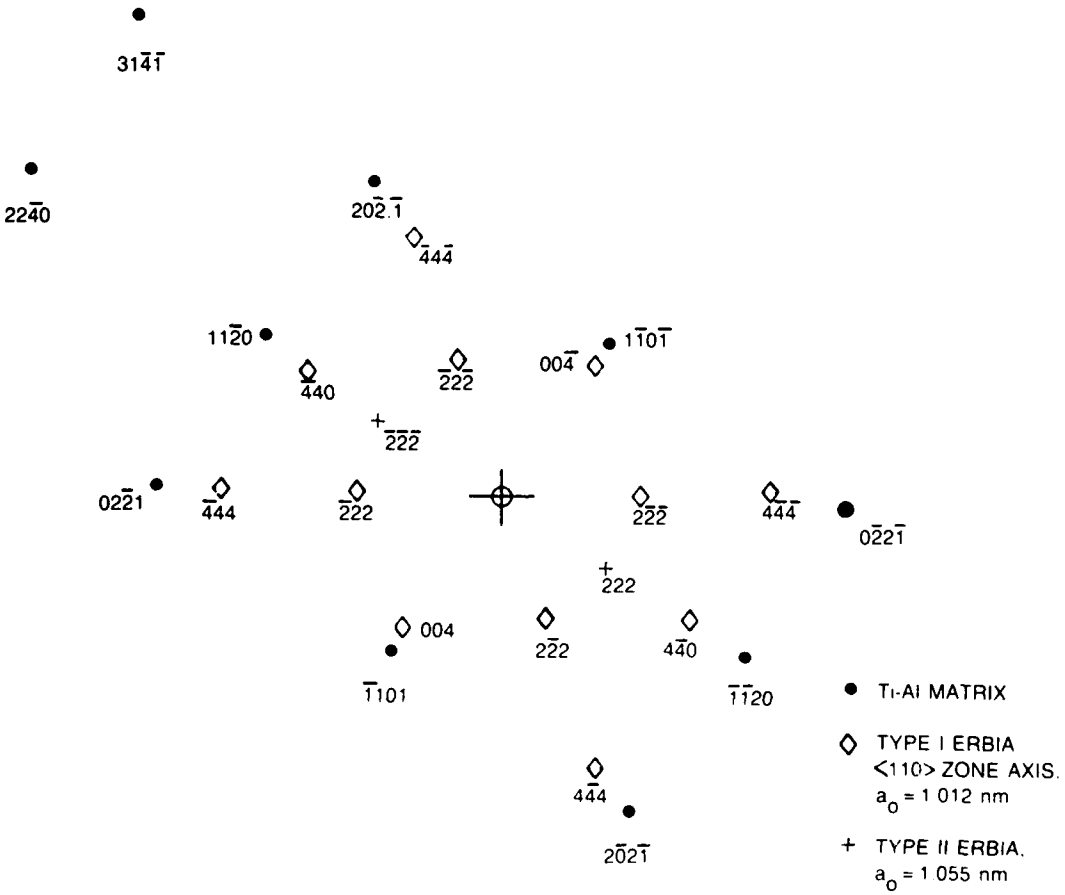

87 - 4 18 - 25

R87-917553-2

ERBIA PRECIPITATES IN Ti-11 Al-0.5 Er (at%)

160μm THICK SPLAT; AGED AT 800°C/0.25 hr

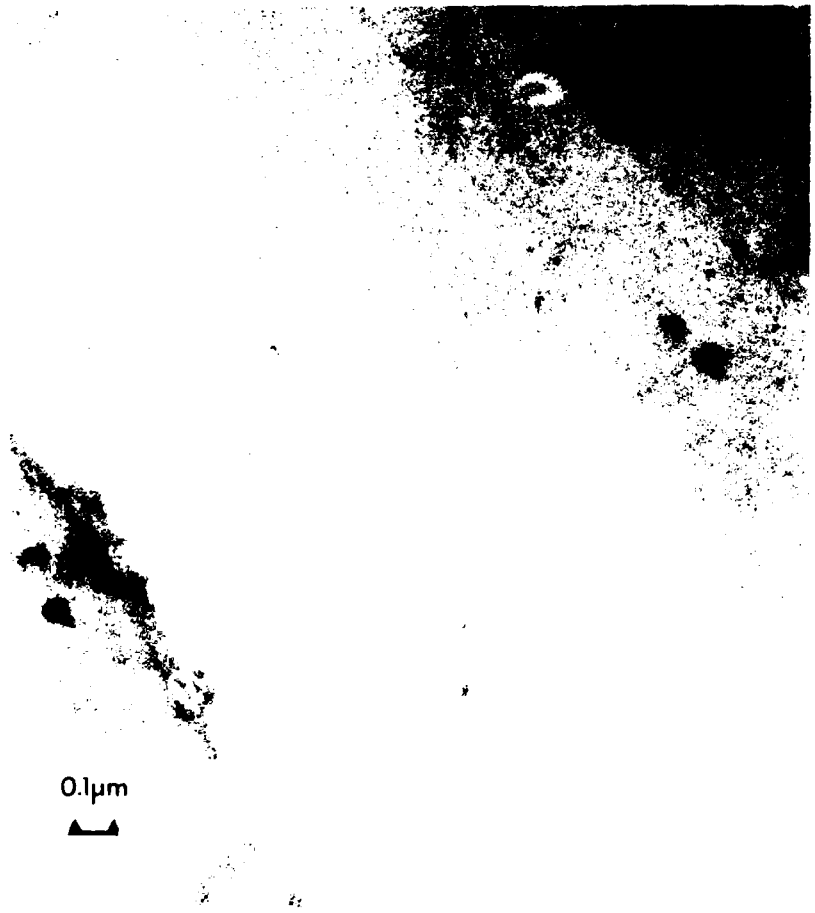

DARK FIELD TEM; g = $\bar{4}40$, TYPE I ERBIA

DARK FIELD TEM; g = 222, TYPE II ERBIA

87-4-18-24

FIG. 34

FIG. 35

ERBIA DISTRIBUTION IN Ti-11 Al-0.5 Er (at%)

175μm THICK SPLAT; AGED AT 800°C/4 hr; AREA OF FIG. 30
DARK FIELD CTEM, g = 440 TYPE I ERBIA MARKED BY POINTER

FIG. 36

ERBIA DISTRIBUTION IN Ti-11 Al-0.5 Er (at%)

175μm THICK SPLAT; AGED AT 800°C/4 hr; AREA OF FIGS. 30, 35
DARK FIELD CTEM, g = 222 OF TYPE II ERBIA MARKED BY POINTER

87-4-18-38

FIG. 37

GRAIN STRUCTURE AND TERBIUM OXIDE DISTRIBUTION IN Ti-11 Al-0.5 Tb (at%)

100μm THICK SPLAT; AGED AT 800°C/0.25 hr

PRECIPITATE FREE ZONES IN Ti-11 Al-0.5 Tb (at%)

100μm THICK SPLAT, AGED AT 800°C/0.25 hr
AREA IN RIGHT SIDE, FIG. 37

FIG. 39

TERBIUM OXIDE DISTRIBUTION IN Ti-11 Al-0.5 Tb (at%)

100μm THICK SPLAT; AGED AT 800°C/4 hr
ANNULAR DARK FIELD STEM IMAGES

AREA IN UPPER RIGHT OF (a)

AREA IN FAR LEFT OF (b); TOP CENTER OF (a)

TERBIA DISTRIBUTION AND PFZ AT PRIOR-BETA GRAIN BOUNDARY

100μm THICK SPLAT; Ti-11 Al-0.5 Tb, AGED 800°C/0.25 hr

2 BEAM BRIGHT FIELD CTEM g = 0002

DARK FIELD, g = $\bar{4}40$, TYPE I TERBIA

R87-917553-2

FIG. 40

TERBIA DISTRIBUTION IN Ti-11 Al-0.5 Tb (at%)

100μm THICK SPLAT: AGED AT 800°C/0.25 hr

BRIGHT FIELD CTEM

DARK FIELD, g = 222, TYPE I TERBIA (SEE FIG. 42b)

FIG. 41

SELECTED AREA DIFFRACTION PATTERNS, Ti-11 Al-0.5 Tb, 800°C/0.25 hr

CENTER OF AREA SHOWN IN FIG. 41

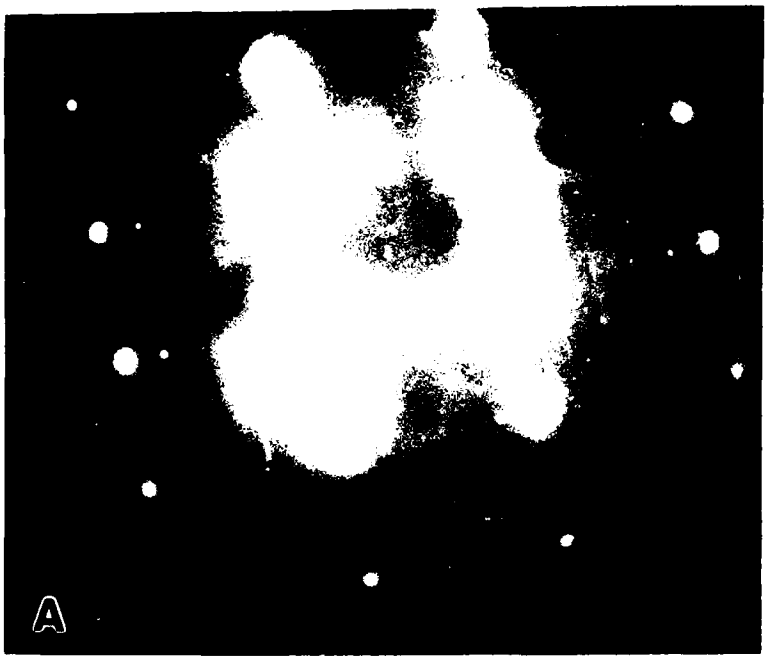

(a) [$1\bar{1}00$] MATRIX ZONE AXIS PATTERN, WITH [$11\bar{2}$] TERBIA PATTERN SUPERIMPOSED. (AREA OF FIG. 41)

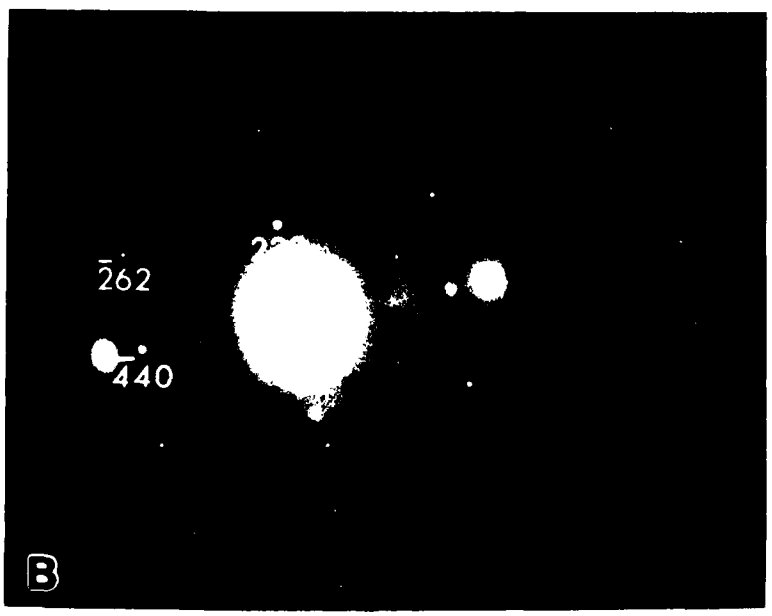

(b) SPECIMEN TILTED ~8° ABOUT [$11\bar{2}0$] WITH RESPECT TO (a) TO REDUCE DOUBLE DIFFRACTION. INDEXED SPOTS ARE TYPE I TERBIA

GRAIN STRUCTURE AND TERBIA DISTRIBUTION, Ti-11 Al-0.5 Tb (at%)

100μm THICK SPLAT; AGED AT 800°C/0.25 hr

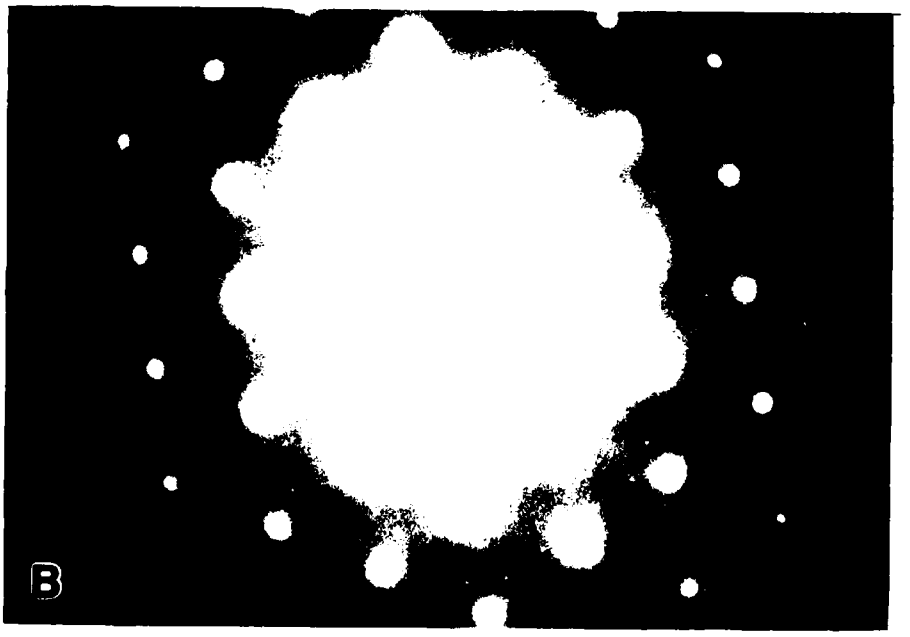

[0001] MATRIX ZONE AXIS PATTERN FROM LARGE GRAIN IN LOWER RIGHT OF (a). ALL SMALL SPOTS ARE FROM {440}. TYPE I TERBIA. REPLICATED BY DOUBLE DIFFRACTION.

FIG. 44

GRAIN STRUCTURE IN Ti-11 Al-0.5 Dy (at%)

80μm THICK SPLAT; AGED AT 800°C/0.25 hr

FIG. 45

DYSPROSIA DISTRIBUTION IN Ti-11 Al-0.5 Dy (at%)

80μm THICK SPLAT: AGED AT 800°C/0.25 hr

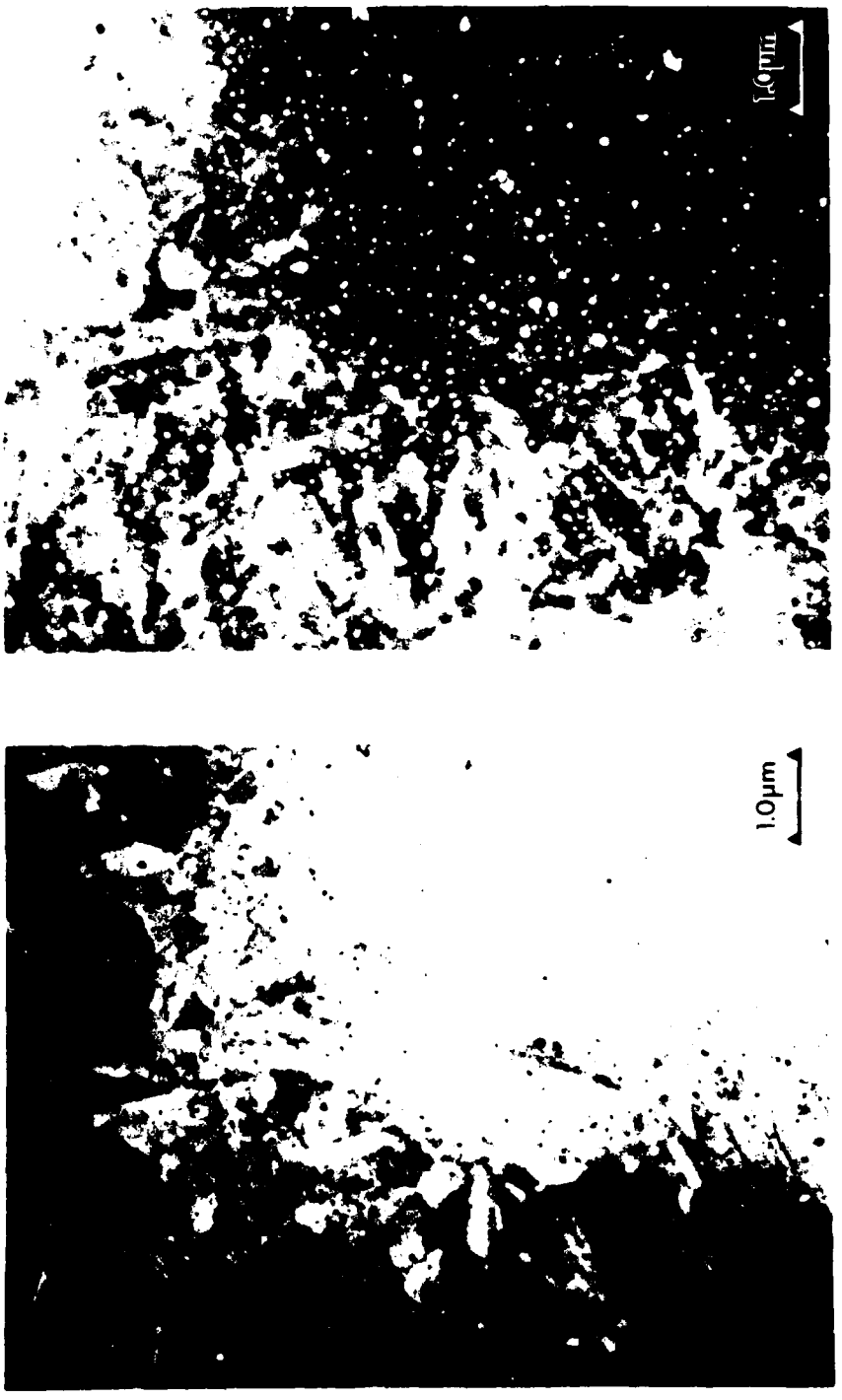

BRIGHT FIELD STEM

ANNULAR DARK FIELD STEM

FIG. 46

STRAIN CONTRAST FROM TYPE I DYSPROSIA IN Ti-11 Al-0.5 Dy (at%)

80μm THICK SPLAT, AGED AT 800°C/0.25 hr
TWO BEAM BRIGHT FIELD, g = 0002, Ti-Al HCP MATRIX

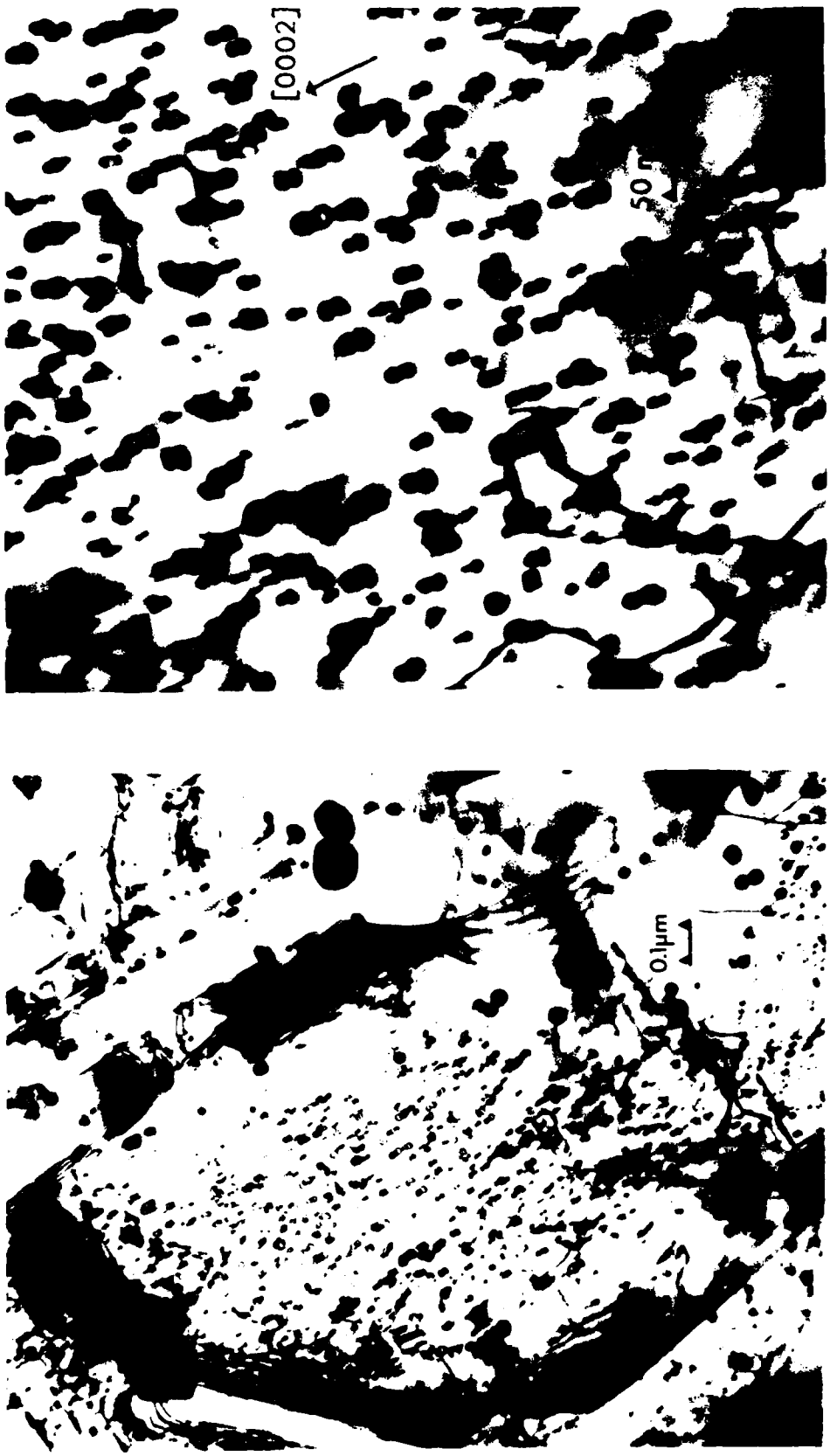

TYPE I DYSPROSIA DISTRIBUTION IN Ti-11 Al-0.5 Dy (at%)

80μm THICK SPLAT; AGED AT 800°C/0.25 hr
AREA SHOWN IN FIGURE 45

DARK FIELD CTEM, $g = \bar{4}40$,
TYPE I DYSPROSIA. MATRIX
ORIENTATION NEAR $[1\bar{1}00]$
ZONE AXIS

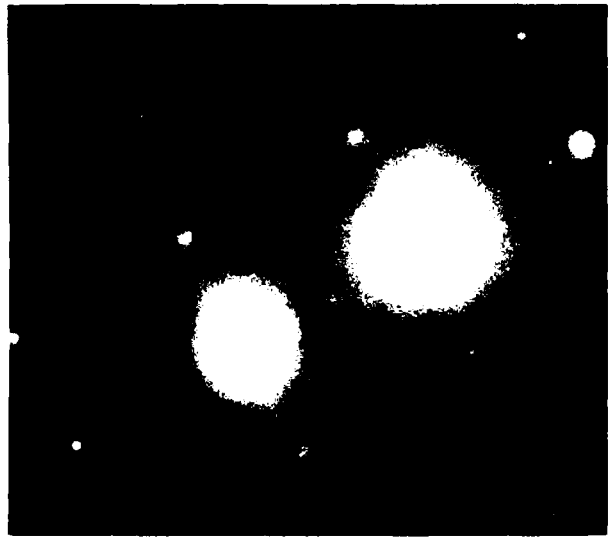

FIG. 47

FIG. 48

GRAIN STRUCTURE AND YTTRIA DISTRIBUTION Ti-11Al-0.5Y (at%)

130μm THICK SPLAT; AGED AT 800°C/0.25 hr

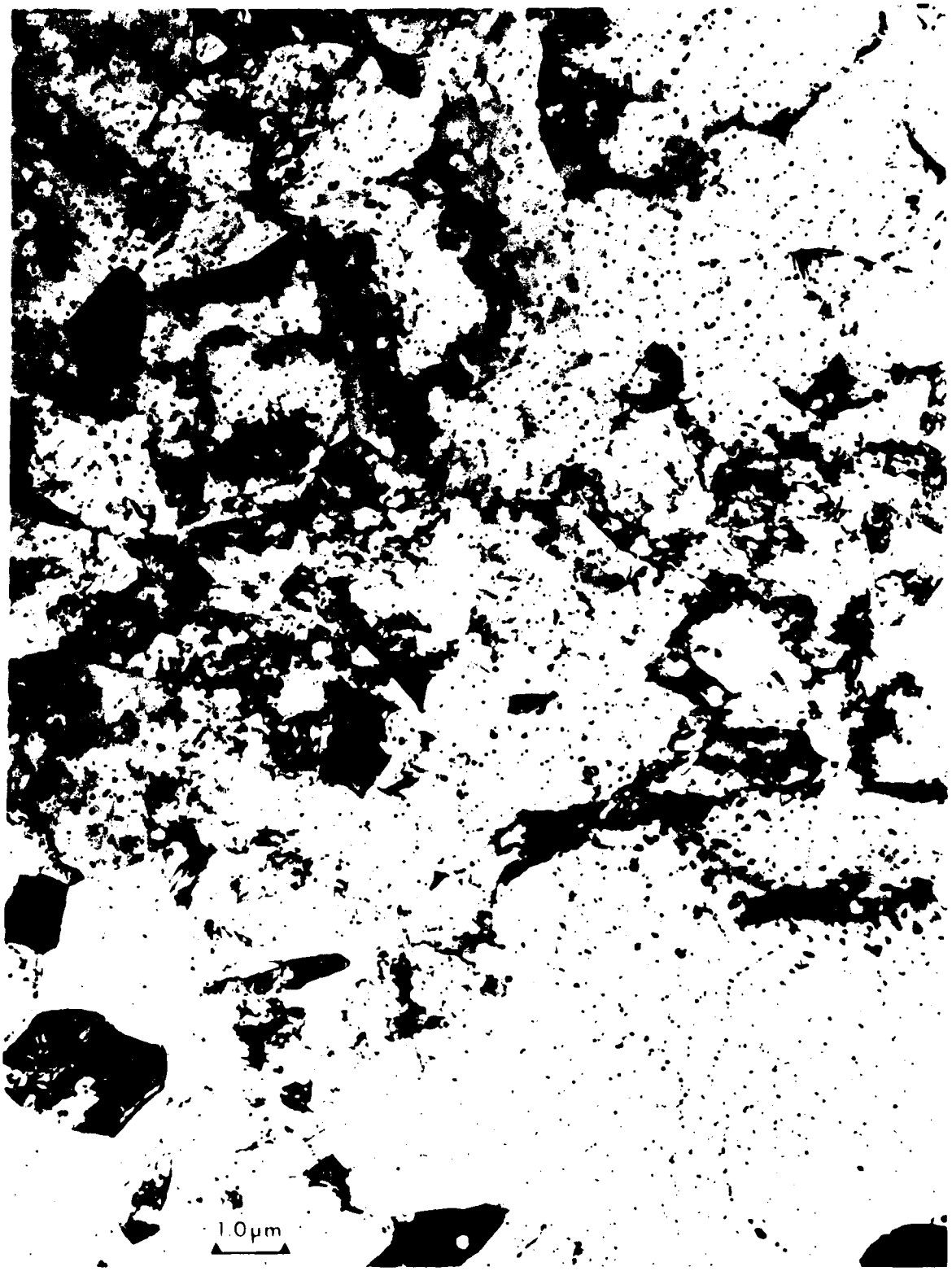

GRAIN STRUCTURE AND YTTRIA DISTRIBUTION Ti-11Al-0.5Y (at%)

130μm THICK SPLAT, AGED AT 800°C/0.25 hr

BIMODAY YTTRIA DISTRIBUTION IN Ti-11Al-0.5Y (at%)

130μm THICK SPLAT; AGED AT 800°C/0.25 hr

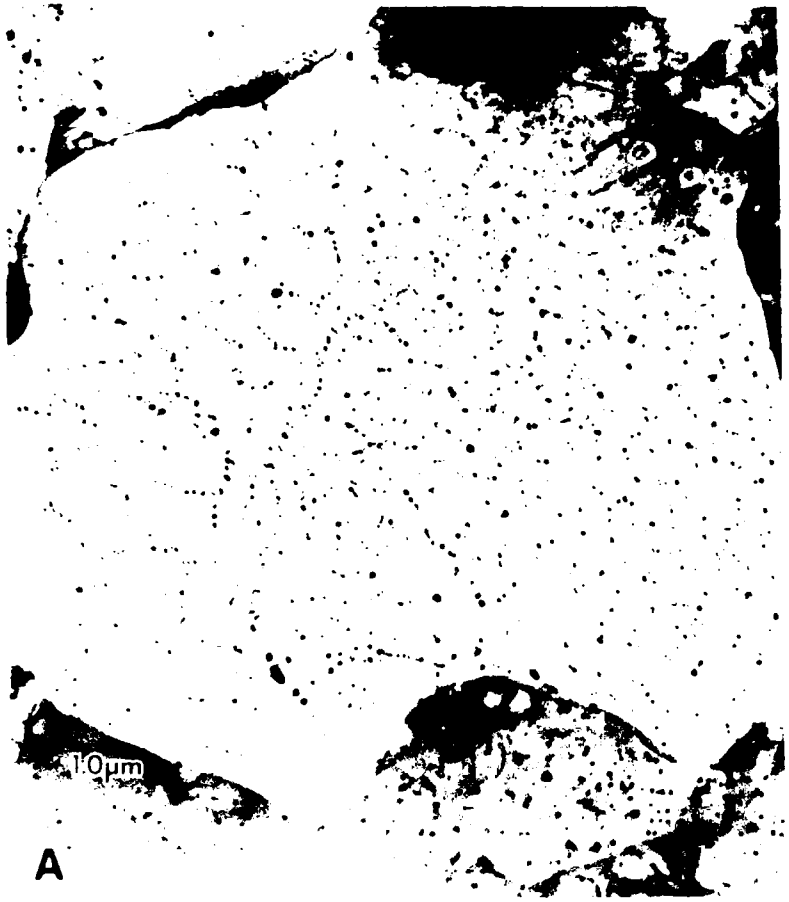

GRAIN IN LOWER RIGHT OF FIG. 48

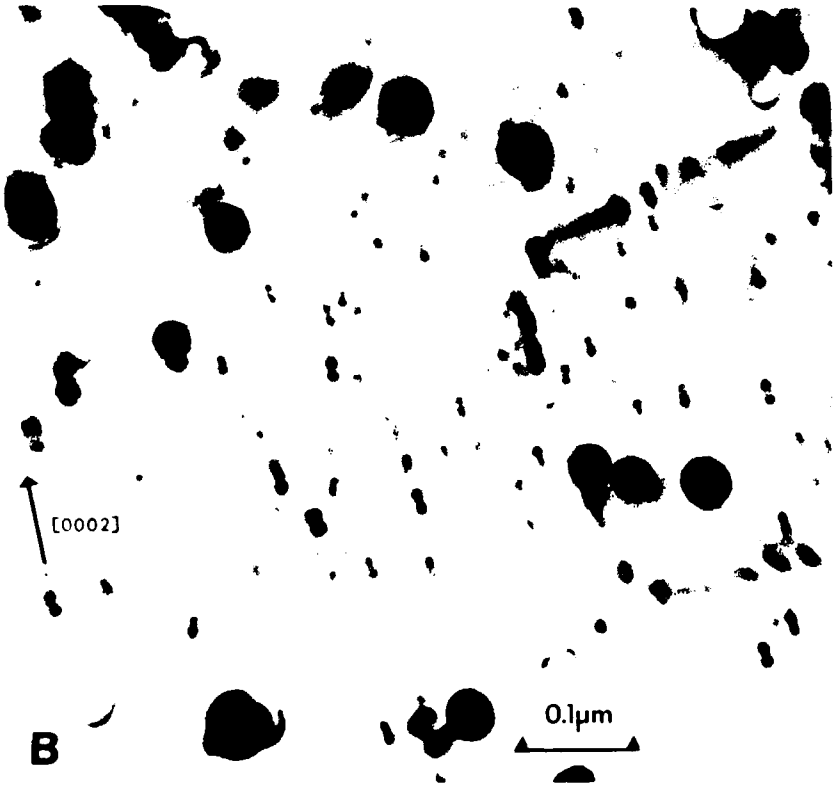

AREA IN CENTER OF (A). 2-BEAM BRIGHT FIELD, g = 0002

FIG. 50

FIG. 51

YTTRIA DISTRIBUTION IN Ti-11Al-0.5Y (at%)

130μm THICK SPLAT; AGED AT 800°C/0.25 hr
2-BEAM BRIGHT FIELD CTEM, g = 0002

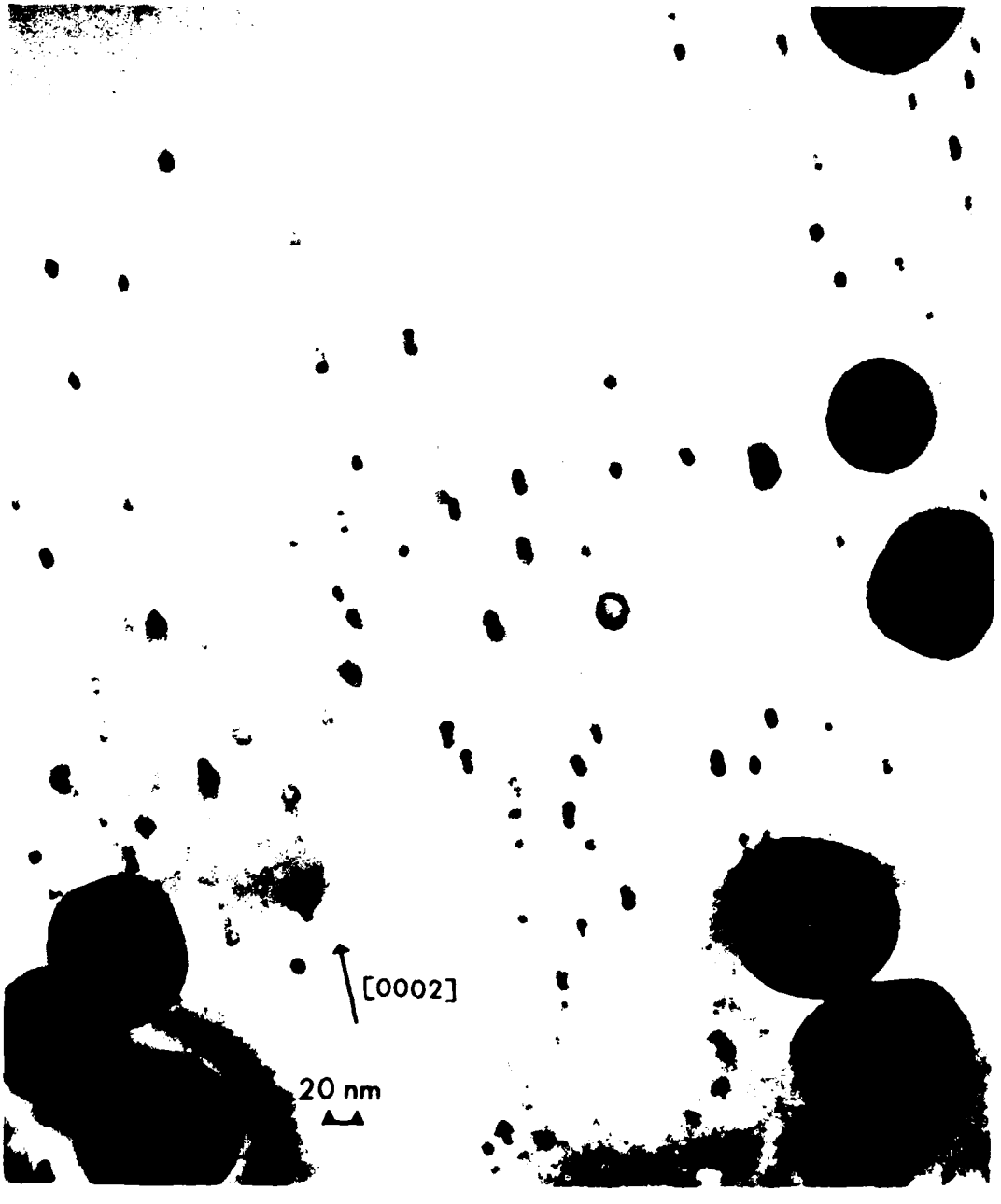

R87-917553-2

YTTRIA DISTRIBUTION IN Ti-11Al-0.5Y (at%)

130μm THICK SPLAT; AGED AT 800°C/0.25 hr
AREA IN LEFT OF FIG. 53

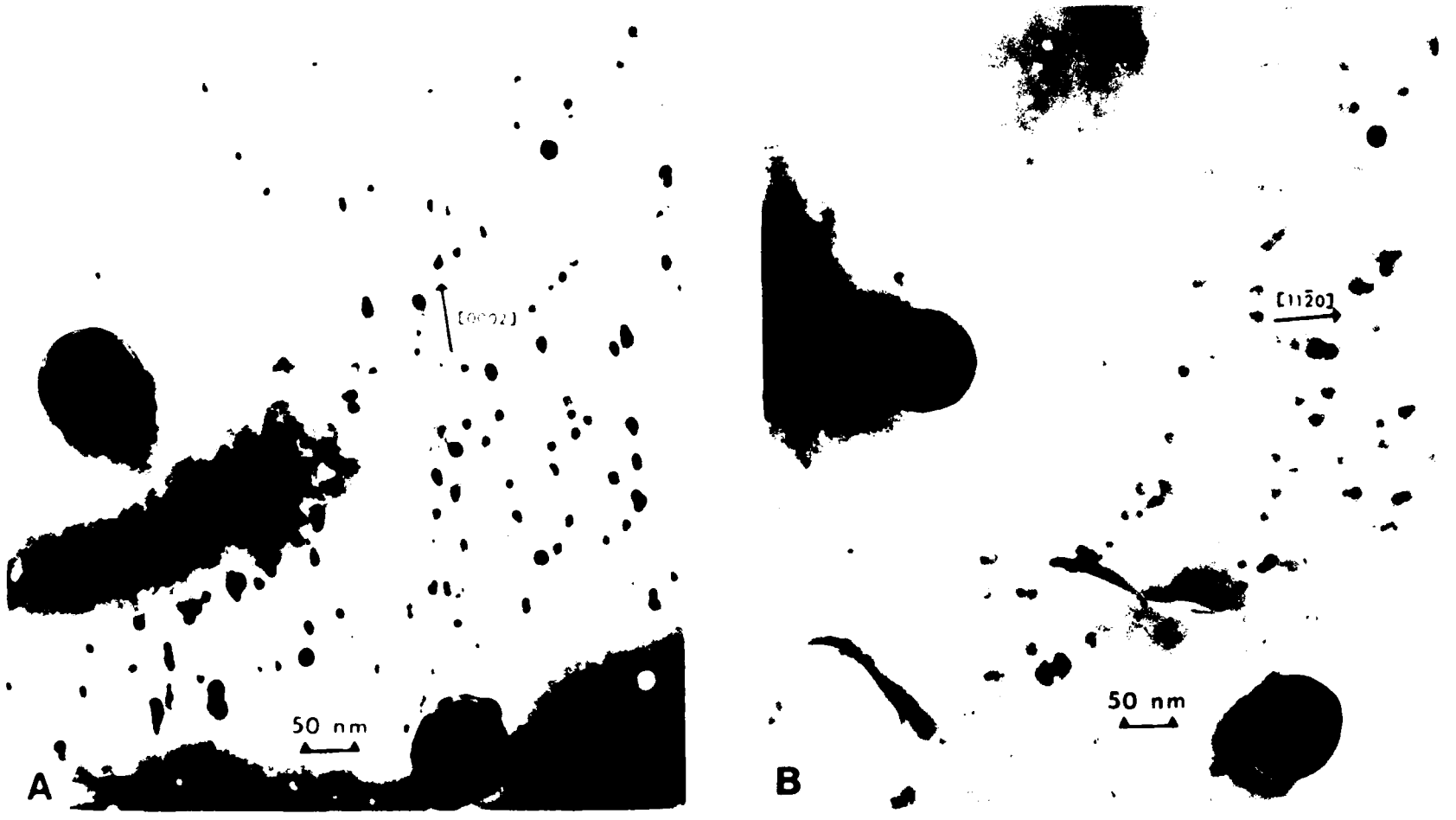

2-BEAM BRIGHT FIELD, g = 0002

2-BEAM BRIGHT FIELD, g = 11$\bar{2}$0

FIG. 52

YTTRIA DISTRIBUTION IN Ti-11Al-0.5Y (at%)

130μm THICK SPLAT; AGED AT 800°C/0.25 hr

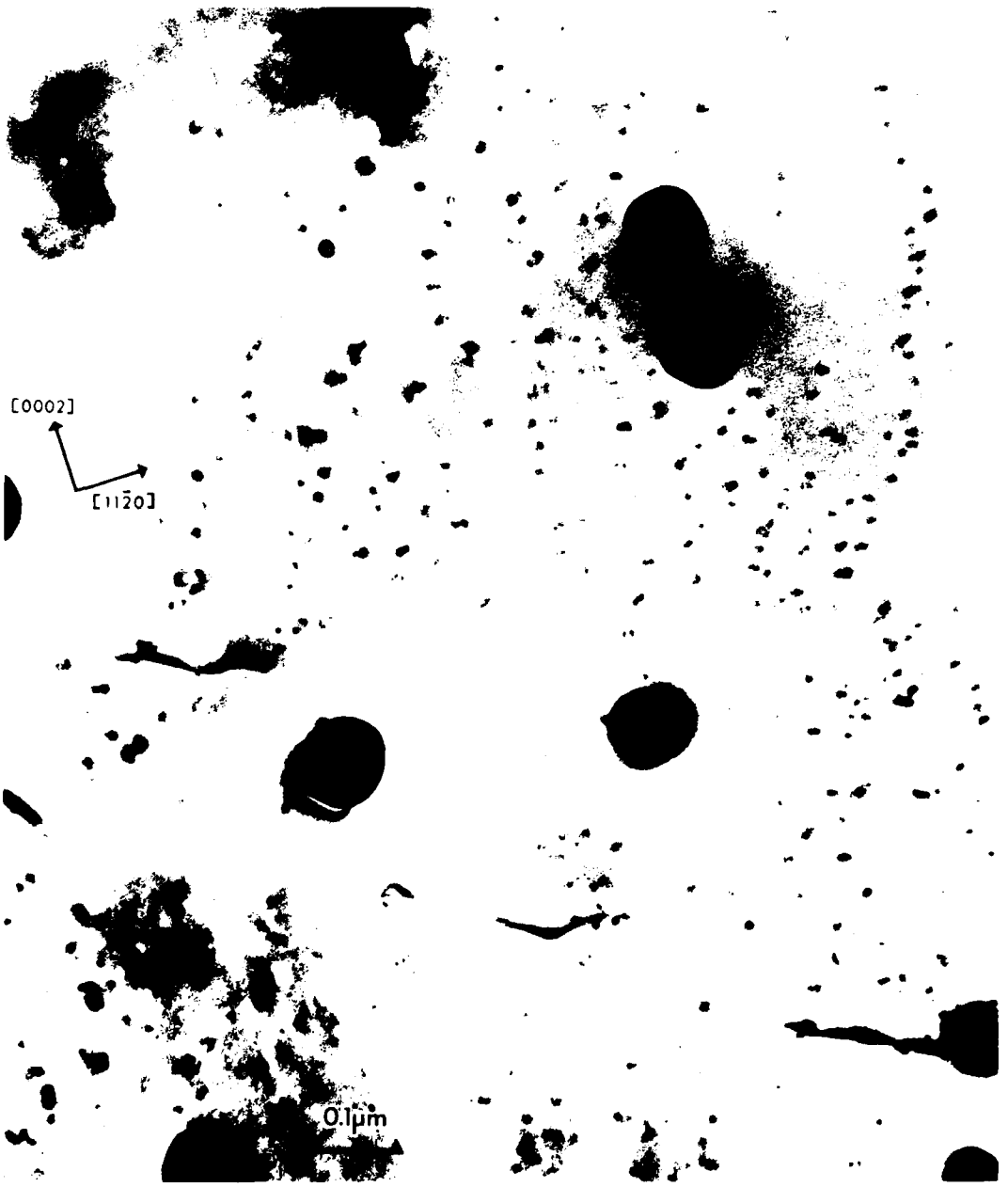

87 4 18 45

TYPE I YTTRIA DISTRIBUTION IN Ti-11Al-0.5Y (at%)

130μm THICK SPLAT; AGED AT 800°C/0.25 hr
AREA OF FIGS. 52, 53
DARK FIELD, g = $\bar{4}40$, TYPE I YTTRIA

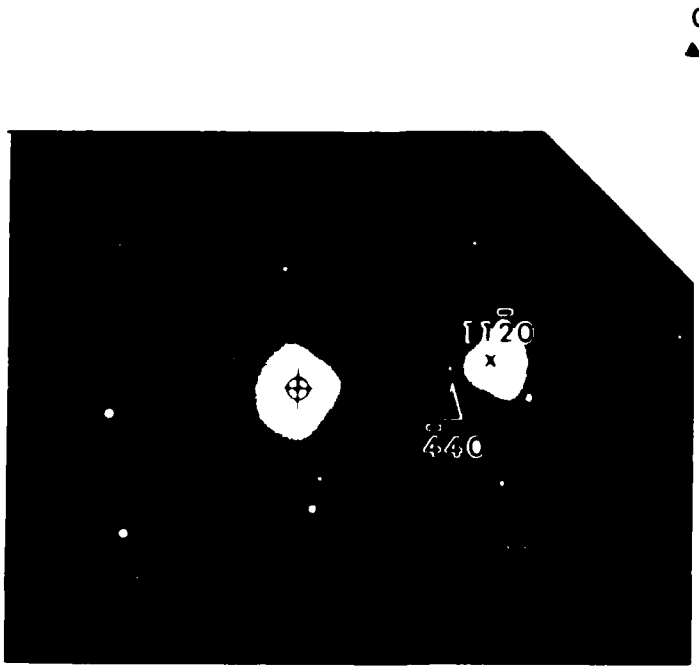

FIG. 55

TYPE II YTTRIA DISTRIBUTION IN Ti-11Al-0.5Y (at%)

130μm THICK SPLAT; AGED 800°C/0.25 hr
AREA OF FIGS. 52, 53, 54
DARK FIELD, g = 222, TYPE II YTTRIA

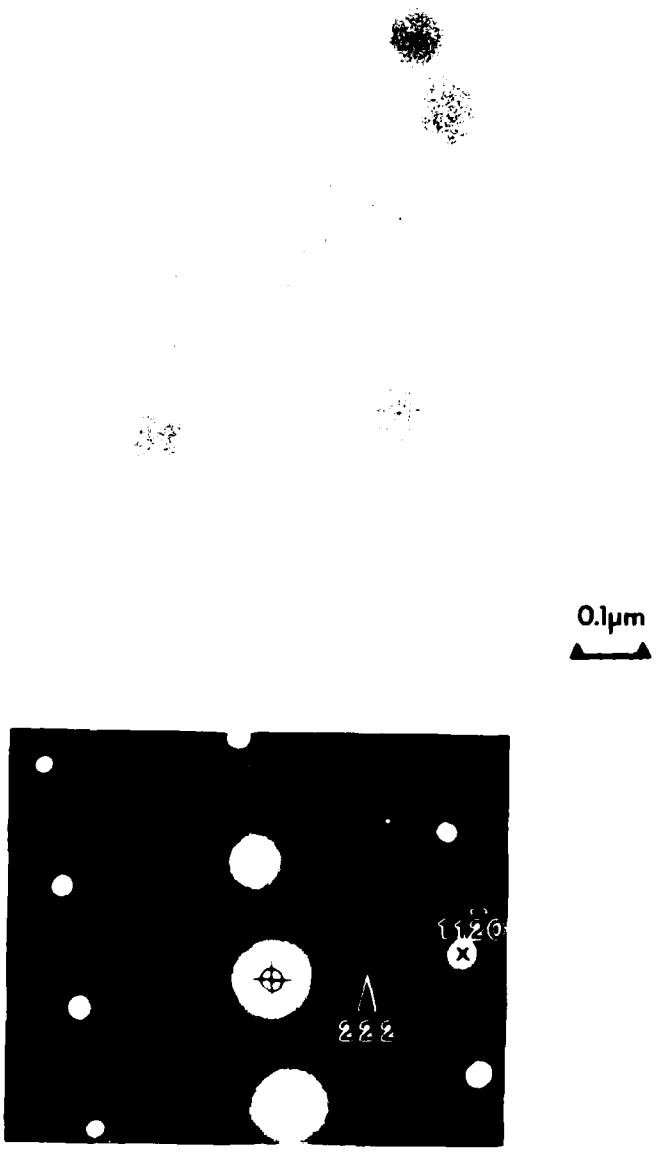

87 4 18 47

FIG. 56

GRAIN STRUCTURE AND GADOLINIA DISTRIBUTION Ti-11Al-0.5Gd (at%)

125μm THICK SPLAT; AGED AT 800°C/0.25 hr

87 4 18 48

Gd_2O_3 DISTRIBUTION IN Ti-11Al-0.5Gd (at%)

125μm THICK SPLAT: AGED AT 800°C/0.25 hr

87 4 18 49

Gd_2O_3 DISTRIBUTION IN Ti-11Al-0.5Gd (at%)

125μm THICK SPLAT; AGED AT 800°C/0.25 hr

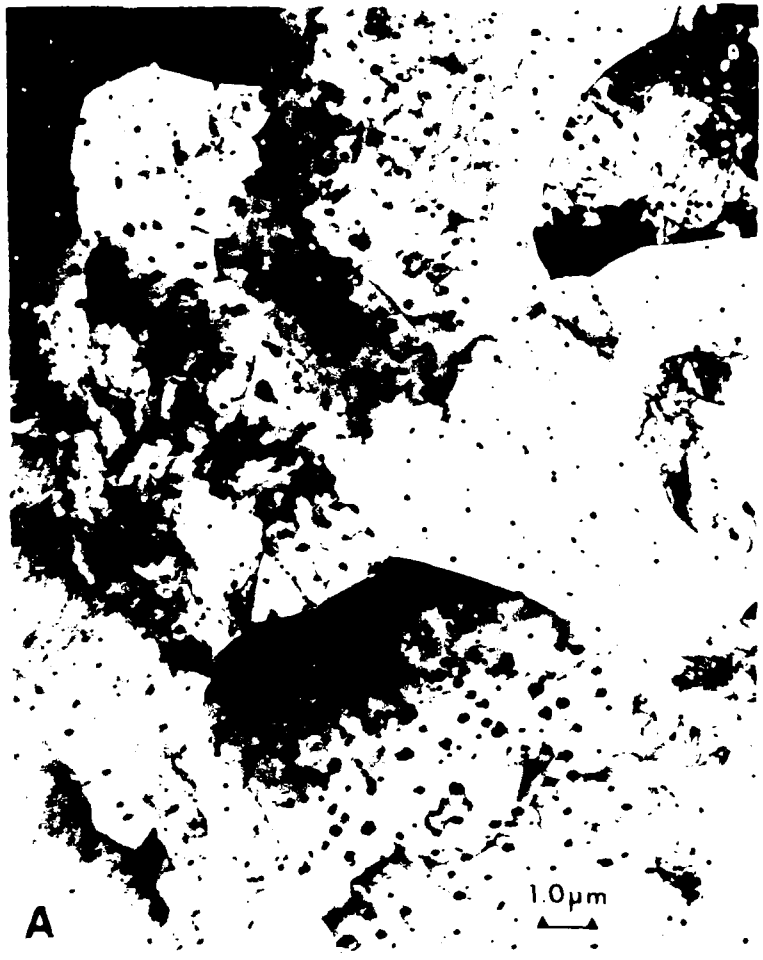

BRIGHT FIELD CTEM

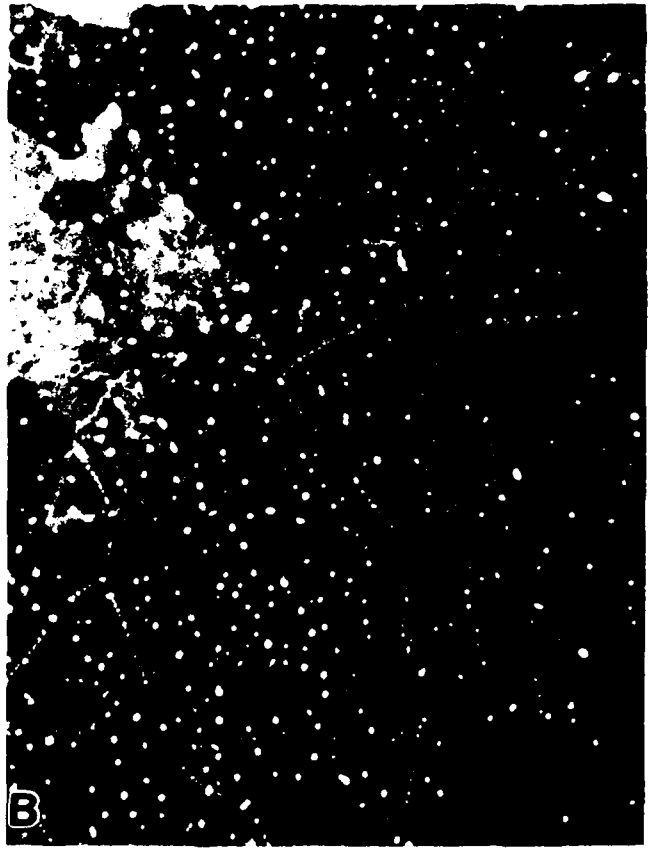

ANNULAR DARK FIELD STEM

FIG. 58

R87-917553-2

FIG. 59

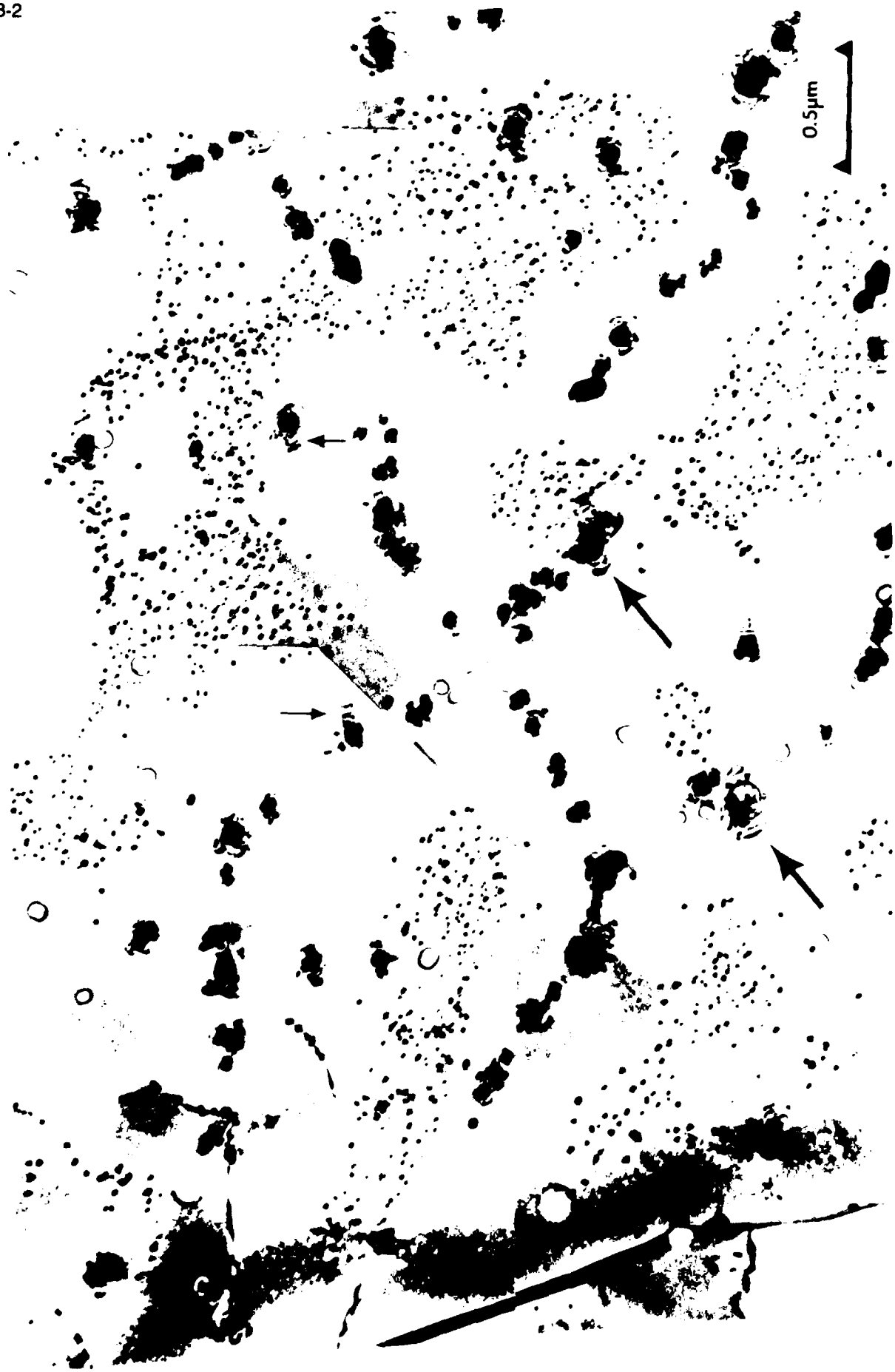

Gd_2O_3 DISTRIBUTION IN Ti-11Al-0.5Gd (at%)

125μm THICK SPLAT, AGED AT 800°C/0.25 hr. AREA OF FIG. 57
ARROWS MARKS DISLOCATION LOOP AT LARGE PRECIPITATE

FIG. 60

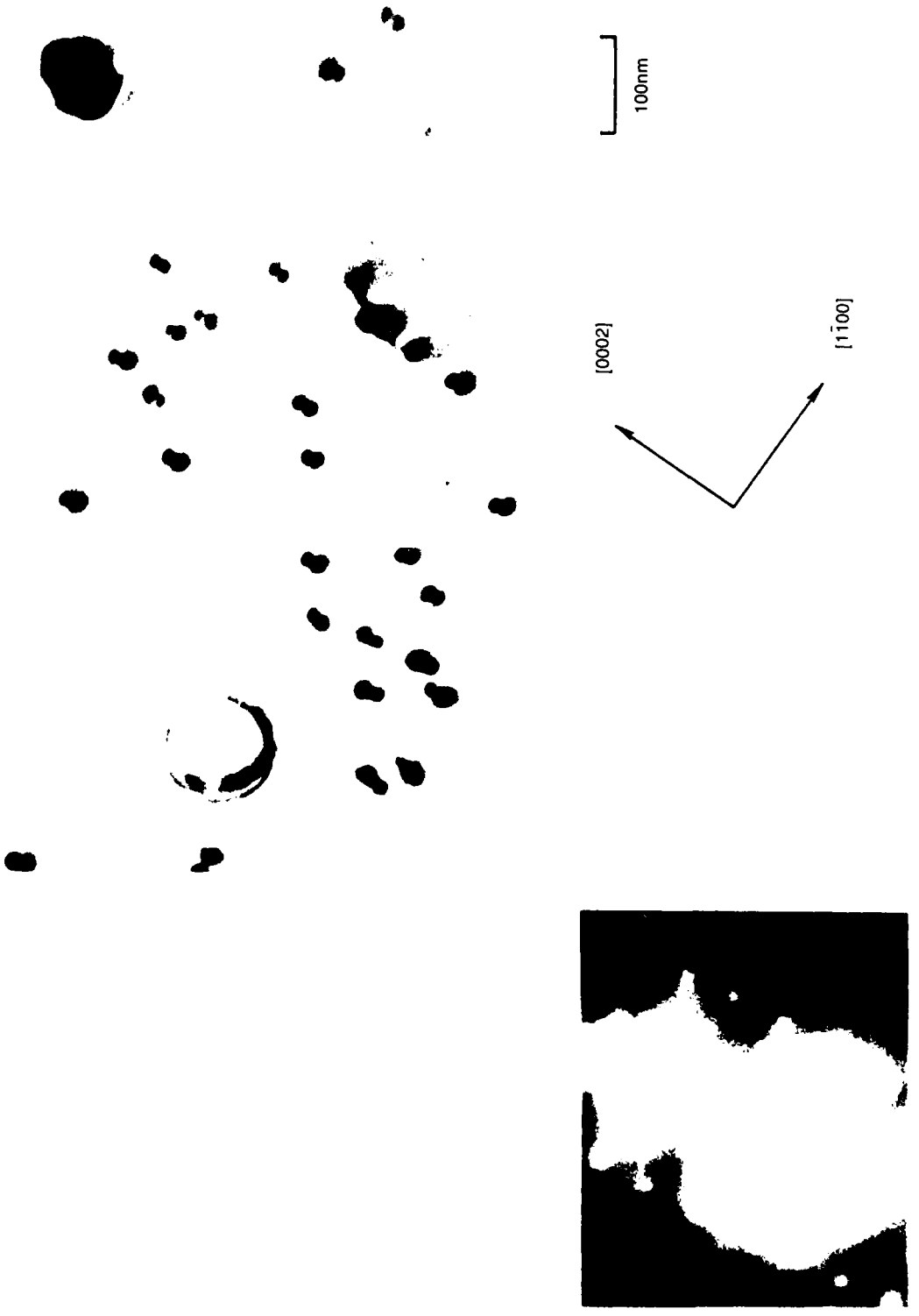

Gd_2O_3 PRECIPITATES IN Ti-11Al-0.5Gd (at%)

125μm THICK SPLAT, AGED AT 800°C/0.25 hr
TWO-BEAM BRIGHT FIELD, g = 0002, Ti-Al MATRIX

Gd_2O_3 DISTRIBUTION IN Ti-11Al-0.5Gd (at%)

AREA IN FIG. 59; 125μm THICK SPLAT; AGED AT 800°C/0.25 hr

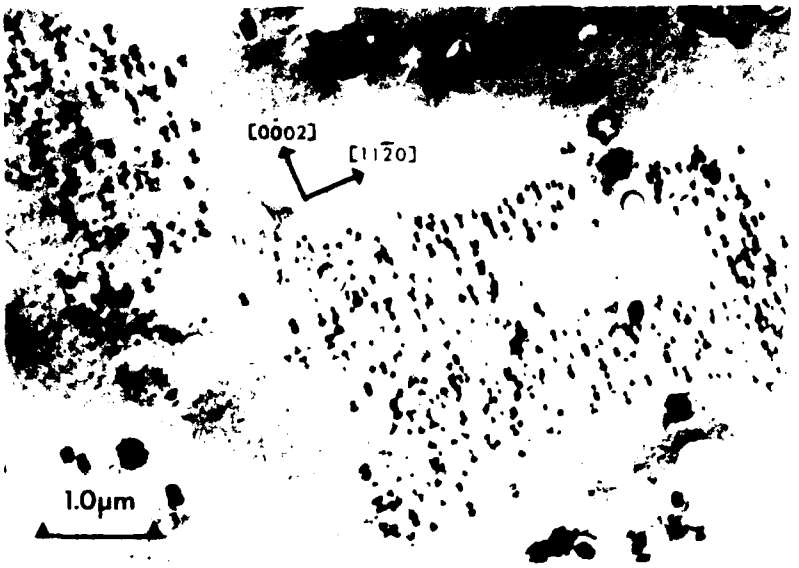

DARK FIELD; $\bar{g} = 0002$, Ti-Al MATRIX

DARK FIELD; $\bar{g} = 222$, TYPE I Gd_2O_3

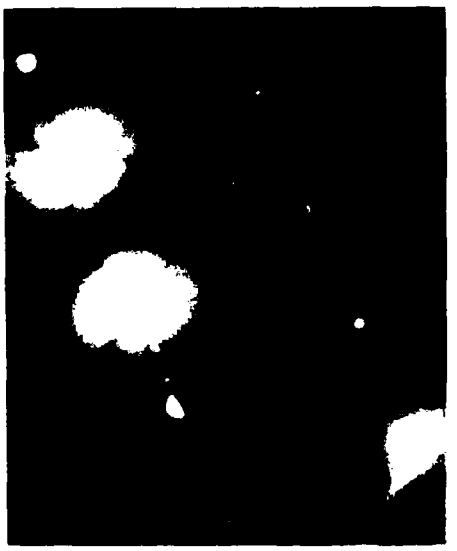

SADP, NEAR [1$\bar{1}$00] ZONE AXIS

Gd_2O_3 DISTRIBUTION IN Ti-11Al-0.5Gd (at%)

125μm THICK SPLAT; AGED AT 800°C/0.25 hr
2-BEAM CTEM, g = 0002

87 4 18 53

Gd_2O_3 DISTRIBUTION IN Ti-11Al-0.5Gd (at%)

125μm THICK SPLAT; AGED AT 800°C/0.25 hr; AREA OF FIG. 62
DARK FIELD CTEM, $g = \bar{4}\bar{4}0$, TYPE I Gd_2O_3 (FIG. 64)

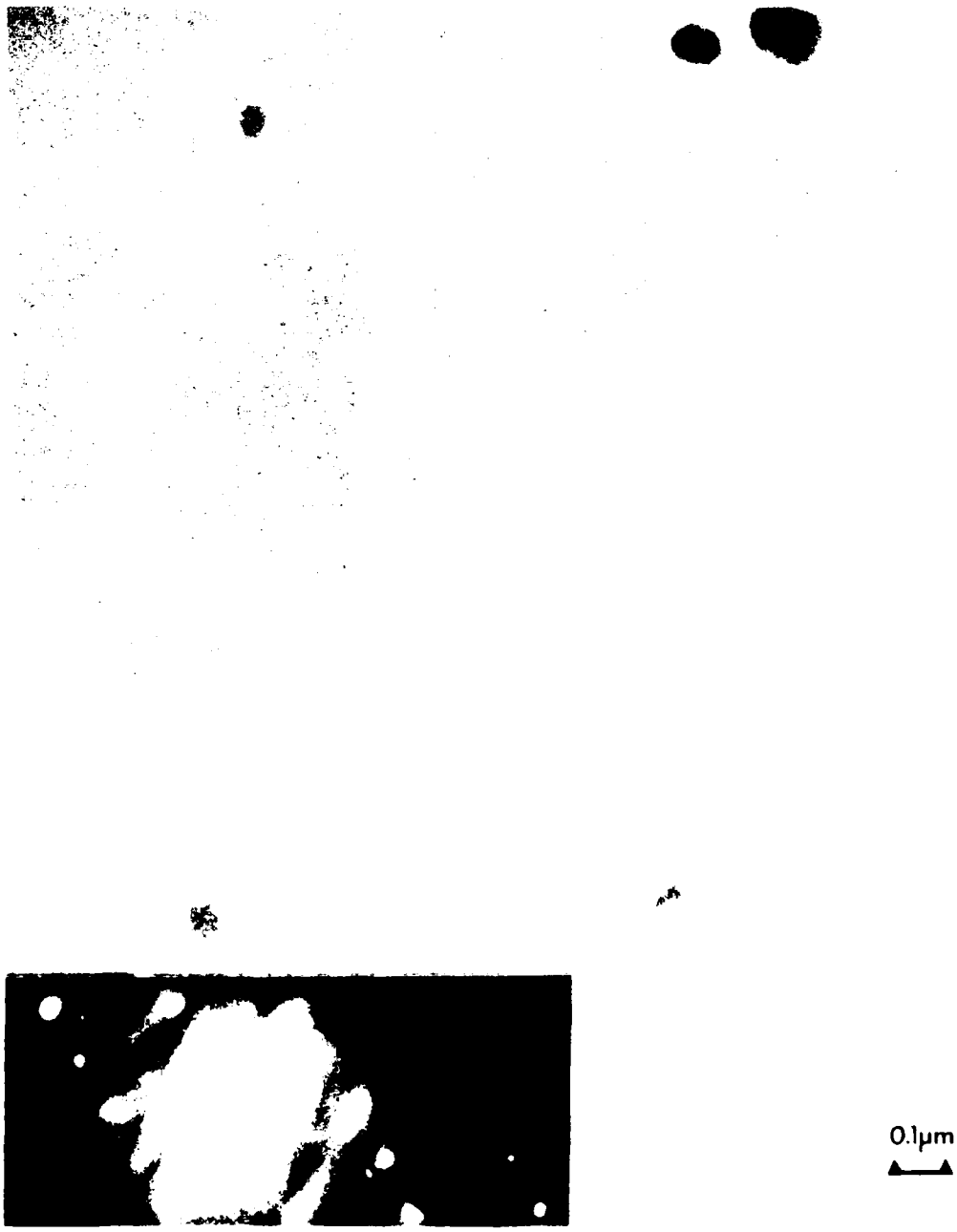

FIG. 64

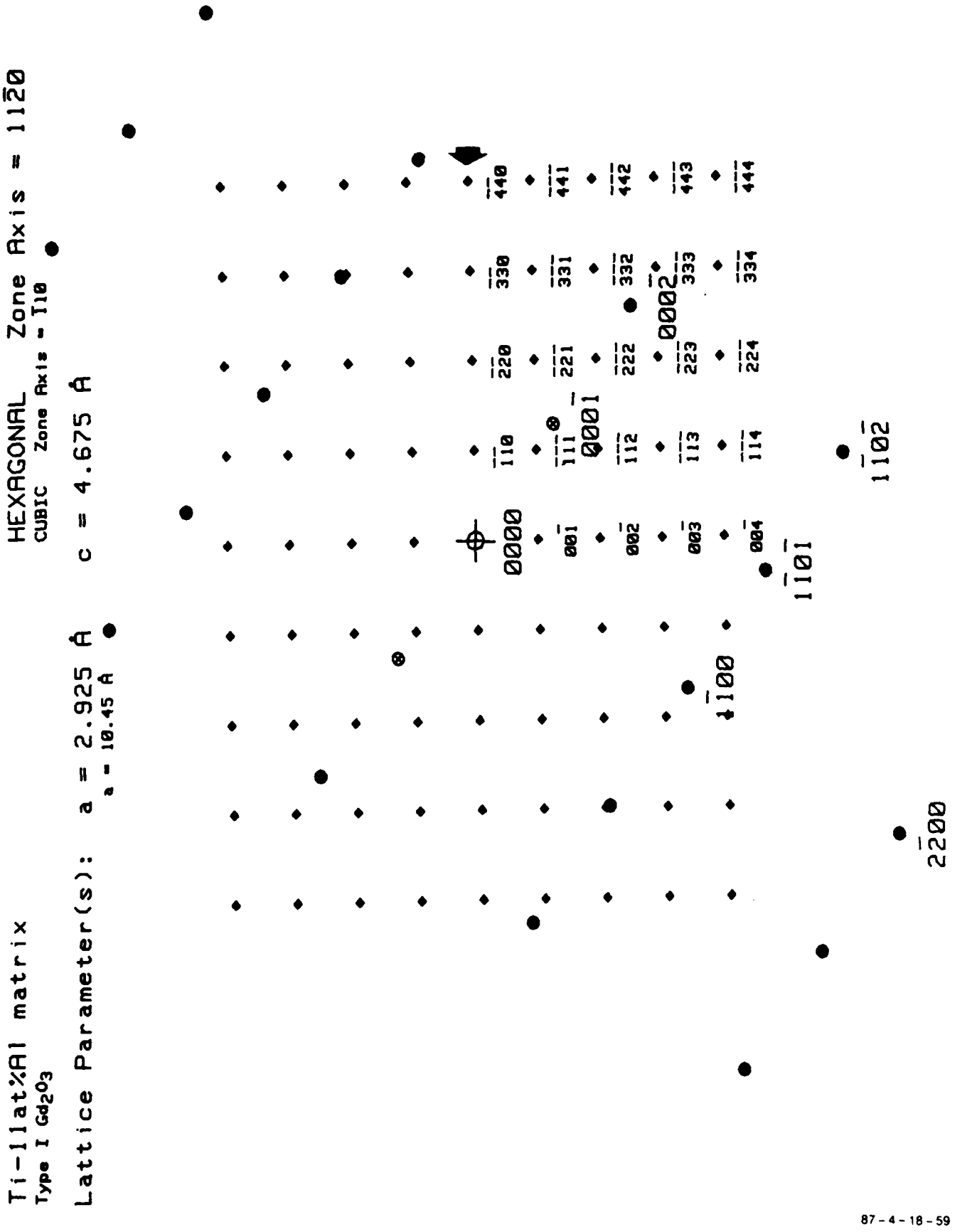
Ti-11at%Al matrix
Type I Gd_2O_3
Lattice Parameter(s): a = 2.925 Å
a = 10.45 Å
c = 4.675 Å
HEXAGONAL Zone Axis = 11$\bar{2}$0
CUBIC Zone Axis = 110
0000
0001
0002
1100
1101
1102
2200
87-4-18-59

FIG. 65

LUTETIA DISTRIBUTION IN Ti-11Al-0.5Lu (at%)

125μm THICK SPLAT; AGED AT 800°C/4 hr

LUTETIA DISTRIBUTION IN Ti-11Al-0.5Lu (at%)

125μm THICK SPLAT. AGED AT 800°C/4 hr

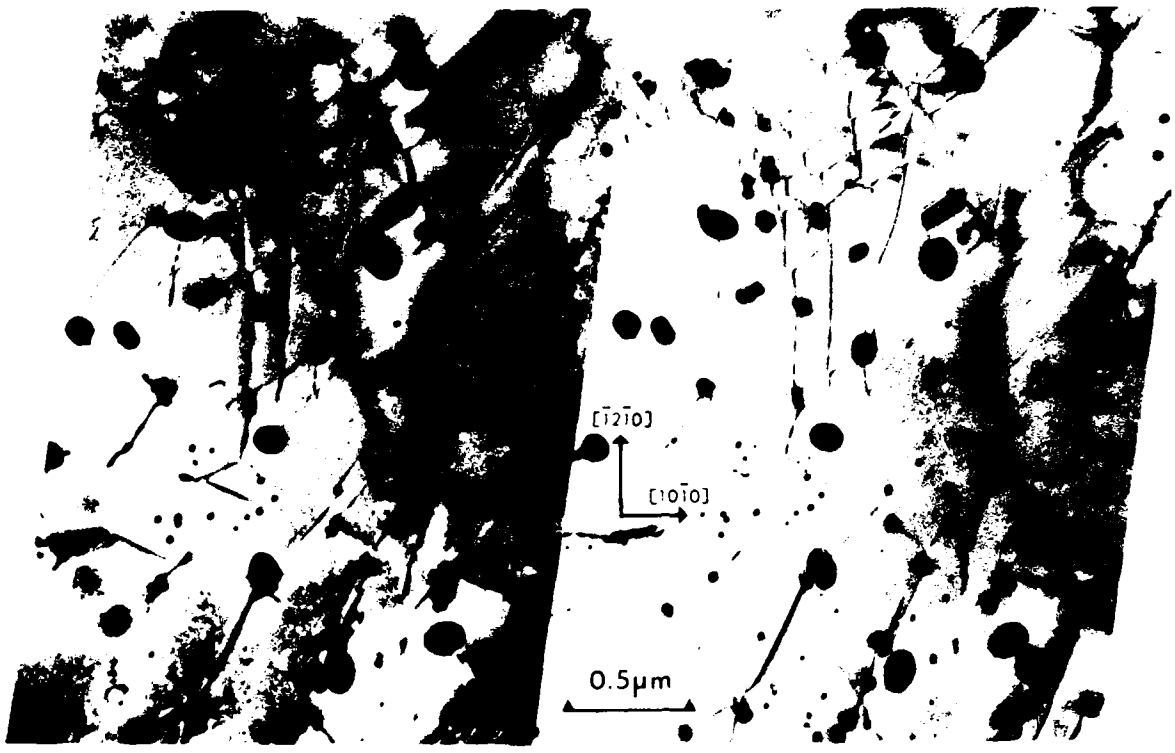

(a) BRIGHT FIELD CTEM STEREO PAIR, $g = \bar{1}2\bar{1}0$
TOTAL TILT ~12°, ±6° ON EITHER SIDE OF [0001]

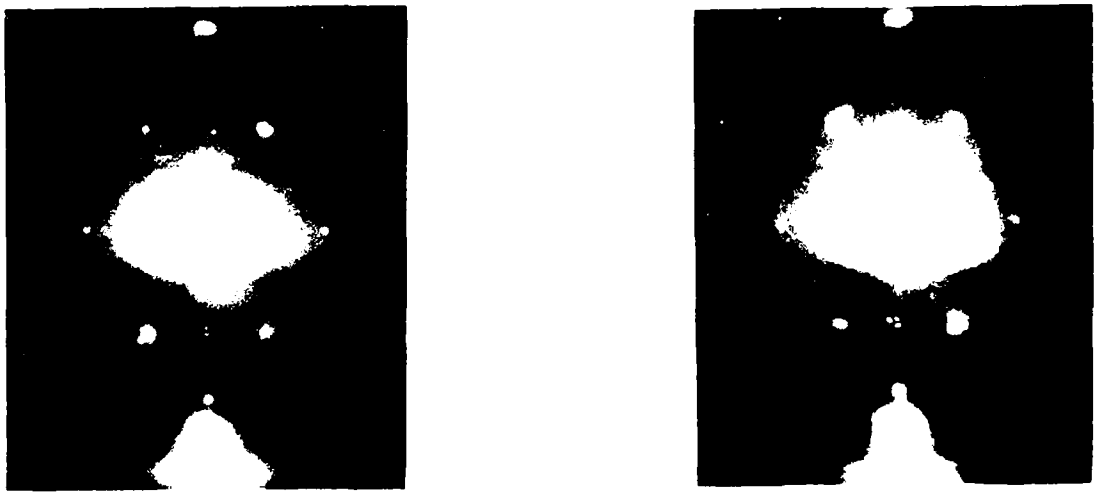

(b) SELECTED AREA DIFFRACTION PATTERNS FROM THE CENTER OF
THE LEFT AND RIGHT PHOTOMICROGRAPHS IN (a)

AD-A183 882 INVESTIGATION OF RAPIDLY-SOLIDIFIED DISPERSION STRENGTHENED TITANIUM ALLOYS(U) UNITED TECHNOLOGIES RESEARCH CENTER EAST HARTFORD CT D B SNOW 01 JUL 87 UTRC/R87-917553-2 2/2

UNCLASSIFIED F/G 11/6.1 NL

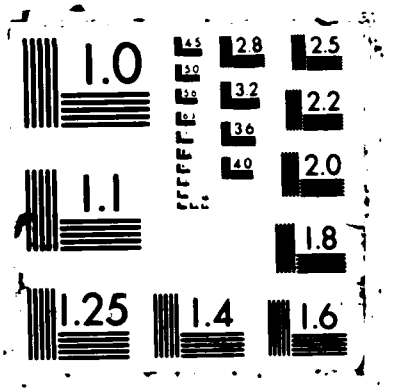
1.0
1.1
1.25
1.4
1.6
1.8
2.0
2.2
2.5
2.8
3.2
3.6
4.0
4.5
5.0
5.6

[0001] MATRIX SELECTED AREA DIFFRACTION PATTERN FROM AREA SHOWN IN FIG. 66

{440} SPOTS FROM A ⟨111⟩ ZONE AXIS PATTERN OF TYPE I Lu_2O_3 ARE SUPERIMPOSED

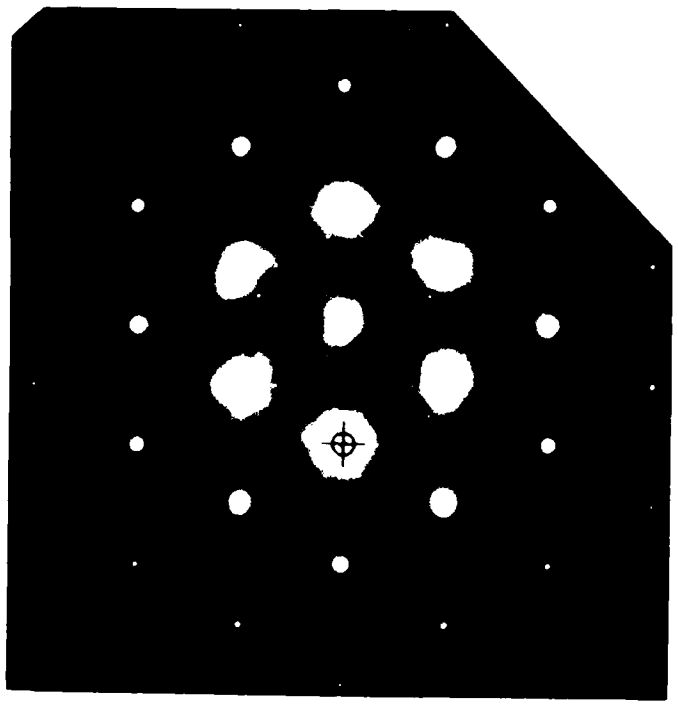

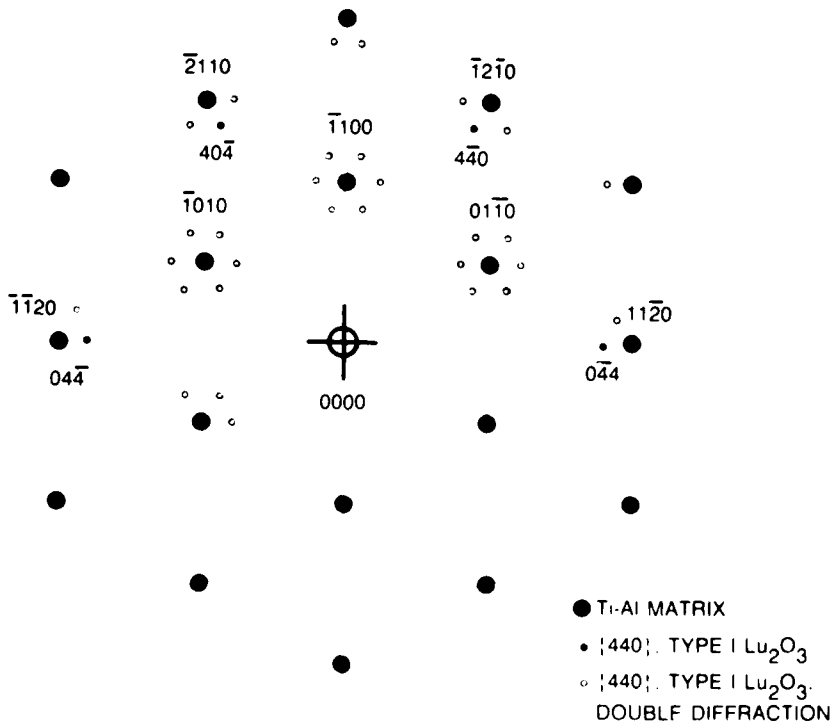

87 - 4 - 18 - 56

TYPE I Lu_2O_3 DISTRIBUTION IN Ti-11Al-0.5Lu (at%)

125μm THICK SPLAT; AGED AT 800°C/4 hr

AREA SHOWN IN FIG. 66 DARK FIELD; $g = 44\bar{0}$, TYPE I Lu_2O_3

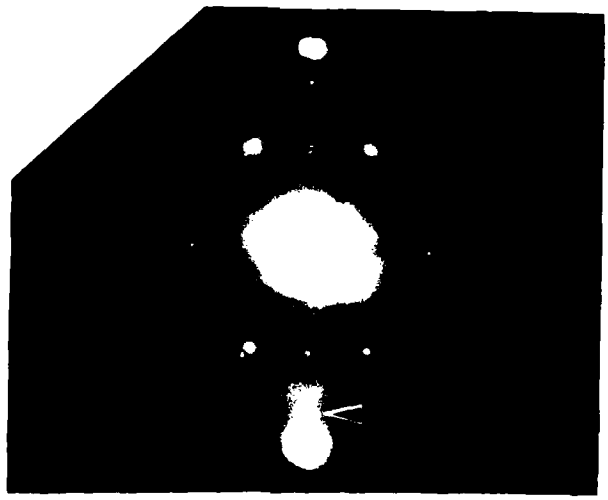

TYPE II Lu_2O_3 IN Ti-11Al-0.5Lu (at%)

125μm THICK SPLAT; AGED AT 800°C/4 hr
AREA SHOWN IN FIG. 66 DARK FIELD, g = 222, TYPE II Lu_2O_3

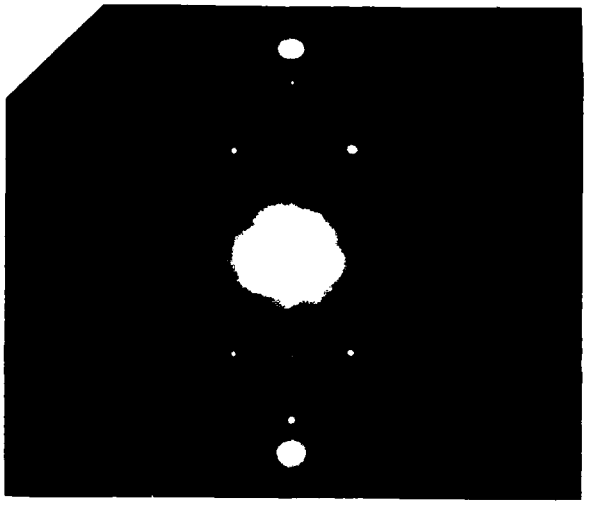

GRAIN STRUCTURE AND LANTHANUM OXIDE DISTRIBUTION, Ti-11Al-0.5La (at%)

94μm THICK SPLAT, AGED AT 800°C/0.25 hr

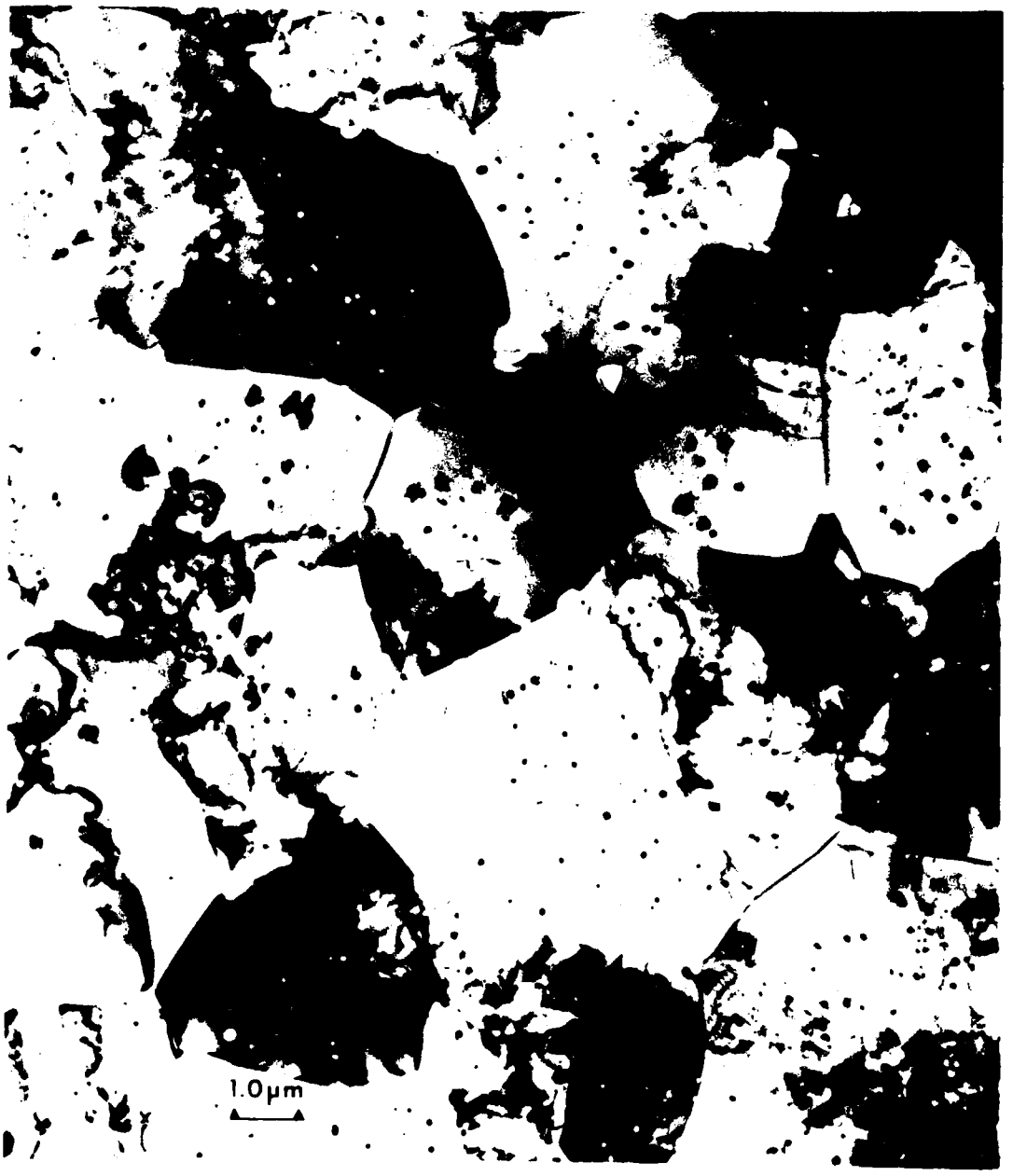

GRAIN STRUCTURE AND NEODYMIUM OXIDE DISTRIBUTION, Ti-11Al-0.5Nd (at%)

100μm THICK SPLAT, AGED AT 800°C/0.25 hr

87-4-18-63

ORIENTATION RELATIONSHIPS:
CUBIC RARE EARTH OXIDE PRECIPITATES IN HCP ALPHA TITANIUM-ALUMINUM

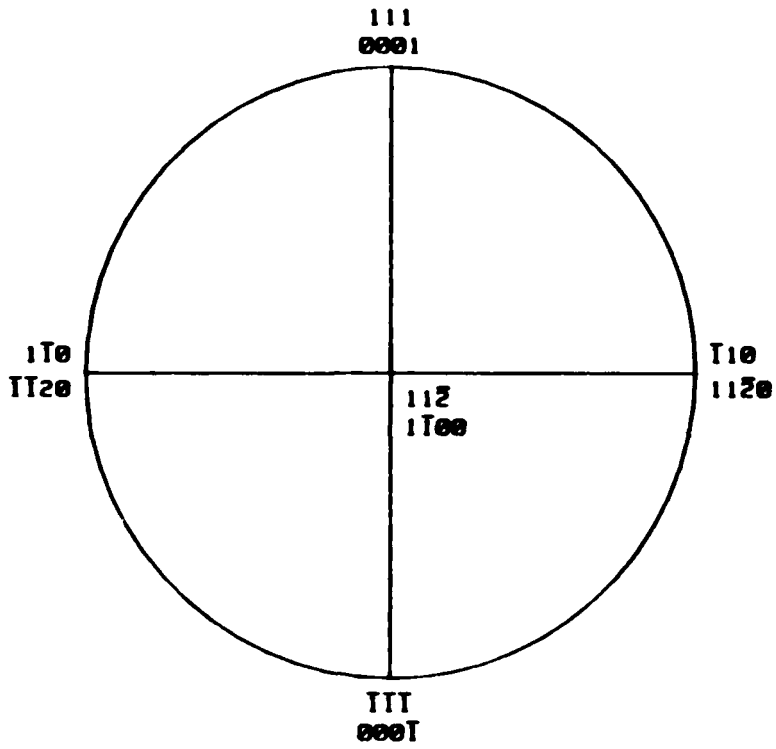

Type I Precipitates

Metastable Cubic

(11$\bar{2}$) REO || (1$\bar{1}$00) Ti

<111> REO || [0001] Ti

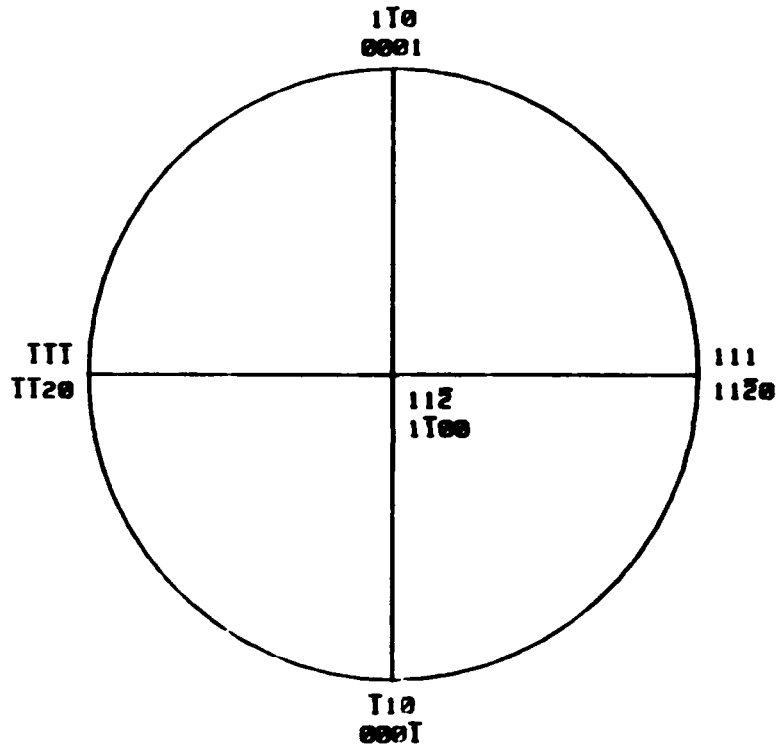

Type II Precipitates

Equilibrium Cubic Sesquioxides

(11$\bar{2}$) M_2O_3 || (1$\bar{1}$00) Ti

<1T0> M_2O_3 || [0001] Ti

87-4-18-64

FIG. 72

FIG. 73

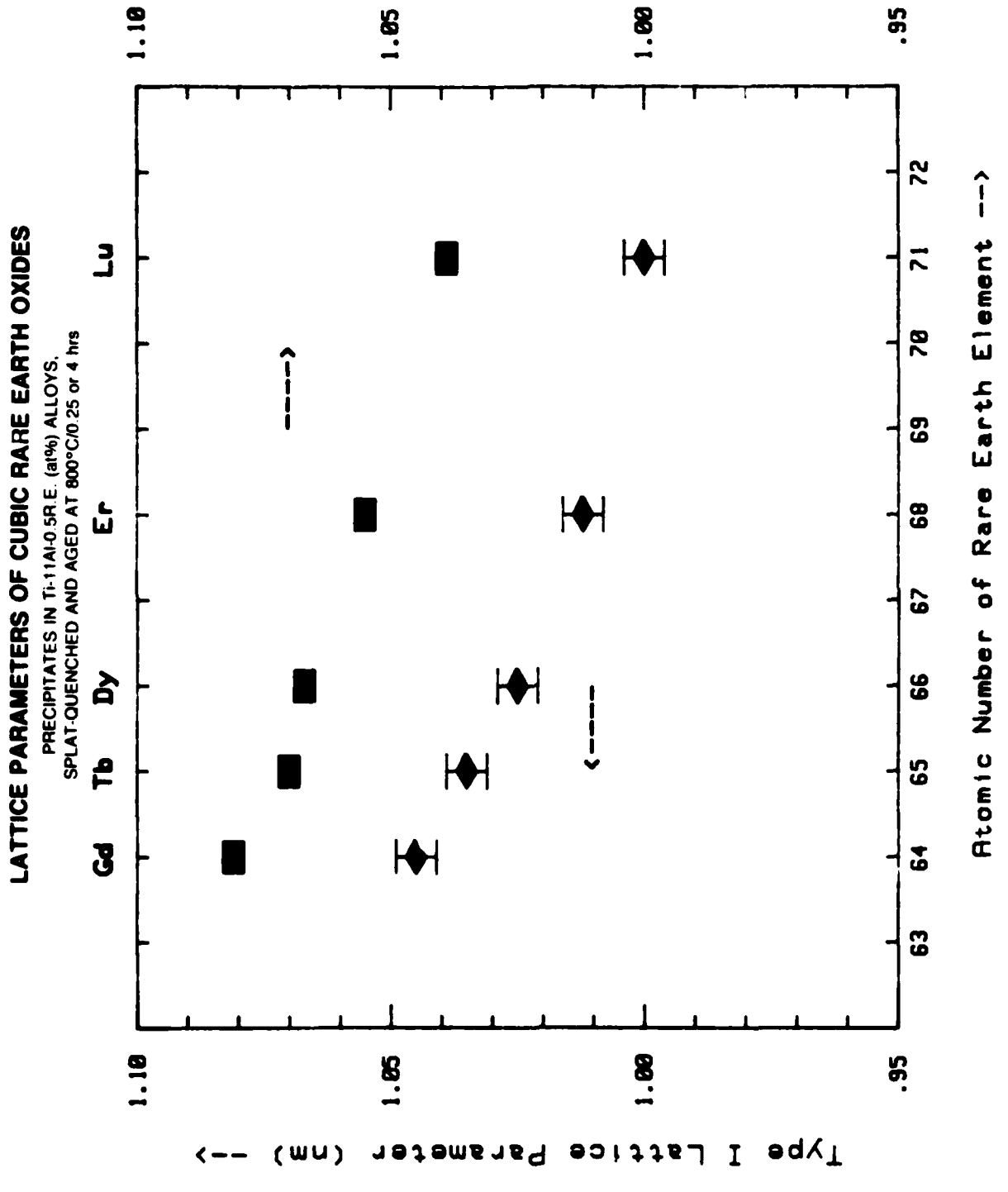

87-4-18-65

END

9-87

DTIC